Effects of Organic Matter Complexation on Partitioning of First-row Transition Metals Into Calcite: Cave-analogue Crystal Growth Studies

A thesis
submitted in partial fulfilment
of the requirements for the degree
of
Master of Science in Chemistry
at
The University of Waikato
by
Ingrid Lindeman

THE UNIVERSITY OF
WAIKATO
Te Whare Wānanga o Waikato

2020

Abstract

Speleothems are important archives of terrestrial paleoclimate due to their wide geographical coverage and the ability to date their growth layers using U-Th and U-Pb radiometric dating. Extensive research into various speleothem-based geochemical proxies has been undertaken in the last half century, and a significant number of proxies are now used routinely for reconstructions of paleoclimate including stable oxygen and carbon isotopes (known to respond to variations in rainfall and temperature), fluorescence (indicative of the quality and quantity of organic matter present in cave dripwaters) and speleothem minerology (e.g. fabric defects and nano-crystal aggregation). Trace element proxies in speleothems have also garnered attention, but the suite of trace elements used to date has primarily been limited to the alkali earth metals as they exhibit simple partitioning and are characterised by partition coefficients (K_d values) less than 1. Their role in karst systems is thus comparatively well constrained.

In contrast, the first-row transition metals have been the focus of only a few speleothem-based studies, despite recent evidence suggesting some of these metals (namely Co, Ni and Cu) may be useful additions to the current suite of trace element proxies already utilised. Thus, although theoretical distribution coefficient data are available for these metals, their partitioning behaviour into speleothem calcite is not well understood. Theoretical distribution coefficients are useful in understanding partitioning behaviour under certain conditions, but the non-thermodynamic nature of partition coefficients during calcite precipitation in most natural contexts requires partitioning behaviour under speleothem-specific conditions to be established. For instance, despite theoretical distribution coefficients being greater than 1 for Co, Ni and Cu, apparent partition coefficients ($K_{d\ app}$) calculated for these metals in actual speleothem samples are frequently less than 1 due to the dependence of $K_{d\ app}$ on a number of factors including calcite precipitation rate, crystal morphology, and complexation reactions between natural organic matter (NOM) and trace ions. Indeed, complexation of first-row transition metals in speleothem-forming dripwaters has been shown to significantly alter the availability of these metals for incorporation into speleothem calcite. This study therefore aimed to investigate the partitioning behaviour of Co, Ni and Cu into

calcite precipitated under karst-analogue conditions and in the presence of organic ligands to help establish these metals as viable speleothem-based paleoclimate proxies.

In order to do this, a suitable method for growing calcite under karst-analogue conditions was first established. All experiments were undertaken inside a purpose-built chamber that ensured precise control of temperature, humidity and pCO_2, and calcite was grown in a manner analogous to that observed for natural speleothems, with calcite precipitation occurring as a result of CO_2 degassing from a thin solution film. Observed growth rates and structural characterisation of the precipitated $CaCO_3$ indicated the method developed was suitable for the desired purpose, and the partitioning data obtained subsequently was considered to be applicable to 'real-world' speleothem and cave dripwater samples.

The partitioning behaviour of Co, Ni and Cu into calcite grown under speleothem-like conditions was assessed, and speleothem-specific K_d values of ~ 4, 1 and 44, respectively, were determined. The relatively high inorganic K_d values determined for Co and Cu illustrate the reason why these divalent metals have frequently been overlooked as paleoclimate proxies in speleothems: metals with high partition coefficients are thought to exhibit complex partitioning behaviour and are significantly affected by PCP. However, further experiments carried out with organic ligands present in solution illustrated that the complexation of Co, Ni and Cu by nitrilotriacetic acid (NTA) and Suwanee River fulvic acid (SRFA) significantly altered their partitioning behaviour, with apparent partition coefficients reduced below 1 for all three metals. It was shown that partitioning of Co, Ni and Cu into calcite was controlled not only by their affinity for the calcite lattice (i.e. inorganic K_d values) but also by the dissociation of the metal-ligand complexes, and that the amount of 'free' metal available for incorporation into calcite was dependent on residence time and the dissociation constants of the complexes.

The results found in this study highlight the fact that the incorporation of the divalent first-row transition metals into speleothem calcite cannot be considered in terms of simple inorganic partitioning, as the widespread presence of NOM in karst systems will alter their partitioning behaviour significantly. Thus, although the use

of these metals as speleothem-based proxies has previously been overlooked in favour of elements such as the alkali earth metals which exhibit simple partitioning (i.e. $K_d << 1$), in reality the NOM present in karst systems will reduce the effects of PCP on these divalent first-row metals, and they should in fact be considered as useful additions to the current range of paleo-proxies used.

Acknowledgements

First and foremost I would like to thank my supervisor Dr Adam Hartland. You have given me the most amazing opportunities throughout my Master's degree, and I cannot thank you enough for them. Your patience, wisdom and support over this time are wholeheartedly appreciated. You are a truly inspiring scientist and I consider myself incredibly lucky to have had the opportunity to worth with you.

I am very thankful for the scholarships I have received to support me through this journey. My sincere thanks go to the William Georgetti Scholarship Trust, the University of Waikato and the Woman's Graduate Trust for your financial assistance. To Gwenda Pennington, thank you for believing in me and for helping me with my scholarship applications. I am sure they would not have been successful without your help. I would also like to thank the European Union's Horizon Research and Innovation programme for providing funding for overseas travel via the QUEST (QUantitative palaeoEnvironments from SpeleoThems) project.

Thank you to all the members of QUEST, especially Seb and Ola, for welcoming me into the speleo-family and teaching me so much. To Denis Scholz and his team at the Johannes Gutenberg University, thank you for an amazing two months in Germany and for teaching me everything I know about crystal growth experiments. Thanks to Matthias Magiera for being the best lab partner anyone could ever hope for, and to Maximilian Hansen for being a great friend and mentor, and always being available to answer my questions.

This project would have been impossible without the amazing technical and academic staff at the University of Waikato. Peter Jarman and Huw Alderman, thank you for building me my very own cave, putting up with my constant requests for adjustments, and always making me laugh. To Jenny Stockdill, Annie Barker and Karla Watson; thank you for the banter, and for always being willing to help. Thanks to Kirsty Vincent for being so helpful with pXRD analysis, to Helen Turner for assistance with SEM analysis and to Steve Newcombe for painstakingly sandblasting the glass plates whenever I needed them. A big thank you to Amanda

French for your ICP-MS expertise and for always being available to brainstorm, and to Dr Megan Grainger for being a mentor and a constant inspiration.

I would also like to thank all the members of the Waikato Environmental Geochemistry (WEG) group, especially Seb and Andy for always being available to talk things through with me. I have wholeheartedly enjoyed working alongside you all and wish you all the best for the future. Brittany, thank you for helping me whenever I needed help, reassuring me whenever I needed reassuring and inspiring me on the regular to be an awesome scientist.

I would also like to thank the members of the Chemistry Social Club for keeping me sane and supporting me throughout this journey. Thank you Emily, Greer, Nyssa, Ryland, Thomas and Yanan for always having my back and making me laugh when I most needed it. I could not have done this without you guys. A special thank you to Jacob, for being the best friend and study buddy anyone could ask for, for helping me with everything from changing gas cylinders to running LC-MS, and for always having the right memes to make me smile. I hope I can support you a through the final part of your PhD as you supported me.

Hayden, there is no doubt in my mind that I would not have been able to do this without your help. Thank you for being my sounding board, my proof-reader, and my chef while I was writing. No one makes spaghetti on toast like you. Thank you for always reassuring me that I could get this done and for cheering me up when I needed it most. Whakawhetai ki a koe.

Finally, I would like to thank my family for their unwavering love and support. To my parents, Jill and Reinier, my sisters, Alice and Sylvia and my grandmothers Brenda and Miep. You have always believed in me, even when I didn't, and encouraged me to keep going when I thought I couldn't. You made sure I looked after myself and reminded me that there is a whole world out there that isn't my thesis. I cannot thank you all enough for the love and support you have shown me throughout my life.

Table of Contents

List of Figures

List of Tables

1 Background and Literature Review

1.1 Introduction

Cavers and tourists in Aotearoa (New Zealand) and around the world explore and marvel at the unique subterranean features formed by mineral deposits in caves. However it has become increasingly apparent that these features may not have value only in their ability to impress tourists, but they also hold within them clues to help us reconstruct past environments.[1-2] Over the past half-century, significant amounts of research into the geochemistry of $CaCO_3$ cave formations such as stalagmites, stalactites and flow stones (collectively known as speleothems, **Figure 1.1**) have been carried out in order to help researchers to use them as paleoclimate records.[1-8]

Speleothems may contain within their growth layers information on past events and past climatic conditions. Not only are major events such as bushfires and volcanic eruptions potentially recorded within them, but also indicators of past climatic conditions including temperature and rainfall.[1, 9] These events are 'recorded' in the form of various geochemical signals, referred to as 'proxies', that respond systematically to changes in environment. Examples include stable isotope ratios, organic material and trace element content. If these signals can be measured in each growth layer, it is possible to make inferences about past environmental conditions over the time that the speleothem was growing. Speleothem science is thus a field of vital importance to climate scientists (and no-doubt society as a whole) as understanding environmental conditions throughout the geological record allows us to advance our understanding of Earth's current climate systems and the effects of anthropogenic activities on these systems. Reconstructions of paleoclimate from archives such as speleothems can be used to inform climate models that predict climatic processes, and these models are now essential for us to understand and to combat the effects of anthropogenic climate change.

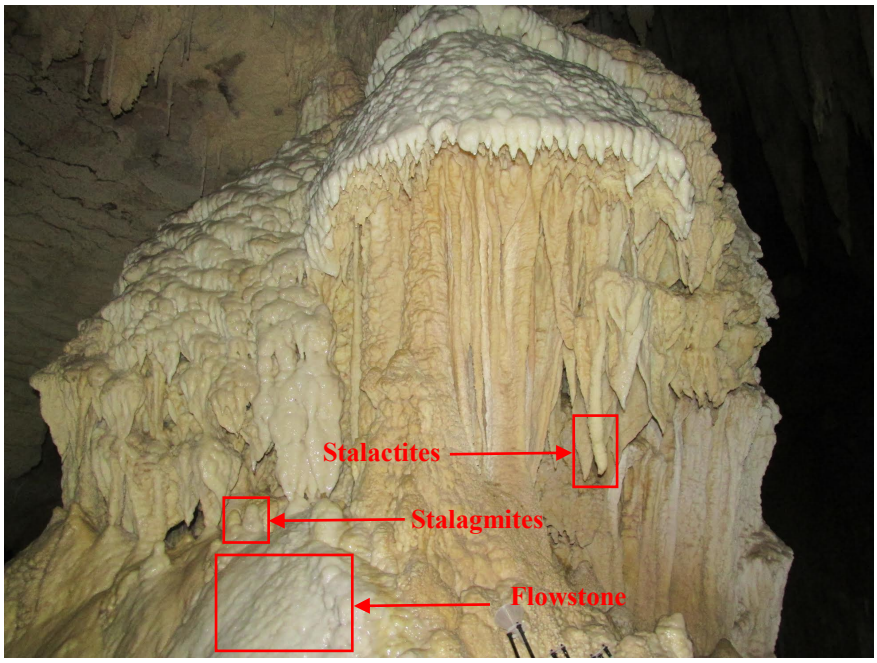

Figure 1.1. A group of speleothems in Waipuna cave, Waitomo, New Zealand. The red boxes indicate three different speleothem formations that may be used as paleoclimate records: a stalactite, stalagmite and flow stone.

Speleothems are by no means the only paleoclimate records available, and indeed they were overlooked for many years in favour of other paleoclimate archives due to the complex nature of their formation pathways. However recent technological advances and improved understanding of karst hydrology and the formation processes of these archives have ensured speleothems have been extensively studied as paleoclimate archives in recent times. The major advantages of speleothems as paleoclimate archives over other terrestrial records such as lake sediment cores is the age of these records and the high temporal resolution that they provide.[1, 10-11] The high-resolution nature of many speleothems (sub-annual resolution in some cases), and the ability to date their growth layers using U-Th and U-Pb radiometric dating, alongside their extensive geographical coverage, mean that speleothem samples are a fundamental tool for terrestrial paleoclimate reconstruction and for understanding climate-system mechanisms.[1]

Although many speleothem-based proxies have been extensively explored for their ability to provide paleoclimate information, the unambiguous interpretation of these proxies has proven difficult and there is a need for further investigations into other possible proxies to ensure speleothem-based climate reconstructions are robust and reliable. For instance, the signals provided by the stable isotope ratios of oxygen

and carbon ($\delta^{18}O$ and $\delta^{13}C$, respectively) in speleothems have been widely studied and used to provide estimations of past rainfall and temperature variations. However, these isotopic ratios are controlled by multiple factors, and thus careful consideration and assumptions are required in order to delineate the primary origin of these signals in a given archive. Thus, further proxies that can be used alongside $\delta^{18}O$ and $\delta^{13}C$ signals are required to ensure the correct interpretation of these signals. The use of trace metal proxies in speleothem archives has become an increasingly popular method of achieving this, as concentrations of trace metals and trace metal isotope ratios also respond to certain processes that occur in the karst system. However, the range of trace metals currently used is slim, and is usually limited to alkali earth metals such as Sr and Mg as their role in karst systems is comparatively well constrained.

In the past decade however, it has become apparent that first-row transition metals such as Co, Ni and Cu, may provide further assistance in interpreting speleothem archives. These divalent transition metal ions are known to complex strongly with the natural organic matter (NOM) present in karst systems, and this interaction has been identified as the most significant controlling factor during the transport of these transition metals to the site of speleothem deposition.[12-13] It is this interaction between divalent metal ions and organic matter that has been identified as vitally important for the use of first-row transition metals as proxies. There have now been several studies that suggest the dissociation of the metal-NOM complexes at the water-speleothem interface may occur in a predictable way and as a function of time.[14] Thus, past drip rates in caves may be able to be reconstructed from the transition metal signatures recorded in speleothem calcite, as these signatures will be a function of complex dissociation. However, the constraints controlling the incorporation of first-row transition metals into calcite, and the effects of organic ligands on this process, have not been extensively studied. Thus, further studies are necessary to help improve our understanding of the behaviour of such metals in cave systems so that these new proxies can be further developed and utilised as potentially quantitative speleothem-based proxies of paleoclimate.

1.2 Cave Systems and Speleothem Formation

1.2.1 Introduction

In order to design a series of experiments that are of relevance to natural speleothem samples, the hydrological and geochemical processes that occur in real cave systems must be understood and, where possible, replicated. Thus, a brief review of surface-to-cave processes and speleothem formation will be carried out here.

Speleogenesis (the formation of a cave) can occur via various mechanisms involving tectonic forces, pressure, geochemical processes, water erosion, microorganisms, and atmospheric influences.[1] Karst caves are the most common type of cave, and these form in soluble minerals such as dolomite, marble, gypsum, chalk and most commonly, limestone. As the focus of this study is calcium carbonate deposits, only karst caves derived from limestone will be discussed further. In brief, the formation of these caves occurs when limestone is dissolved by acidic groundwater that percolates through faults, joints, and bedding planes. These cracks eventually enlarge to become caves and cave systems.[1]

1.2.2 Surface-to-Cave Processes

The subsurface of a karst landscape is divided into two zones which are defined by the level of the water table. The phreatic zone lies below the water table, and its pore spaces are thus usually saturated year-round.[1] The vadose zone, however, is the area above the water table, and is itself comprised of three layers: the soil (this layer may not be present in some cases), epikarst and lower vadose layers. As the vadose zone lies above the water table, it can be saturated or void of water depending on the time of year, geology, rainfall and above ground vegetation.[1] In the soil zone, high partial pressures of carbon dioxide (pCO_2) are present due to the respiration of microorganisms and root exhalation. High pCO_2 levels ensure that infiltrating water reacts to form carbonic acid (**Equation 1.1**), meaning the water

becomes acidic and can therefore interact and dissolve the carbonate in the lower layers (**Equation 1.2**).[1]

$$H_2O_{(l)} + CO_{2(g)} \rightleftharpoons H_2O_{(l)} + CO_{2(aq)} \rightleftharpoons H_2CO_{3(aq)} \quad (\mathbf{1.1})$$

$$H_2CO_{3(aq)} + CaCO_{3(s)} \rightleftharpoons Ca^{2+}_{(aq)} + 2(HCO_3^-)_{(aq)} \quad (\mathbf{1.2})$$

The soil zone is also where a significant proportion of organic matter (OM) enters into the system (**Figure 1.2**). As meteoric water enters the soil layer, organic matter derived from soil fauna and vegetal detritus becomes mobilised and is carried into the layers below, eventually reaching the growing speleothem surface.[1, 12-13] A wide variety of organic compounds of varying size and polarity comprise this organic matter, and thus a convention has been established to characterise OM into three classes. The largest fraction of OM, known as the particulate fraction, is functionally defined as having solids greater than 1 μm. The colloidal fraction is defined as the OM fraction having solids between 1 nm and 1 μm in size. Finally, the dissolved organic matter fraction (DOM) is characterised by a size of less than 1 nm. Both hydrophilic and hydrophobic compounds comprise OM, and this effects the mobility of OM in the karst system. Lignin-derived and long chain alkane compounds have reduced mobility in the karst system due to their hydrophobic characteristics, while hydrophilic compounds such as organic acids and protein-derived compounds (e.g. amino acids) have a significantly higher mobility.[13] Hydrophilic organic ligands therefore are of more interest in this study because of this increased mobility, and because of their higher affinity for complexation to metal ions. Another source of OM that may be preserved in speleothem records is from microbial communities within the cave/on the speleothem surface,[13] however this organic matter is of little relevance to this study so will not be discussed further.

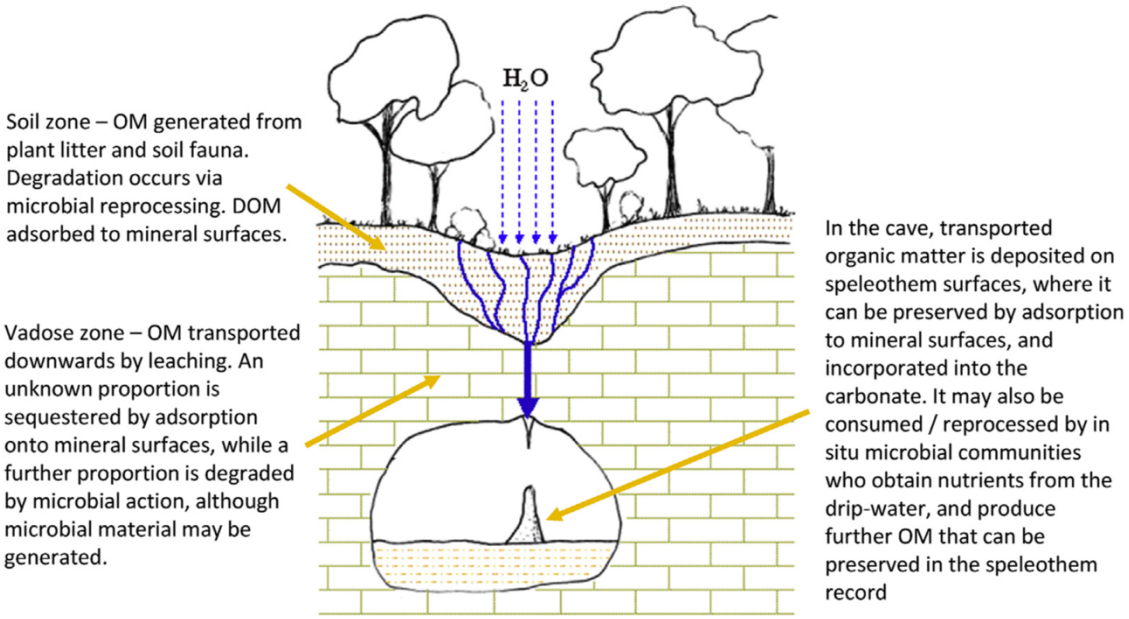

Figure 1.2. Origins and fate of OM in a karst system. Adapted from reference [13].

The second layer of the vadose zone, the epikarst, often acts as an aquifer, a result of low porosity/permeability caused by strong weathering.[15-17] This means the epikarst is often responsible for storing water, and thus is fundamental in dictating the residence time of the water, which can vary significantly on the scale of days to years. The residence time of this water is particularly important for paleoclimate reconstructions as it will impact the signals that are eventually captured within a speleothem archive.[15-17] There are two broad categories of flow through the epikarst: vadose/fracture flow and seepage/diffusive flow.[15] Fracture flow, as the name would suggest, is characterised by fast movement of water through large conduits such as fractures in the bedrock. This occurs only when a saturation threshold of the vadose zone is met. Conversely, seepage flow is characterised by the slow movement of water through sections of bedrock that are of low permeability, and it is this type of flow that is responsible for water storage in the vadose zone. The extent to which OM (and thus complexed metal ions) reaches a growing speleothem at any given time is largely dependent on which flow mode is operating in the vadose zone. For instance, larger fractions of OM are more likely to reach the speleothem surface if fracture flow is present, as they require more energy to be carried through the karst system.[13]

1.2.3 Speleothem Formation

Speleothems form via the precipitation of calcium carbonate (usually in the form of calcite or less frequently, aragonite) from cave drip waters (**Figure 1.3**).[1] As mentioned above, high pCO_2 levels occur in the soil above a cave systems, as a result of microbial respiration and root exhalation. Dissolution of CO_2 results in an acidic solution that dissolves carbonate minerals present in the host rock as it percolates through the soil and epikarst, enriching the water in Ca^{2+} and HCO_3^- ions (**Equation 1.3**).[1] When the water eventually reaches an area of lower pCO_2 (such as a cave), evolution of CO_2 from the solution results in the deposition of $CaCO_3$ (**Equation 1.3**, reverse direction). For instance, during the formation of a stalagmite (the type of speleothem most commonly utilised for paleoclimate reconstructions), infiltrating dripwater forms a thin solution film ~0.1 mm thick on the stalagmite surface.[18-21] The dissolved CO_2 degasses within seconds, causing an increase in pH to around 8, and subsequently HCO_3^- becomes the dominant (~95 %) form of dissolved inorganic carbon (DIC).[22-24] The solution reaches supersaturation with respect to calcite, and thus calcite precipitates as the solution flows down the stalagmite surface.

$$CaCO_{3\,(s)} + CO_{2\,(g)} + H_2O_{\,(l)} \rightleftharpoons Ca^{2+}_{(aq)} + 2HCO_3^-{}_{(aq)} \qquad (\mathbf{1.3})$$

Due to the nature of this process, the growth of speleothems is accretionary, and thus they are able to capture environmental signals continuously over large periods of time.[1] As the speed of $CaCO_3$ deposition on speleothems is dependent on water availability and other factors, the carbonate is frequently deposited in distinguishable growth layers, or laminae (**Figure 1.4**). These layers can have resolution from sub-annual scale to millennial scale and each of the layers may contain information indicative of the environmental conditions affecting water movement and water content when the layer formed.[1-2, 11]

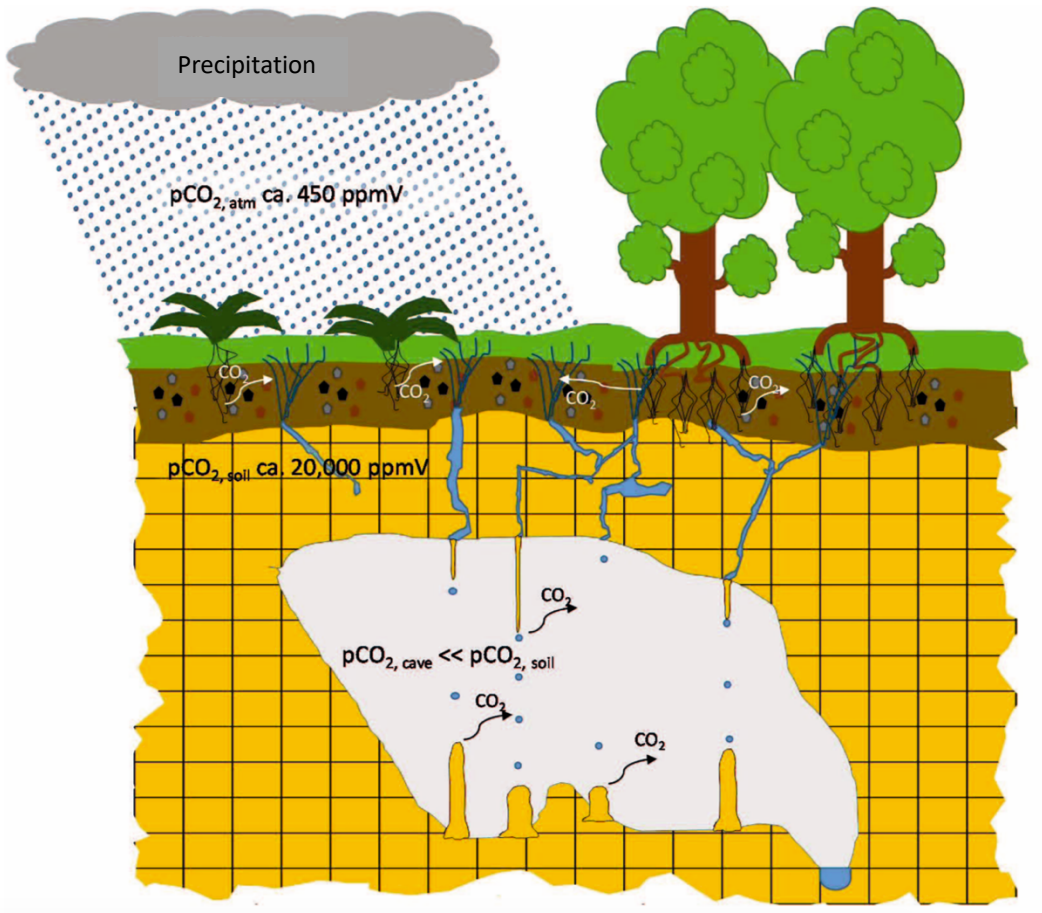

Figure 1.3. Representation of a karst cave system showing the movement of water and CO_2 through the system. Precipitation is followed by the formation of carbonic acid due to uptake of CO_2, causing dissolution of the $CaCO_3$ host rock. Finally, degassing and thus the formation of speleothems inside the cave occurs as a result of the pCO_2 in the cave being less than that of the soil. Figure adapted from reference [20].

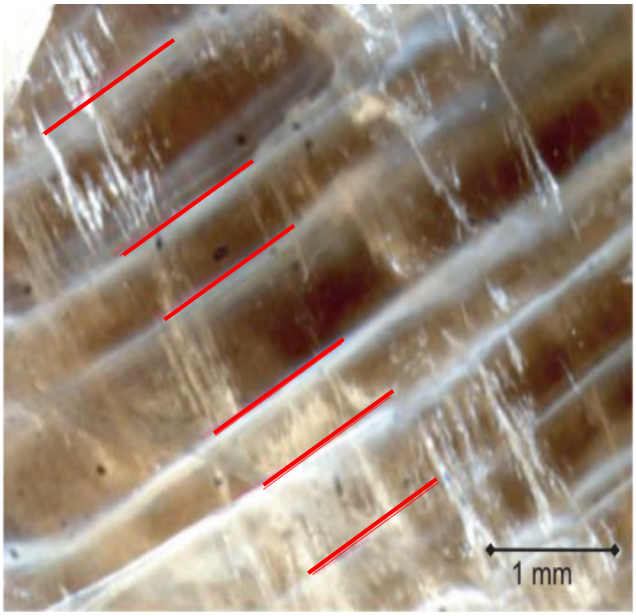

Figure 1.4. Example of visible growth laminae from stalagmite '2pac' found in Akçakale Cave, Gümüşhane province, northeast Turkey. Figure adapted from reference [1].

1.2.4 Calcite Precipitation Rate from a Thin Film

The rate of precipitation of calcite from a thin solution film (such as those found on a speleothem surface) has been well described in the literature.[25-26] The method developed by Buhmann and Dreybrodt (1985) to calculate precipitation rate will be utilised in this study to determine calcite growth rate in each of the experiments, and thus the principles of their method will be discussed here in brief.[26]

It is shown in **Equation 1.3** that as precipitation of one molecule of $CaCO_3$ occurs, one CO_2 molecule is lost. The diffusion and loss of this CO_2 to the atmosphere is almost instantaneous.[18, 22, 26] However in order for the loss of CO_2 to occur, the H_2CO_3 species must convert into H_2O and CO_2 (**Equations 1.1** and **1.2**) and this happens comparatively slowly. Thus the precipitation rate of $CaCO_3$ is limited by the rate of this conversion. Buhmann and Dreybrodt, (1985) combined these processes and derived equations to calculate the precipitation rate, F, of $CaCO_3$ from a thin film:

$$F = \kappa([Ca^{2+}] - [Ca^{2+}]_{eq}) \quad (\mathbf{1.4})$$

$$\kappa = (0.052 + 0.04T + 0.004T^2) \times 10^{-5} \quad (\mathbf{1.5})$$

where κ is a rate constant in cm s^{-1}, $[Ca^{2+}]$ is the concentration of Ca^{2+} at time t, $[Ca^{2+}]_{eq}$ is the concentration of Ca^{2+} at equilibrium (which is dependent on atmospheric pCO_2) and T is the temperature in °C.[26] When this equation is applied to water films as thin as those seen in caves (and indeed in this study), the rate constant κ becomes independent of the film thickness.[23, 27] Thus, as calcite precipitates, calcite supersaturation decreases exponentially according to a characteristic decay time, τ_{pr}, and the change in concentration of Ca^{2+} and HCO_3^- with time can be described by the following equation:

$$[Ca^{2+}](t) = ([Ca^{2+}]_0 - [Ca^{2+}]_{eq})e^{\left(-t/\tau_{pr}\right)} + [Ca^{2+}]_{eq} \quad (\mathbf{1.6})$$

where $[Ca^{2+}]_0$ is the initial concentration of Ca^{2+} at t = 0 and t is the residence time.[22] If the derivative of **Equation 1.6** is taken, the change in concentration of Ca^{2+} over the course of precipitation, and thus growth rate, can be calculated:

$$\frac{d[Ca^{2+}]}{dt} = \frac{1}{\tau_{pr}}([Ca^{2+}]_0 - [Ca^{2+}]_{eq})e^{\left(-t/\tau_{pr}\right)} \quad (\mathbf{1.7})$$

1.2.5 Prior Calcite Precipitation

Prior calcite precipitation (PCP) is a process that can occur before speleothem formation that affects the proxies used for paleoclimate reconstructions. PCP occurs when $CaCO_3$ precipitates from infiltrating water up-flow of the speleothem drip site, when the solution loses CO_2 in aerated (lower pCO_2) channels, caverns, or pores.[28] Rates of PCP are affected by aridity and cave ventilation. Higher rates of PCP are observed during arid periods because there is less water available to fill the pores and caverns where PCP is most likely to occur, enhancing the penetration of air into the aquifer.[28] This results in low pCO_2 and thus precipitation of $CaCO_3$. Similarly, PCP can be affected by cave ventilation as ventilation will change the pCO_2 values within the cave also.[1, 28] As PCP influences various paleoclimate signals in speleothems (including trace metal concentrations) both seasonal cycles and long term trends in aridity and cave ventilation can been observed in speleothem calcite.

1.3 Current Climate Proxies in Speleothems

1.3.1 Introduction

Many useful paleoclimate proxies have been identified and analysed in speleothem samples over the past several decades. Thus only a few of the most notable proxies will be discussed in this section, and only in brief, in order to highlight the impressive potential of speleothems to record paleoclimatic events. The shortfalls of each proxy will also be discussed, in order to highlight the requirement for the

development of further proxies. It should be noted that current trace metal proxies (including their isotopic ratios) will be covered in **Section 1.4** so that they can be discussed in more depth.

1.3.2 Stable Isotope Fractionation

As many paleoclimate proxies in speleothems are based on stable isotopic fractionation, this phenomenon will be briefly reviewed here. Isotopic fractionation occurs as a result of physicochemical processes that affect the relative isotopic abundance of an element due to the slight differences in mass between isotopes.[1, 29] The heavy and light isotopes of an element have different binding energies and therefore different mobilities. The heavier isotopes usually have lower mobilities and higher binding energies, resulting in a slower response than the lighter isotopes during a chemical reaction.[20] This difference in responsiveness leads to isotope fractionation, the magnitude of which is usually expressed by a fractionation factor, α. **Equation 1.8** shows how the fractionation factor is calculated:[20, 29]

$$\alpha_{B/A} = \frac{R_B}{R_A} \qquad (\mathbf{1.8})$$

Where R_A is the isotope ratio in phase A and R_B is the isotope ratio in phase B. As isotopic fractionation is often small, α is usually close to unity and it is therefore convenient to express isotope effects by the fractionation, ε, which can be calculated according to **Equation 1.9**:[20, 29]

$$\varepsilon_{B/A} = (\alpha_{B/A} - 1) \times 1000 \qquad (\mathbf{1.9})$$

Three types of isotope fractionation are presented in the literature. These are equilibrium, kinetic, and disequilibrium fractionation.[20] Equilibrium fractionation occurs when isotopes move between two reservoirs, and the flux in both directions is equal. When there is movement in one direction, and the process is irreversible, kinetic isotope fractionation will dominate.[20, 30] In most natural systems, the overall isotopic fractionation is a result of the combination of these two processes, and is referred to as disequilibrium fractionation.[20]

As would be expected, both kinetic and equilibrium fractionation processes are important in cave environments.[1-2] In his seminal 1971 paper, Chris Hendy describes these processes in terms of $\delta^{13}C$ and $\delta^{18}O$. If loss of CO_2 from the solution is slow, then isotopic equilibrium will exist between $HCO_3^-{}_{(aq)}$ and $CO_{2\,(aq)}$ and the precipitated calcite will also be in equilibrium with the solution. In this instance $\delta^{18}O$ values will depend strongly on climate, while $\delta^{13}C$ values will not. In contrast, if CO_2 loss from the solution is fast, kinetic fractionation may occur between $HCO_3^-{}_{(aq)}$ and $CO_{2\,(aq)}$, and thus the precipitated $CaCO_3$ will have higher $\delta^{18}O$ and $\delta^{13}C$ values. If such kinetic fractionation is observed, paleoenvironmental reconstructions from $\delta^{18}O$ and $\delta^{13}C$ values are confounded.[2]

1.3.3 δ ^{13}C and δ ^{18}O Stable Isotopes

The stable isotopes of oxygen and carbon are widely applied as paleoclimate proxies in speleothems because the isotopic ratios of C and O are known to respond to rainfall and temperature via isotopic fractionation.[1, 10, 20-21, 31] Various studies of speleothem $\delta^{13}C$ and $\delta^{18}O$ have indicated past periods of aridity and high rainfall, supplementing information from other paleoclimate archives such as ice-cores, and illustrating the usefulness of speleothems for aiding understanding of climate-system mechanisms.[32] For instance, the 8.2 ky event (an abrupt and cold period experienced in the North Atlantic region 8,200 years ago) has been well documented in Greenland ice-cores, and recently $\delta^{18}O$ data from a sub-annually resolved stalagmite record from central China has shown that this event was also experienced in the East-Asian monsoon region. $\delta^{18}O$ data from Heshang cave stalagmite HS4 demonstrate a significant period of aridity was experienced in this region, coinciding with the onset of the 8.2 ky event. This in turn demonstrated the existence of teleconnections in the climate system between the North Atlantic and other regions.[32] This is only one example of many where speleothem $\delta^{18}O$ and $\delta^{13}C$ data has been used to qualitatively reconstruct past climatic events, which illustrates the power of speleothems to provide vital information for paleoclimate reconstructions.

Clumped isotopes have recently become a focus of speleothem scientists for use as paleoclimate proxies also.[1, 20] The term ‘clumped isotopes’ refers to chemical

species that are enriched in heavier isotopes of more than one element. Clumped isotopes form because there is a temperature dependent preference for heavy isotopes to bond together in the same molecule. The analysis of clumped isotopes (via the measurement of the various isotopologues of a molecule, in this case CO_2 derived from calcite via acid digestion) has been hindered by analytical capabilities. Measuring the mass 47 isotopologue ($^{13}C^{18}O^{16}O$) is required for clumped isotope analysis in speleothems, and this is difficult due to its very low abundance. Recent advances in analytical techniques mean that clumped isotope analysis is now a viable option for paleoclimate reconstructions, although many analytical difficulties are still faced when using this technique. It should be noted that despite the major influence of temperature on the formation of clumped isotopes in cave systems (due to the strength of the $^{13}C^{18}O$ bond), kinetic processes are still present which do not allow fully quantitative reconstructions of temperature to be made.[1]

Despite the ability of $\delta^{13}C$, $\delta^{18}O$ and clumped isotopes proxies in speleothems to reveal past trends in air temperature and rainfall variations, the interpretation of the data is hampered by a multitude of other factors that affect the isotopic fractionation of C and O, including kinetic fractionation.[1, 7, 19, 33] Complex processes that occur in the soil, epikarst and cave make the unambiguous interpretation of stable isotope data highly difficult: $\delta^{13}C$ and $\delta^{18}O$ proxies are not as robust and reliable as needed. Thus, past rainfall and temperature variability can only be inferred. Quantitative reconstructions using these proxies are not currently possible, and therefore further research into proxies such as those investigated in this study is needed so that they can be used alongside the already powerful proxies discussed above. Hopefully with the development of further proxies, a multi-proxy approach to paleoreconstructions can be used to allow unambiguous interpretations of speleothem archives.

1.3.4 Natural Organic Matter (NOM) Proxies

The amount and type of organic matter that reaches a growing speleothem is dictated to a large degree by climatic and ecological processes. Thus there has been particular interest in the past two decades in developing new speleothem-based NOM proxies that can be used alongside inorganic proxies to provide

comprehensive reconstructions of paleoclimate and also provide insight into changes in vegetation above cave systems.[12-13, 34-37] A recent review provided by Blyth *et al.* (2016) outlines this promising area of speleothem science, and provides a discussion on the association between trace metals and organic matter in karst systems.[13] This review outlines some more recently developed approaches to using OM for paleo-reconstructions, including analysis of specific plant-derived biomarkers such as *n*-alkanes and analysis of compound-specific $\delta^{13}C$ values in OM isolated from speleothem samples.[13, 35] These newer approaches, however, are of little relevance to this study so will not be discussed further.

Of more relevance to this study is the 'traditional' fluorescence analysis of speleothem-derived organic matter.[13] This approach utilises the absorption of high energy UV–visible light by OM as electrons are excited above their ground state, and the subsequent emission of fluorescence as the electrons return to the ground state.[38] The wavelength of the emitted fluorescence can provide qualitative information on the OM present in the sample, while the intensity of the fluorescence is indicative of OM quantity. For instance, OM with delocalised (and thus readily excitable) electrons (i.e. aromatic groups) typically emit fluorescence in the 360-450 nm wavelength range. If fewer aromatic groups are present, fluorescence emissions are usually within the 300-350 nm range.[38] Cumberland and Baker (2007) have shown that the emission wavelength of the OM can be used to make inferences about the decomposition of OM in the karst system, with higher energy (shorter wavelength) emissions indicating a higher level of biological decomposition occurring in the soil zone, and lower energy (longer wavelength) emissions indicating less decomposed OM.[34] This fluorescence technique can also be used to provide information on the quality and quantity of OM present in cave dripwaters, and this quantitative approach will be used on the solution samples collected during the experiments in this study to determine the extent to which organic material has been incorporated into the $CaCO_3$ precipitates.[12]

1.4 Trace Metals as Proxies in Speleothems

1.4.1 Introduction

The development of techniques such as Inductively-Coupled Plasma Optical Emission Spectrometry (ICP-OES) and Inductively-Coupled Plasma Mass Spectrometry (ICP-MS) have allowed relatively easy quantitation of trace elements in both speleothems and cave dripwaters. This, coupled with the fact that they are known to respond to environmental variables, mean trace elements have become a major focus of speleothem scientists for their use as climate proxies. [4-6, 20, 39-40] Such studies have previously focused primarily on the alkali earth metals Mg, Sr and Ba, and comparatively little attention has been given to other divalent metals such as the first-row transition metals. A brief review of the controls on elemental partitioning into speleothems will be given below, followed by a review of the established applications for trace alkali earth metals in speleothems. Finally, the few data pertaining to first-row transition metals in speleothems and cave dripwaters will be presented and a discussion of the potential for these metals to be used as powerful paleoclimate proxies will be undertaken.

1.4.2 Elemental Partitioning into Speleothems

In order to interpret trace element signals in speleothem carbonates, the partitioning behaviour of trace elements into calcium carbonate minerals must be understood. Trace element incorporation at the speleothem surface is known to respond to a number of factors, including temperature, the growth rate of calcite and characteristics of the drip solution, and thus although trace element data has the potential to yield valuable information about past climate, the contribution of each of these factors must be well understood in order for accurate and unambiguous interpretations to be made.[1, 5]

Three main processes of trace element incorporation into minerals have been discussed in the literature since being defined by McIntire in 1963.[41] These are surface adsorption, occlusion, and solid solution formation. Surface adsorption occurs when the foreign ions have weak bonding interactions with the surface ions

of the mineral whose bonding is not yet completely satisfied. This process is of most importance in colloidal or aggregate minerals, as the energy of surface adsorption increases with surface area. Due to the nature of the $CaCO_3$ grown in this study, this mode of incorporation will not be vastly important and thus will not be extensively discussed. The partitioning of trace elements via occlusion occurs when trace elements are adsorbed at the surface and then are subsequently 'trapped' when the next mineral layer grows over them. Occlusion can explain fluid inclusions in speleothems, as fluid present during precipitation can be 'trapped' in a similar manner, often in the presence of trace elements also. This process is of most importance during high rates of precipitation.[1] Finally, trace elements may be incorporated into a mineral lattice via substitution within the crystal lattice. In the case of calcite, divalent trace metals can substitute for a Ca^{2+} ion. As you would expect, the ionic radius and valency of the elemental impurity is particularly important for this process, and divalent ions of similar ionic radii to the divalent calcium ion are most likely to incorporate in this manner.[1, 41 42] As the metal ions used in this study are all divalent and comparatively similar in ionic radii to Ca^{2+}, this mode of partitioning will be assumed to be the dominant mode. However further experiments investigating the local coordination geometries of the trace impurities would be recommended to confirm this.

Partitioning of trace metals into calcite was historically described by a parameter known as the distribution constant, or K_D, based on the equilibrium partitioning of an element X between two phases.[43] This parameter provided a way of describing the extent to which a trace element was partitioned between an aqueous phase and a mineral phase (e.g. calcite). This partitioning is represented in **Equation 1.10**:

$$X_{phase\ A} \rightleftharpoons X_{phase\ B} \qquad \textbf{(1.10)}$$

The equilibrium constant of **Equation 1.10** is given by **Equation 1.11**:

$$K = \frac{a_{X_{phase\ B}}}{a_{X_{phase\ A}}} \qquad \textbf{(1.11)}$$

where a is activity. In order for the equilibrium constant K to be equal to the concentration ratios of the element X between phases B and A, the activity coefficients of X in each phase must be the same.[43] Under these conditions, the equilibrium constant (and thus also the concentration ratio) is equal to the distribution constant by K_D. However, these conditions are very rarely obtained, and thus distribution constants have become almost redundant in favour of a similar but distinct parameter, the partition coefficient.[43]

The partition coefficient (sometimes also referred to as the distribution coefficient) was first introduced in 1927 by Henderson and Kraček and, unlike the distribution constant, is non-thermodynamic. [43, 44] Either D_X or K_d is usually used to represent the partition coefficient, where X is the trace element of interest. The partition coefficient, like the distribution constant, is used to relate the trace element content of a mineral phase to that of the solution phase from which it precipitated but is normalised to the concentration of the 'carrier' element. In the case of calcite, the carrier element is calcium (**Equation 1.12**). The non-thermodynamic nature of the partition coefficient renders it preferable, as thermodynamic equilibrium is rarely, if ever, obtained in either laboratory experiments or natural systems under near Earth surface conditions.[43] Experimentally determined partition coefficients for the most part do not reflect equilibrium, but are simply phenomenological measurements for a given set of conditions.[43] As such, they are influenced by a host of parameters beyond the thermodynamic variables of temperature, pressure and composition, and thus although partition coefficients measured in the laboratory can give valuable insight into the processes governing the composition of solids, they can rarely be quantitatively applied to understanding the composition of precipitates in nature.[43]

$$K_d = \frac{[X/Ca]_{CaCO_3}}{[X/Ca]_{aqueous}} \qquad \textbf{(1.12)}$$

Equation 1.12 dictates that a $K_d > 1$ indicates preferential incorporation of the trace element X into calcite, while a $K_d < 1$ indicates Ca is preferably incorporated into the $CaCO_3$ lattice. [4-6, 45-46]

Many partition coefficients for a range of trace elements have been both calculated and determined experimentally for calcite, and in particular for speleothem samples.[6, 46-48] In order to fully interpret and understand the resultant K_d values, all the factors affecting trace element partitioning and the modes of incorporation of trace elements, must be considered. It has already been stated that the partitioning of trace elements can be affected by a wide variety of factors including the steric and electronic properties of the element, temperature, calcite growth rate, organic ligand binding and trace element concentration, however the degree to which each of these factors affects partitioning of trace elements (especially first-row transition metals) into speleothems, is not well understood.[1] Trace element incorporation into calcite remains ambiguous and cannot be regarded as a solely thermodynamic process, and thus, if first-row transition metals are to be used as robust paleoclimate proxies, further work is required to deconvolute the controls on their partitioning[1, 4-7, 31, 40 43]

One of the factors that would not be accounted for in a thermodynamic approach to trace element partitioning into speleothem calcite, but one that hugely influences the partitioning behaviour of trace elements into carbonates, is the effect of complexation by NOM.[1] The effects of NOM on trace element partitioning into speleothems have frequently been overlooked and underestimated, despite the demonstration of the widespread occurrence of trace metal transport via NOM in cave dripwaters.[12] It is now known that many trace metals complex to both dissolved and colloidal NOM in cave systems, and it follows that the effective concentration of these elements in solution (and thus the concentration available for incorporation into calcite) will depend on the lability of these complexes.[12, 36] **Section 1.5** will outline the interactions between trace metals and organic material in more detail.

A thermodynamic approach to trace element partitioning into calcite would also not take into account the kinetic contribution that occurs due to certain areas of the crystal surface having features that promote the incorporation of trace elements.[42] Certain areas may become more enriched in trace elements than others due to morphological and energetic differences between sites.[1, 42] Different areas of the crystal surface may have different features, such as kinks and screws, which can affect the adsorption of trace metals onto the surface.[42, 49-50] Therefore a simple

thermodynamic approach is insufficient to determine trace element partitioning, and the surface features of calcite crystals should be taken into account when investigations into trace element partitioning in speleothems are undertaken.[4]

Figure 1.5 illustrates the 'sector zoning' concept proposed by Paquette and Reeder in 1995, which accounts for the different coordination environments of a trace element *X* in calcite.[42] Here, two distinct growth steps which differ in the direction they translate can be seen. Scheme A illustrates a $\left[\overline{4}41\right]_{+/+}$ kink site in calcite, while scheme B illustrates a $\left[\overline{4}41\right]_{-/-}$ kink site. At the $\left[\overline{4}41\right]_{+/+}$ kink site the trace element *X* is coordinated to three oxygen atoms all within the same growth layer (the upper dark grey layer). Conversely, scheme B shows that at the $\left[\overline{4}41\right]_{-/-}$ kink site, *X* is coordinated to two oxygen atoms in the top growth layer (dark grey) and one oxygen atom in the bottom layer (light grey). Differences in direction of the coordinated bonds to the calcite faces between the two different schemes were also noted by Paquette and Reeder (1995). These differences in the coordination environment of *X* lead $\left[\overline{4}41\right]_{+/+}$ kink sites to be the more open of the two systems, thus favouring ions with larger radii (e.g. Sr^{2+} and Ba^{2+}) while the $\left[\overline{4}41\right]_{-/-}$ kink site favours ions with smaller radii (e.g. Co^{2+}, Cd^{2+} or Mg^{2+}). This phenomenon is thought to be most important in systems with slow mineral growth rates. [42]

The growth rate of carbonate minerals is also an important controlling parameter on trace element partitioning that heavily influences apparent K_d values.[43] An increasing growth rate may either increase or decrease the partition coefficient, depending on whether it is a compatible element (e.g. Cd^{2+}) or an incompatible element (e.g. Sr^{2+}). Partition coefficients of an incompatible element will usually increase with precipitation rate, while the converse is true for compatible elements.[42-43] It should also be mentioned that temperature has been shown to significantly effect partitioning of several trace elements, however as the temperature will be held constant for all experiments in this study, this phenomenon will not be discussed further. [4, 46, 51]

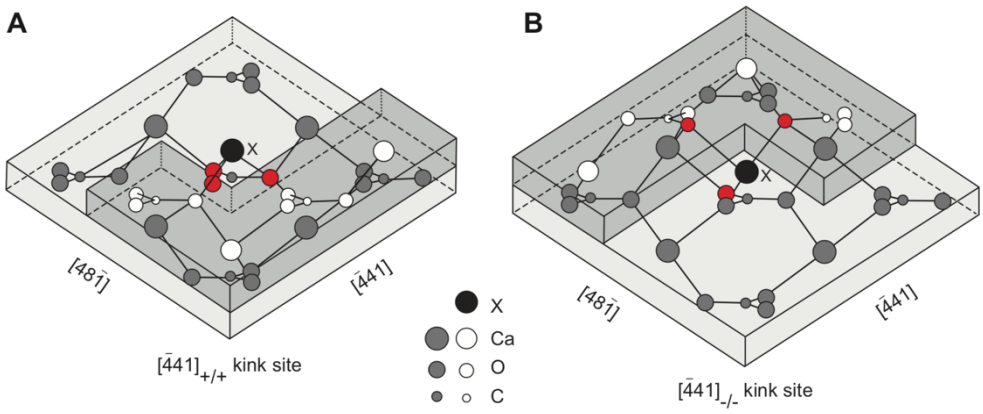

Figure 1.5. Illustration of the different coordination environments of a trace element (X) at two different kink sites in calcite. The light grey shaded areas represents the lower mineral layers, while the dark grey shaded areas represent the upper growth layer. White circles indicate atoms in the upper growth layer, grey circles represent the elements in the lower layers and red circles indicate oxygen atoms directly coordinated to the trace metal impurity. Scheme A indicates a $\left[\bar{4}41\right]_{+/+}$ kink site in calcite where the trace element X is coordinated to three oxygen atoms all within the same growth layer. Scheme B illustrates a $\left[\bar{4}41\right]_{-/-}$ kink site where X is coordinated to two oxygen atoms in the top growth layer and one oxygen atom in the bottom layer. The $\left[\bar{4}41\right]_{+/+}$ kink site is more open, thus favouring ions with larger radii while the $\left[\bar{4}41\right]_{-/-}$ kink site favours ions with smaller radii. Figure taken from reference [42].

1.4.3 Isotopic Fractionation During Elemental Partitioning into Calcite

Another factor that should be taken into account when developing speleothem-based trace element proxies is the potential isotopic fractionation that occurs as a result of partitioning from the aqueous phase into $CaCO_3$ minerals. [52] For instance, the light isotopes of the alkali earth metals are enriched in calcite due to steric effects. Schott *et al.* (2014) demonstrated this in a series of experimental studies investigating the effects of crystal growth rates, fluid pH and speciation on the isotopic composition of divalent metals incorporated into a calcite lattice. [1, 52] They also demonstrated that the isotopic fractionation of Mg decreases with increasing calcite growth rate, while Ca, Ba and Sr show an increase in isotopic fractionation during periods of increased growth rates. They attributed this to the higher lability of H_2O ligands in the hydration spheres of the four heavier alkali earth metals. They also found that divalent first-row transition metals showed the opposite trend- a slight enrichment of heavy isotopes of Zn, Cu, Cd and Ni were observed in the

precipitated calcite, as would be expected due to the higher affinity of these metals for the mineral phase ($K_d > 1$). The fractionation of these elements was shown to decrease with increasing growth rates. In the same study, Schott *et al.* investigated the effects of RO^- ligands on the resulting isotopic fractionation between the aqueous solution and calcite. They demonstrated that for transition metals such as Cu which bind ligands strongly (see **Section 1.5.3**), the equilibrium isotope distribution between aqueous solutions and calcite depends on solution pH, $\Sigma CO_{2(aq)}$ and the presence of aqueous ligands. This will be covered in more detail in **Section 1.5.5**, below. [52]

1.4.4 Established Applications of Trace Metal Proxies in Speleothems

Despite the aforementioned concern by some that trace element partitioning is ambiguous and cannot be easily used for quantitative paleoclimate reconstructions, many successful studies have used trace element proxies in speleothems to provide information on past aridity.[1] The most commonly used elements for these reconstructions are the alkali earth metals Sr, Mg and to a lesser extent, Ba, as they exhibit simple partitioning ($K_d << 1$) and the role of these elements in the karst system is comparatively well-constrained. Gaining information on past aridity via these proxies is possible because X/Ca proxies (where X is Sr, Mg or Ba) are known to reflect levels of PCP in the karst system (although this is of course not the only factor affecting X/Ca values in speleothem samples and cave dripwaters). [1,7] One of the most well documented effects of PCP is the shift to higher Sr/Ca and Mg/Ca values as PCP increases (**Figure 1.6**). Dripwater solutions, and thus also speleothems, are enriched in these alkaline earth elements when PCP occurs up-flow of the speleothem, as both $K_{d\text{-}Mg}$ and $K_{d\text{-}Sr} << 1$ (i.e. calcium ions are preferentially incorporated into calcite over trace element ions). Subsequently, higher levels of these trace elements are present in the dripwater at the growing speleothem surface, resulting in higher X/Ca values in the growing speleothem calcite.

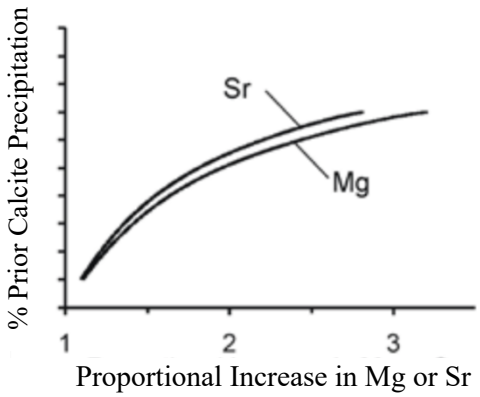

Figure 1.6. Graph showing the expected increase in Sr and Mg as PCP increases. Taken from Fairchild & McMillan (2006).[54]

Many studies utilising alkali earth metals as paleoproxies in speleothems have been undertaken. Liu *et al.* (2013) for instance used Mg/Ca data from the HS4 stalagmite to support the $\delta^{18}O$ evidence for aridity in the East-Asian monsoon region during the 8.2 ky event.[32] Similarly, Zhou *et al*. (2011) used Mg/Ca, Sr/Ca and Ba/Ca ratios from stalagmite SZ2 (from Suozi Cave in Sichuan province, Central China) to demonstrate changes in past climate and environment during Marine Isotope Stages (MIS) 5c and 5d.[53] They suggested temperature to be the dominant control on the Mg/Ca ratios observed, and PCP to be one of the main influences on the Sr/Ca and Ba/Ca ratios observed.

It should be noted that PCP is not only affected by water availability, but also by changes in CO_2 concentrations caused by moisture-independent factors such as cave ventilation dynamics and changes in respiration rates of microbes and vegetation. Both variations in soil CO_2 and cave ventilation are often seasonal and may either increase or decrease the amount of PCP observed. As the extent to which moisture independent and moisture dependent processes affect PCP is not well known, caution should be taken when using proxies affected by PCP (such as trace elements) to reconstruct hydroclimate.

Two other major factors controlling the X/Ca ratios in dripwater and speleothems are the mixing of different sources of dissolved metals, and water-rock interactions. Although both processes are important in interpreting X/Ca proxies, they are of little relevance to the study presented here so will only be covered in brief. With regards to mixing from different sources, a speleothem may be fed with a solution

containing cations from both a Ca enriched limestone source and an 'exotic' source enriched in a trace element. In this situation, the X/Ca ratio of the dripwater will be greatly dependent on the proportion of solution infiltrating from each source at a given time. The effects of PCP and source mixing on X/Ca can sometimes be distinguished by the use of trace element isotope ratios (e.g. Mg).[28]

Water-rock interactions can influence X/Ca values through two processes: incongruent dissolution and bedrock crystallisation. When incongruent dissolution occurs, infiltrating water dissolves bedrock and in doing so preferentially dissolves the alkali earth metals over calcium, increasing the trace element content of the speleothem-forming dripwater. When bedrock recrystallisation occurs, the bedrock recrystalises after infiltrating water has dissolved it, preferentially incorporating calcium over the alkali earth metals, again increasing X/Ca values in the water. As PCP and water-rock interactions have similar effects on the trace element content of the infiltrating water, but reflect opposite trends in hydroavailability, care must be taken when interpreting these trace element proxies. However Sinclair (2011) has developed a mathematical approach to calculate the extent to which PCP, water-rock interactions, and other karst processes have affected X/Ca values of the infiltrating water based on the partition coefficients of Mg and Sr.[55]

1.4.5 Transition Metals in Speleothems as Promising Paleoclimate Proxies

Few studies have investigated the incorporation of transition metals into speleothem calcite, primarily because of the high partition coefficients ($K_d > 1$) predicted for these metals when compared to the alkali earth metals. However, there is now evidence that they may be useful additions to the speleothem-based proxies already used. As this study is investigating Co, Ni and Cu, most of this section will be focused on these three transition metals.

There are several reasons why Co, Ni and Cu may be good candidates for novel paleoclimate proxies. They are abundant members of the first-row transition metals, are present in both cave waters and speleothems, and, being transition metals, they exhibit a range of behaviours that are not shown by the alkali earth metals. Notably, they complex strongly to organic ligands, and the strong complexation of these

elements by NOM should significantly alter both their availability for incorporation into calcite and their isotopic fractionation. Indeed, previous studies have shown a strong correlation between transition metal concentrations and fluorescent laminae in speleothem samples, indicating that trace metals and organic material may be associated within speleothems.[56] In a speleothem sample from Grotto di Ernesto in Italy for example, Borsato *et al.* (2007) found that trace elements (including some first-row transition metals) were enriched in layers alongside NOM. They found that concentration of the elements in these layers were ordered as follows: Y > Zn, Cu, Pb > P and Br, a hierarchy reflecting the selectivity of transport by organic colloids flushed from the soil zone during seasonal infiltration events. Further studies in this area are in agreement with the conclusions drawn by Borsato *et al.* (2007) (e.g. Hartland *et al.* 2012), and these will be covered in detail in **Section 1.5.4**.

1.5 Trace Metal Complexation With Organic Matter in a Karst System

1.5.1 Introduction

It has now been established that if the proposed trace transition metals are to be used as paleoclimate proxies in speleothems, their complexation to organic matter must first be well characterised and understood. Thus, the principles of metal ion complexation will be discussed here, with a specific focus on the complexation of first-row transition metals with NOM.

1.5.2 Characteristics of Organic Complexing Agents in Natural Waters

The vast majority of organic complexing agents in natural waters are humic substances, derived from the decomposition of plant residues. Humic substances are composed of a wide range of organic molecules with varying molecule weights and functional groups and can thus be difficult to fully characterise. However, they are frequently categorised into three distinct fractions: humin, humic acid (HA) and fulvic acid (FA).[57-60] Humin is defined as the fraction of humic substances that is

insoluble after alkali extraction, and is of little relevance to this study so will not be discussed further. The HA fraction is defined as the fraction that is soluble in aqueous solutions only when the pH of the solution is above 2. HA is usually composed of high molecular weight compounds with few oxygen containing functional groups. Conversely, FA is soluble at any pH, composed of lower molecular weight organic compounds, and constitutes the majority of NOM present in freshwater systems. [57-60]

The main mode of metal ion complexation from NOM is through oxygen-containing (i.e. electron donating) functional groups in HA and FA such as carboxyl and phenolic groups.[57] As the proportion of such groups varies significantly between HA and FA, the relative concentrations of HA and FA in fresh water systems is important in determining the amount of metal ions bound to NOM and the strength of the complexes formed. It has been shown that the relative concentrations of HA and FA in caves can vary significantly, and this will have significant implications for the metal species present in cave dripwaters and thus speleothems.[12]

1.5.3 Principles of Metal-Ligand Complexation

Recent studies investigating first-row transition metals in cave dripwaters have shown that the rate of dissociation of metal-ligand complexes (denoted ML) is a dominant factor in determining the availability of these metals for incorporation into speleothem calcite. [40, 61] Therefore concepts relevant to the dissociation rate of such complexes will be discussed here.

The rate of dissociation of a ML complex is dependent on the two factors: the rate of formation of the complex and the stability of the complex.[62] For the reaction:

$$L + M \underset{k_{\text{diss}}}{\overset{k_{\text{form}}}{\rightleftharpoons}} ML \qquad (\mathbf{1.13})$$

the dissociation constant of the complex (k_{diss}) can be calculated from the formation constant of the complex (k_{form}) and the stability constant, K, according to the following equation:

$$k_{diss} = \frac{k_{form}}{K} \qquad \textbf{(1.14)}$$

Factors that determine the magnitude of the formation and stability constants of aqueous complexes will be discussed here.

The formation of metal-ligand complexes in aqueous solutions can be described by an associative substitution pathway known as the eigen mechanism, in which a ligand first associates with a fully hydrated metal cation in the outer coordination sphere. Loss of a water molecule from the inner coordination sphere allows the coordination of the ligand in the inner sphere. This two-step process is outlined in **Figure 1.7** for a divalent metal cation, M^{2+}, that forms octahedral complexes (e.g. Cu^{2+}, Ni^{2+}, Co^{2+}). The ligand, L, is assumed to be monodentate in this representation, however it should be noted that naturally occurring organic complexants are frequently polydentate. The second step in the reaction pathway outlined below (i.e. loss of the water molecule) occurs on much longer timescales than the association of the ligand, meaning this is the rate determining step that dictates the timescale on which organo-metal complexes are formed (and thus also the magnitude of k_{form}). Eigen and Wilkins (1965) illustrated that the rate constant for the loss of any ligand is specific for each metal cation, based on its electron configuration and oxidation state. For instance, the rate of exchange of a coordinated water molecule is known to be 3 x 10^4 s^{-1} for Ni^{2+}, 2 x 10^6 s^{-1} for Co^{2+} and 3 x 10^9 s^{-1} for Cu^{2+}, indicating organo-metal complexes will form most quickly in aqueous solutions for Cu^{2+}, then Co^{2+} and then Ni^{2+}.[63-64]

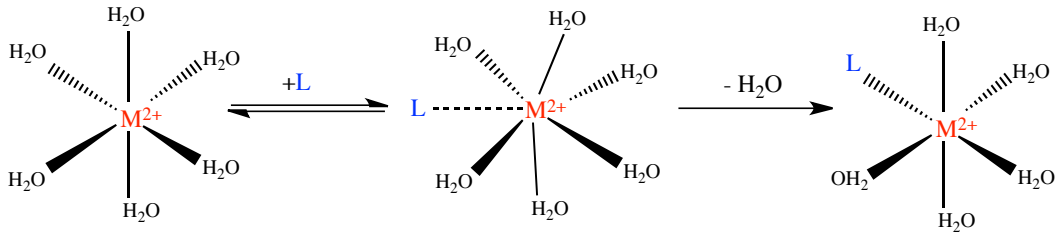

Figure 1.7. The eigen mechanism. A fully hydrated metal cation (M^{2+}) forms an intermediate complex with ligand L. In the second (rate determining) step a water molecule is substituted out for the ligand.

Stability constants of metal-ligand complexes are useful measures of the strength of interaction between a cation and ligand. The magnitude of a stability constant is governed by various factors, including the denticity and aromaticity of the ligands involved, electrostatic effects and Ligand Field Stabilisation Energy (LFSE). For the reaction **1.13**, above, the stability constant, *K*, is given by:

$$K = \frac{[ML]}{[L][M]} \qquad (\mathbf{1.15})$$

The chelate effect describes the effect of denticity on stability constants. Briefly, the substitution of a polydentate ligand for monodentate ligands (such as water) in a complex increases the disorder of the system and thus the entropy, thereby increasing the stability of the chelated complex. As the NOM in karst systems typically binds through carboxylic and phenolic functional groups, and both of these groups have been shown to provide bidentate and tridentate binding to metals centres,[65] this effect is likely important in the formation of highly stable metal complexes in karst dripwaters. Ligands that can act as π acceptors as well as σ donors (e.g. aromatic ligands) also form more stable complexes due to the increased donation of electron density to the metal centre. Again, the presence of aromatic groups in NOM is well documented and could contribute to the formation of highly stable metal complexes in dripwaters.

Not only is the nature of the ligand important in determining complex stability, but also the characteristics of the metal centre. All transition metals with *d*-orbital electrons have a high affinity for ligands with electron donating groups (a result of the LFSE that occurs when complexes are formed). The Irvin-Williams series outlines the relative stabilities of complexes formed by divalent first-row transition metal ions, reflecting a combination of both electrostatic effects and LFSE.[66] The stability of complexes formed by these ions generally increase across the row to a maximum stability at copper: Mn(II) < Fe(II) < Co(II) < Ni(II) < Cu(II) > Zn(II). This is consistent with a decrease in ionic radius with increasing atomic number (and thus an increase in charge density). The increase in LFSE from zero for Mn(II) to a maximum at Ni(II) also makes the complexes increasingly stable across the row (note the LFSE for Zn(II) is zero). Cu, however, forms the most stable complexes due to a phenomenon known as the Jahn-Teller distortion which increases the LFSE of Cu complexes even further.[64, 67-68] In brief, the Jahn-Teller

distortion in octahedral Cu complexes occurs because of the d^9 electron configuration of Cu^{2+} and the degeneracy of the two e_g orbitals (d_z^2 and $d_x^2 - d_y^2$). The distortion is effectively an elongation or compression of the axial bonds that removes this degeneracy, thus lowering the electrostatic repulsion between the electron-pair on the ligand and the electrons in orbitals with a *z* component (i.e. d_z^2 and $d_x^2 - d_y^2$). This lowers the overall energy of the complex, increasing its stability further.[69]

Table 1.1, below, shows the stability of divalent Cu^{2+}, Ni^{2+} and Co^{2+} complexes with two strong chelating ligands ethylenediaminetetraacetic acid (EDTA) and nitrilotriacetic acid (NTA) at metal to ligand ratios of 1:1. Data for the corresponding Mg^{2+} complexes are also included for comparison, to show the significant difference in complex stability between the alkali earth metals and the first-row transition metals.

Table 1.1 Stability Constants (Log*K*) reported in the literature for the complexation of Cu^{2+}, Ni^{2+}, Co^{2+} and Mg^{2+} with two chelating ligands, ethylenediaminetetraacetic acid (EDTA) and nitrilotriacetic acid (NTA). [68, 70-71]

Ligand	**EDTA**	**NTA**
Metal Ion	**Log*K***	
Cu^{2+}	18.86	12.96
Ni^{2+}	18.62	11.54
Co^{2+}	16.31	10.30
Mg^{2+}	8.69	5.46

The applicability of the Irvin-William series to the competition for binding sites in NOM has been investigated. Mandal *et al.* (1999) for instance used Competitive Ligand Exchange Method (CLEM) to assess the competitive binding of Cu^{2+}, Ni^{2+} and Co^{2+} for NOM.[64] They found that Cu(II) out-competed Co(II) and Ni(II) for the strong binding sites of the humic substances, which is consistent with the Irvin-Williams series. As all three of these metals are present in the solutions used in this study, it is likely a similar trend will be seen for the ligands utilised.

It should be noted that determination of absolute stability constants such as those listed in **Table 1.1** becomes difficult when the ligands are humic substance, due to their heterogeneous composition and the subsequent inability to characterise their binding sites and determine the 3D structures of the resulting complexes.[59] For small ligands such as EDTA and NTA, the denticity of the ligand and the molecular structure (including stereochemistry) of the complex can be comparatively easily deduced. The concentration of the free ligand [L] in a thermodynamic equilibrium expression such as **Equation 1.15** can therefore be calculated, especially when the concentration of the ligand is in excess. In contrast, this is only possible for humic substances in a restricted sense, as [L] is a model-dependent value.[72-73] Therefore the use of conditional stability constants is required, i.e. stability constants which have been measured under site specific conditions.[59] Therefore literature stability constants for complexes of divalent transition metals and humic substances may not be relevant for conditions such as those found in a karst system or indeed in this study.

1.5.4 Transition Metal Complexation by NOM

In order to fully comprehend the effects of NOM on trace element proxies in speleothems, factors affecting the stability and lability of these complexes must first be understood. A range of modelling, laboratory and field-based studies have assessed these factors, and these will be discussed here.

Firstly, the mode of binding of divalent transition metals by NOM should be discussed due to the effect of denticity on complex stability (see **Section 1.5.3**). Shi *et al.* (2016) used various literature data sets to model the binding modes of NOM and divalent metals, and found polydentate complexes of the first-row transition metals dominate.[65] They suggest bidentate complexes to be the most common, with monodentate complexes considered negligible above pH 5 and tridentate complexes present in the pH range 7-8. Warnken *et al.* (2007) suggested that due to the importance of binding mode on complex stability, a single dissociation constant for a metal-NOM complex is an oversimplification, and a range of dissociation constants for each metal should be expected depending on the NOM quantity and composition and solution composition.[57, 74-75]

Possibly two of the most well documented factors affecting NOM binding of trace metals are solution pH and ionic strength.[57, 65, 76-77] Modelling studies such as those carried out by Shi *et al.* (2016) have predicted a strong pH dependence on metal binding by NOM. Experimental laboratory-based studies have also demonstrated this for divalent metal complexes with humic and fulvic acids, with results showing slower dissociation of Cu-HA and Ni-FA complexes at elevated pH.[78-79] Experimental studies on cave dripwater samples have also shown this phenomenon, for instance Hartland *et al.* (2011) found enhanced NOM binding of transition metals in hyperalkaline cave dripwaters (pH ≈ 11) from Poole's cavern (Derbyshire ,UK) when compared to cave dripwaters of more typical pH (pH ≈ 8).[36] This is thought to be a result of the differences in availability of binding sites with changing pH. Electrolyte concentration has also been shown to affect divalent metal complexation by NOM, with studies showing increased dissociation rates in higher ionic strength solutions.[77, 80] This has been demonstrated experimentally for both Cu-HA and Ni-FA complexes.[77-78] Due to the significant effect of these solution characteristics on the stability and dissociation rate of transition metal-NOM complexes, pH and ionic strength have been carefully considered during this experimental study.

Another significant factor affecting complex stability and dissociation rates in natural systems is the metal to ligand ratio. Again the importance of this is due to changes in the availability of different NOM binding sites (i.e. weak vs strong binding sites).[77, 81] This effect has been observed for Cu-HA and Ni-FA complexes in several laboratory-based studies, with decreases in metal:ligand ratios causing slower dissociation rates and increased complex stability as more polydentate (and therefore more stable) complexes form. [65 77, 80] This is of course accompanied by a decrease in the fraction of free metal ions and labile metal-NOM complexes in the system.

Studies have been undertaken in order to provide quantitative estimates of dissociation rate constants for various metal-NOM complexes. For instance Amery *et al.* (2010) used the CLEM and Diffusive Gradient in Thin films (DGT) techniques to measure the dissociation kinetics of different Cu-DOM complexes in natural water samples.[62] They found that the dissociation of both Cu-NTA and Cu-citrate complexes was fast and followed first order dissociation kinetics, while the

dissociation of Cu-DOM complexes demonstrated slower, more complex dissociation kinetics with an average k_{diss} value of approximately 10^{-3} s^{-1}. Amery *et al.* also observed that dissociation of Cu-HA complexes in synthetic solutions was slower than for Cu-DOM complexes, highlighting the fact that the increased heterogeneity of NOM over isolated HA causes differences in the thermodynamic and kinetic properties of the resultant complexes. Thus although isolated acids can provide useful approximations of trace metal-NOM complex stability, the presence of molecules such as small organic acids, amino acids, and carbohydrates in natural NOM sources will likely cause faster dissociation kinetics than is seen for Cu-HA complexes.[62, 82]

A similar study carried out by Zhang *et al.* (2012) used DGTs to assess the dissociation kinetics of Ni-NTA, Ni-HA and Ni-FA complexes. They used a dynamic numerical model of the complexes in a DGT system in order to estimate the k_{diss} values that were in agreement with their experimental data. The k_{diss} values obtained were $2 \pm 0.5 \times 10^{-4}$ s^{-1} for Ni-NTA, 2.5×10^{-3} s^{-1} for Ni-FA and 3.42×10^{-4} s^{-1} for Ni-HA, supporting the observation of Amery *et al.* (2010) that divalent metal complexes with NTA dissociate more rapidly than those with DOM. These values will provide useful estimates of the dissociation rates of some of the complexes used in this study, although they unlikely to be exactly the same due to small differences in solution composition (e.g. ionic strength and pH).

There have also been several studies undertaken in the last decade investigating the complexation of first-row transition metals with NOM in cave systems that have been invaluable in the quest to establish these metals as paleoproxies.[12, 14, 36, 40, 61] Hartland *et al.* (2011) investigated the speciation, size distribution and metal complexation properties of NOM in the dripwaters of a hyperalkaline cave, Poole's Cavern (Derbyshire, UK).[36] They demonstrated the presence of soil-derived colloids in the dripwaters and they found that colloidal NOM was a dominant complexant of Co, Ni, Cu and V in this karst system, with particularly stable complexes formed by Co. This study marked a shift in the thinking surrounding partitioning of trace metals into speleothem carbonates, as previous studies had frequently interpreted their partitioning under the assumption that they were present as free ions. This study demonstrated that the complexation of these metals with NOM is likely to have significant effects on their partitioning and therefore must be taken into account.[36]

A further study of metal binding and transport by natural organic matter (NOM) in karst dripwaters was undertaken in order to confirm this phenomenon in contrasting cave sites and to characterise the metal-ligand interactions.[12] Hartland *et al.* (2012) measured the concentrations of both organic carbon and trace metals in filtered soil leachates and dripwaters from three contrasting cave systems: Lower Balls Green Mine (Gloucestershire, UK), Grotta di Ernesto (Trentino, Italy) and the previously studied cave, Poole's Cavern (Derbyshire, UK).[12] They demonstrated that the transport of first-row transition metals through the karst system was significantly mediated by NOM, particularly colloidal OM.[12] They also observed distinct linear trends between Cu:Ni ratios and the acid-soluble NOM and poorly-soluble NOM end members in the soil leachates and cave dripwaters. The observed variations in Cu:Ni ratios in the dripwaters were attributed to differences in the functional groups of each end member and the affinity of the different metals for these binding sites. They also observed increased concentrations of mobilised particulate and colloidal OM during periods of increased dripwater supply (when fracture flow dominated) that corresponded with increased concentrations of Cu, Ni, Fe, Sn and Mn. During periods of decreased dripwater supply, a decrease in transition metal and NOM concentrations were seen, and the NOM observed was substantially finer and primarily dissolved. The differences in Cu:Ni ratios between periods of high and low water supply were thus attributed to the increased presence of stronger binding sites in coarser OM compared to smaller humic-like colloids, and the competitive binding of Cu over Ni for these sites (in accordance with the Irvin-Williams series).[12, 57] Based on this study, it has been suggested by Blyth *et al.* (2016) that the ratio of different first-row transition metals in speleothem samples could likely prove useful for providing insights into the composition of dripwaters with respect to NOM. [12-13]

Further work was carried out in this area by Hartland *et al.* (2014) on samples from Poole's cavern with the aim of quantifying the trace metals and NOM captured in speleothem carbonate.[40] They observed variations in trace element content in the carbonate and based on their results attributed much of this variation to colloidal transport of the elements. They found the lability of metal-NOM complexes to be a significant factor in determining the trace element content observed in the speleothems samples, as the empirical partition coefficients ($K_{d\,app}$) they found were dependent on the 'free' aqueous fraction of metal, f_m, (i.e. the fraction of metal not

bound to NOM).[40] For instance, where the fraction of free metal was close to zero, $K_{d\ app}$ was also close to zero despite the actual inorganic K_d values ($K_{d\ act}$) for that metal being significantly higher. They proposed $K_{d\ app}$ and $K_{d\ act}$ values of the transition metals can be largely explained by the concentration of 'free' metal in the dripwaters, according to **Equation 1.16**, and thus, that differences in the preservation of each trace metal in calcite could be explained quantitatively by their complexation behaviour with NOM.*

$$f_{m(aq)} = \frac{\frac{M_{(s)}}{Ca_{(s)}}Ca(aq)}{K_d}M_{(aq)} \qquad \textbf{(1.16)}$$

Another important area that this study by Hartland *et al.* (2014) investigated was ternary complexation.[40] Briefly, ternary complexation occurs in speleothems when the metal-NOM complex adsorbs to the growing calcite surface and is incorporated into the speleothem as a whole. Thus, dissociation of the complex does not have to occur before the metal ion partitions into the calcite, and **Equation 1.16** does not hold (as $K_{d\ app}$ is no longer dependent on the 'free' metal concentration).[40] This study found that almost all of the Co present in the speleothem calcite was a result of ternary complexation of Co-NOM complexes (the most stable complexes in their cave system), but found that for complexes of Ni, Cu and V, the fraction of ternary complexation occurring was very small or absent. The authors thus concluded that although ternary complexation can occur for particularly stable complexes, it is the exception rather than the rule, and for most metals dissociation of the complex must occur before the metal can partition into calcite.[40] Thus, it was suggested that if further data on inorganic $K_{d\ act}$ values and complexation reactions between NOM and metals are obtained from karst-analogue laboratory studies, it will likely become possible to interpret the trace metal composition of speleothems in terms of their organic contents and thus provide a record of NOM character and concentration through time.[40]

* It should be noted that this relationship was derived in a hyperalkaline cave system, and thus the authors suggested that further testing should carried out in caves of a more 'typical' pH (pH 7-8) and also under controlled karst-analogue conditions in a laboratory.

A further study published in 2018 by Hartland and Zitoun investigated the speciation of Cu in cave dripwaters from five different sites in Aotearoa (New Zealand), and confirmed that Cu complexation by NOM is almost certainly a universal property of cave waters.[61] Using adsorptive cathodic stripping voltammetry on the water samples they were also able to determine that the presence of NOM reduced the concentration of 'available' Cu (defined as Cu that is either held in simple, readily dissociating inorganic complexes or hydrated 'free' Cu^{2+} ions, [Cu']) in solution by five orders of magnitude when compared to the total Cu concentration ($[Cu_T]$). They showed that even when $[Cu_T]$ increased, [Cu'] stayed consistently low, indicating that complexation with NOM was inhibiting the partitioning of Cu into the Ca^{2+} lattice position of calcite.[61] Based on their finding they developed a conceptual model (**Figure 1.8**), demonstrating the factors affecting the amount of Cu incorporated into the speleothem calcite, namely:[61]

- The residence time of speleothem thin water films
- The dissociation rates of labile metal-organic complexes
- The stability of ternary metal-NOM complexes

1.5.5 Effects of Organic Ligand Complexation on the Isotopic Fractionation of Metals

As mentioned in **Section 1.4.5**, the complexation of metals by organic ligands can cause their isotopic fractionation. It would be expected, therefore, that first-row transition metals such as Ni and Cu that have more than one stable isotope and that form comparatively stable complexes with NOM would likely be significantly fractionated in karst systems due to the widespread prevalence of metal-NOM complexes. The Jahn-Teller distortion experienced by Cu^{2+} complexes is likely to cause increased isotope fractionation of Cu in particular.[52] These isotopic signature in speleothems, therefore, could prove to be useful proxies that provide insight into the quality and quantity of NOM in karst systems.[13, 61, 64, 67-68, 83] This section will therefore briefly review a few of the relevant studies that have investigated the isotopic fractionation of trace metals caused by complexation to organic ligands.

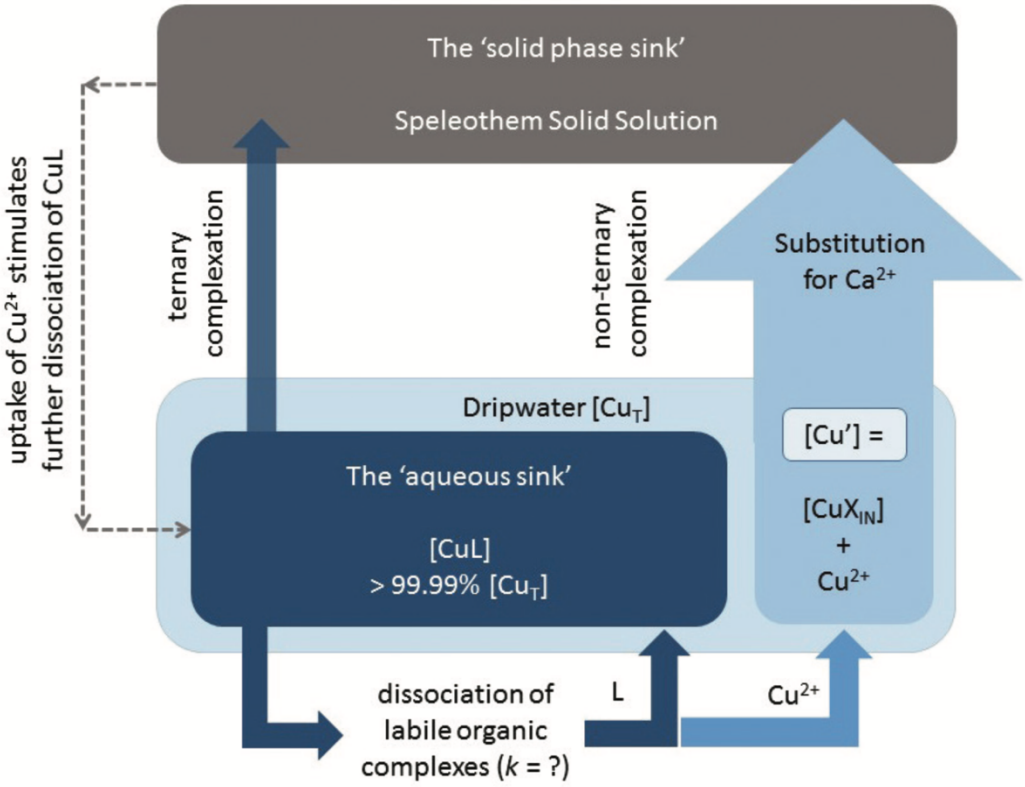

Figure 1.8. The conceptual model developed by Hartland and Zitoun (2018) outlining the processes occurring at the calcite-water interface for Cu-NOM complexes (represented here by CuL). Rapid complexation of the metal creates an 'aqueous sink' for Cu, while the adsorption of newly dissociated Cu^{2+} to the calcite surface creates a 'solid sink' and causes further dissociation of Cu-NOM complexes.[61]

In a karst-analogue laboratory experiment, Mavromatis *et al.* (2016) investigated the effects of organic ligands on the isotopic fractionation of magnesium during low-temperature precipitation of calcite.[84] Of the six ligands investigated, they found that only citric acid caused a significant change in the magnesium isotopic fractionation factor. They therefore concluded that the presence of organic ligands in cave dripwaters should not significantly affect magnesium isotope fractionation, which is not particularly surprising given that Mg does not complex strongly to organic ligands (see **Table 1.1** for a comparison of stability constants for Mg and transition metal complexes).

Of more relevance to this project are the several studies which have investigated whether organo-complexation of Cu can cause fractionation of stable Cu isotopes.[64, 67-68, 83] Bigalke *et. al* (2010) used Non-ideal Competitive Adsorption (NICA)-Donnan chemical speciation modelling to describe the binding of Cu to insoluble

humic acid.[67] They used this model to assess the isotopic fractionation of Cu when bound to a range of functional groups and found that the fractionation at equilibrium between 'free' Cu and the Cu bound to insoluble humic acid was 0.26 ± 0.11 ‰. They also found the modelled isotopic fractionation of Cu was the same for high affinity and low affinity sites within the humic acid, and that the degree of fractionation was independent of pH.[67] Ryan *et. al* (2014) also investigated the degree of isotopic fractionation of Cu during complexation with various soluble ligands, using a Donnan dialysis technique.[68] The ligands used were EDTA, NTA, iminodiacetic acid (IDA), desferrioxamine B (DFOB) and Suwannee River fulvic acid (SRFA). They found an enrichment of ^{65}Cu in the complexes compared to the 'free' Cu species, with $\Delta^{65}Cu_{complex\text{-}free}$ values ranging from +0.14 to + 0.84 ‰. They also observed a strong linear correlation between the logarithms of the stability constants of the Cu complexes and the magnitude of isotopic fractionation.[68] Fujii *et. al* (2013) observed that the presence of only a few ppm of an oxalate ligand changed the isotopic fractionation of Cu between calcite and the aqueous solution by 1‰ i.e. the calcite was enriched in light Cu.[85] The results of these studies indicate that, as expected, the stable isotope fractionation of Cu in particular is likely a good candidate for use as a speleothem-based paleo-proxy.

1.6 Laboratory 'Cave-Analogue' Experiments

It has already been demonstrated in the sections above that laboratory-based experiments can be useful tools to help provide important information on trace element partitioning and organo-complexation. Laboratory-based cave-analogue experiments can be particularly useful as they allow experiments to closely model the unique cave environment and the modes of natural speleothem precipitation, thus providing more meaningful and relevant results. This section will briefly review some of these cave-analogue experiments to highlight the types of experiments that can be done and the value of the results they can produce.

There have been several laboratory-based studies dealing with trace element incorporation into calcite that have aimed to establish partition coefficients for various trace elements. Huang and Fairchild (2001) for instance carried out a series of experiments using a cave-analogue experimental design.[86] They precipitated

$CaCO_3$ in an environment with controlled temperature and near 100% relative humidity. In their experiments, they mixed $NaHCO_3$ and $CaCl_2$ solutions at a pCO_2 of 631 ppmV and transported the solution through a tube to a drip site where it dripped onto a glass plate. They determined partition coefficients for Mg and Sr at different $CaCO_3$ growth rates, and from their results suggested that Mg partition coefficients may allow the determination of $Mg/Ca_{(aq)}$ in some caves. They suggested that the partition coefficient values for Sr, in contrast, should be interpreted with caution due to the growth-rate dependence of $K_{d\text{-}Sr}$ that they observed.[86]

Day and Henderson (2013) studied the partitioning behaviour of Li, Na, Mg, Co, Sr, Cd, Ba and U into calcite at various temperatures (7, 15, 25 and 35 °C) and drip rates (2, 6 and 10 drips per minute), using an experimental design that mimicked natural processes even more closely.[51] They precipitated calcite via CO_2-degassing from a thin solution film of low ionic strength and maintained tight control on temperature, pCO_2, drip rate and calcite saturation index (SI) throughout their experiments. **Figure 1.9** shows the experimental design they utilised. From their data they were able to develop temperature dependent expressions for the partition coefficients of these trace elements.[51] They also determined that high $X/Ca_{(calcite)}$ values, when X was a compatible element like Cd, were particularly indicative of low amounts of PCP and they suggested $Cd/Ca_{(stalagmite)}$ would be a useful addition to trace-element studies of natural stalagmites. These studies demonstrate the value of laboratory experiments in investigating controls on trace element partitioning into calcite, and to speleothem science and paleoclimate reconstructions overall.[51]

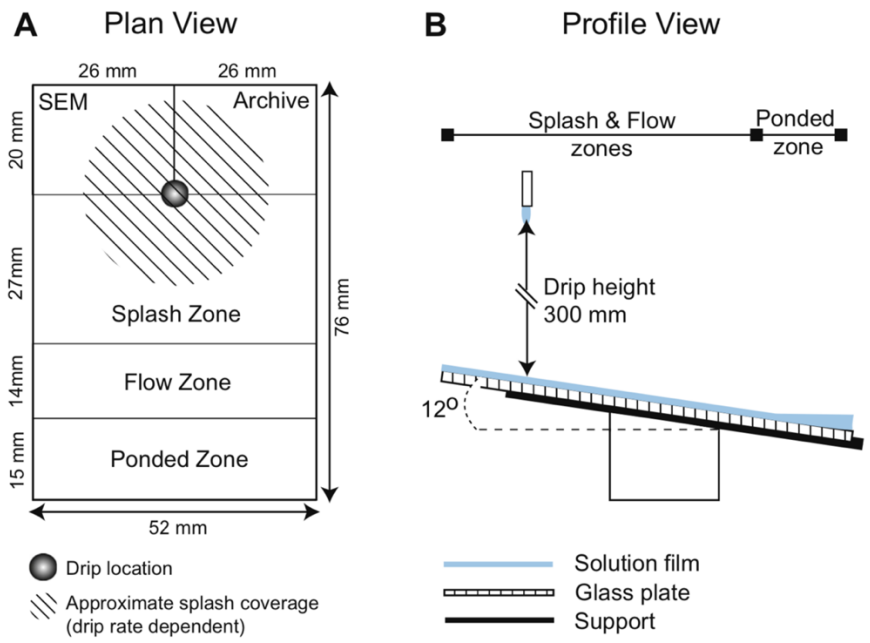

Figure 1.9. The experimental setup used by Day and Henderson (2013). A) A plan view of the glass plate on which the solution dripped. The glass plate was seeded with calcite prior to the experiment. The filled circle shows the location of the drip site. B) A profile view of the glass plate. Taken from reference [51].

The use of a completely sealed cave-analogue system with controlled temperature, pCO_2, humidity and solution composition has been reported in the literature by Hansen *et al.* (2017) and represents a major improvement in calcite-growth laboratory experiments.[19] By conducting experiments within a sealed environment, they were able to study in detail the carbon isotope exchange between gaseous CO_2 and dissolved inorganic carbon (DIC) in a thin solution film composed of water and dissolved calcium carbonate. A schematic of their experimental design is provided in **Figure 1.10**. By utilising a sealed 'cave-like' environment, they were able to flush the system with $N_{2(g)}$ and then establish a defined pCO_2 level within the box (500-1000 pCO_2), using CO_2 of known isotopic composition. These experiments allowed the development of a novel, complete reaction diffusion model describing the carbon isotope exchange between gaseous CO_2 and DIC. This allowed a more in-depth understanding of the processes affecting the $\delta^{13}C$ proxy in speleothems, and again illustrates the value of laboratory-based experiments for speleothem science.[19]

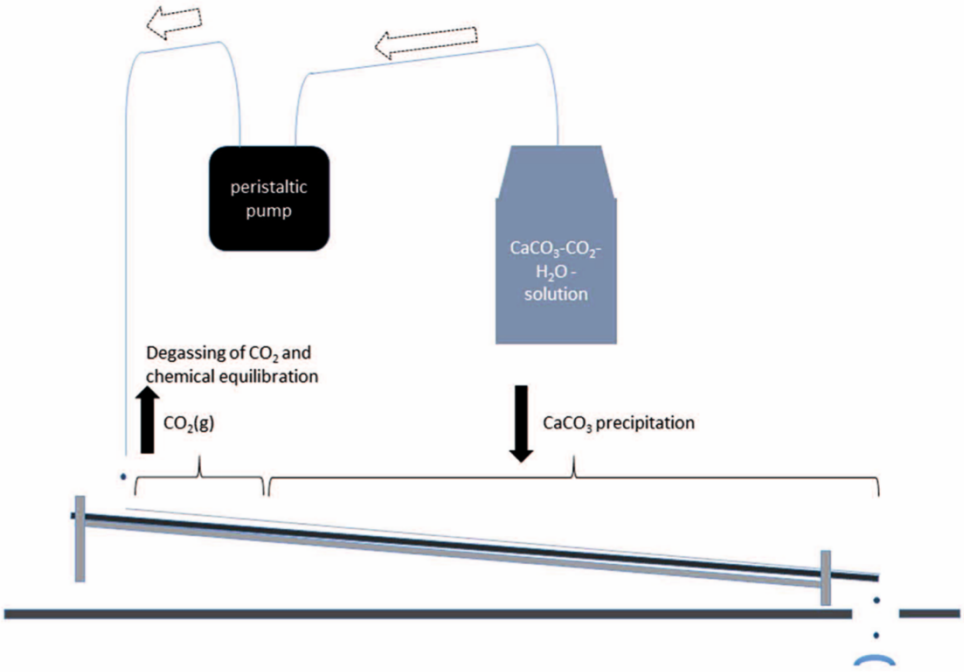

Figure 1.10. A schematic representation of the experimental design used by Hansen *et al.* (2017). They dripped the solution via a peristaltic pump on to a sandblasted glass plate, ensuring a thin solution film over the whole plate. Degassing of CO_2 and chemical equilibration occurred in the first section of the plate, followed by precipitation of calcite along the rest of the plate. Taken from reference [19].

As yet, no extensive laboratory-based study on the incorporation of divalent first-row transition metals into speleothem-like calcite has been undertaken. Thus, this project will aim to build on the knowledge obtained by previous cave-analogue studies by carrying out calcite-growth laboratory experiments with solutions containing Co^{2+}, Ni^{2+}, Cu^{2+} and organic ligands. A completely sealed cave-analogue system similar to that used by Hansen *et al.* (2017) will be used in order to ensure precise control on environmental variables and to ensure the conditions during calcite growth are as similar to karst cave conditions as possible.

1.7 Aim and Objectives

Although a significant amount of research into the use of speleothems as paleoclimate records has been undertaken, there are a vast number of processes affecting each type of paleoclimate signal that have made the unambiguous interpretation of speleothem records problematic thus far.[7] Quantitative

reconstruction of past rainfall is currently not possible as there are many convoluting factors affecting stable isotope and trace element signals. Therefore, more research into the effects of these factors, and investigation into other potential proxies is required. Few studies have investigated the incorporation of transition metals into speleothem calcite compared to the widely used alkali earth metals, however, there is evidence that they may be useful additions to the speleothem proxies already used. The aim of this project is to investigate the suitability of Co, Ni and Cu as paleoclimate proxies in speleothems by studying their partitioning behaviour into calcite and their interaction with organic ligands during calcite precipitation. In order to do this, four broad objectives have been identified within the project.

- Firstly, a suitable method that allows calcite growth under cave-analogue conditions in a laboratory, and that allows the effects of PCP on trace element incorporation into calcite to be assessed, will need to be established.

- Secondly, inorganic partitioning values for the three metals will be calculated.

- Thirdly, the effects of two organic ligands on Co, Ni and Cu incorporation into calcite will be assessed, and their new apparent K_d values calculated. This will help to provide a greater understanding of the impact NOM in cave dripwaters may have on these potential proxies.

- Finally, samples will be taken so that the isotopic fractionation of Cu that occurs as is it incorporated into calcite in the presence of these ligands can be measured. Unfortunately, due to instrumental and time constraints, these isotope measurements will not occur during the timeframe of this thesis but will be carried out subsequently.

These objectives will help to establish whether Cu, Ni and Co are viable paleoclimate proxies in speleothems that may be used in a multi-proxy approach for paleoclimate reconstructions. This in turn may help speleothem scientists worldwide to interpret their records with a higher degree of certainty and provide

information on past climatic events that could help us to better understand our current and changing climate.

2 Methods and Materials

2.1 Materials

2.1.1 General Chemicals

$CuCl_2 \cdot 2H_2O$, $CoCl_2 \cdot 6H_2O$, $NiCl_2 \cdot 6H_2O$, nitrilotriacetic acid (NTA) and lycopodium were supplied by British Drug House (BDH) Limited. $CaCO_3$ and $CaCl_2$ were supplied by Sigma Aldrich. Suwannee River Fulvic Acid (SRFA) was supplied by the International Humic Substances Society.

2.1.2 Gases

Industrial grade CO_2 (code 169) and N_2 (code 152) were used for all experiments (supplied by the British Oxygen Company).

2.1.3 Trace Element Standards

Both the multi-element ICPMS standard and the single element calcium standard were supplied by inorganic ventures.

2.2 Design of Crystal Growth Experiments

In order to enable calcite growth experiments that were analogous to calcite growth in a natural cave system, the first part of this project was dedicated to experimental design. A system that allowed careful control of environmental variables was established, and a method that caused crystal growth via CO_2 degassing was developed to ensure the experiments closely resembled natural speleothem precipitation, thus providing more meaningful and relevant results than they otherwise would have.

2.2.1 GeoMIC: Control of Environmental Variables

A climate-controlled environment in which the experiments could take place (**Figure 2.1**) was purpose-built over the course of this project, based closely on the system used by Hansen *et. al* (2017).[19] This system, christened GeoMIC (Geochemistry, Minerals, Isotopes and Climate) is a state-of-the-art climate-control box designed to provide researchers with a chamber of well-defined atmosphere and precisely controlled temperature, humidity and CO_2 concentrations. GeoMIC was equipped with a four-channel high-precision Hei-FLOW Heidolf peristaltic pump to provide precise control of drip rate, a Vaisala HMP7 relative humidity and temperature probe and a Vaisala GMP252 CARBOCAP carbon dioxide probe. Three NTC thermistors were also installed in GeoMIC to monitor temperature; one at each end of the box and one that was deployed into the solution reservoir (see **Section 2.2.2**).

The temperature inside GeoMIC was controlled via a Polyscience recirculating chiller coupled to a radiator fan inside the enclosure. Removable insulating panels were installed on the outside of the box during the majority of the experiments to help maintain temperature. Atmospheric pCO_2 was controlled via the addition of N_2 and CO_2 gases through computer-controlled magnetic valves as required. A purpose-built Labview software program installed on GeoMIC's computer allowed automatic control of the Polyscience recirculating chiller and the magnetic valves to control temperature and pCO_2 within the chamber via feedback from the Visala probes. Humidity was kept as high as possible throughout the experiments, with the incoming CO_2 and N_2 gas passing through hydration flasks before entering the chamber. An aquarium membrane pump was used to cycle the air inside GeoMIC through a beaker of water for the duration of the experiments to increase humidity further. The labview software logged all atmospheric data for the duration of the experiment at one minute intervals.

Manual manipulation of an experiment after the chamber had been sealed to the outside environment was achieved through four nitrile isolator-box gloves installed on the face of the box. A sample port at the end of the chamber allowed samples to

be removed during the experiment with minimal gas, temperature and humidity exchange occurring with the outside environment.

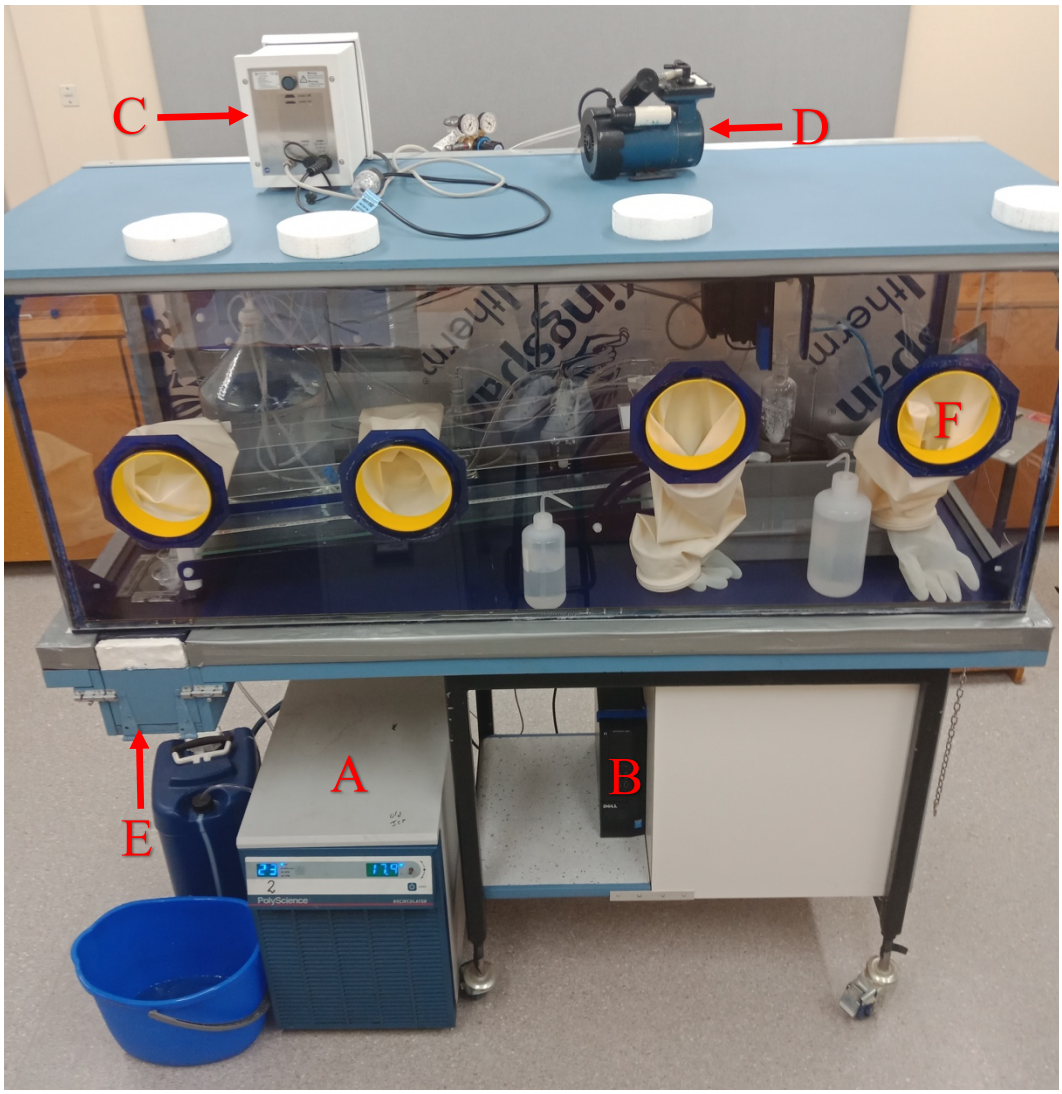

Figure 2.1. The cave-analogue system GeoMIC. A) The recirculator controlling temperature inside the chamber. B) Networked computer controlling the pump, gas valves, humidifiers and recirculator. C) High precision peristaltic pump. D) Humidifying pump to circulate chamber air through a beaker of water. E) The sampling port. When opened, solution samples can be taken from inside the chamber. F) Isolator-box gloves allow manual manipulation of the experiment.

The environmental conditions under which all experiments were performed are given below in **Table 2.1**. These conditions were chosen as they are similar to those found in a 'typical' cave environment with actively growing speleothems.[1]

Table 2.1. Environmental conditions for each crystal growth experiment. Errors represent one standard deviation. Values were measured at one minute intervals for the duration of each experiment.

Experiment	pCO_2 (ppm)	Temperature (°C)	Humidity (%)
1 (Inorganic 1)	1000 ± 6	20 ± 0.1	93 ± 3
2 (Inorganic 2)	1000 ± 11	20 ± 0.1	95 ± 1
3 (NTA Ligand)	1000 ± 7	20 ± 0.3	94 ± 2
4 (SRFA Ligand)	999 ± 6	20 ± 0.1	95 ± 1

2.2.2 Experimental Design

To replicate a reservoir of cave dripwater, $CaCO_3$ (5 g) was dissolved in 10 L of deionised water to make a solution of 5 mM $CaCO_3$ and trace elements and organic ligands were added as required for each experiment (see **Section 2.2.4**). While stirring, CO_2 gas was sparged through this solution until the reservoir became clear. The pH of the solution at this point was approximately 5 for all experiments, and the solution was undersaturated with respect to calcite (calculated in PHREEQC).[87] In typical cave systems, where the dripwater remains in the aquifer for sufficiently long periods to reach chemical equilibrium with the host rock, the SI of the dripwater in the aquifer is approximately 0.[88] Thus, the undersaturated experimental solution was sparged with N_2 gas until the solution became only slightly undersaturated with respect to calcite (SI ≈ -0.09, pH ≈ 6.4). The SI of the solution was determined by measuring its pH, as the relationship between pH and calcite SI of the solution had been modelled for each experiment using PHREEQC. The PHREEQC code used to do this is given in **Appendix I**. A SI index of exactly 0 was not used in order to avoid prior precipitation of calcite in the reservoir or tubing. Once prepared, the solution was immediately sealed to the environment, and was equilibrated to 20 °C in GeoMIC for 48 hours.

After the reservoir had reached temperature and the pCO_2, humidity and temperature in the GeoMIC chamber had stabilised, the solution was pumped via the Hei-FLOW peristaltic pump onto a 190 cm long glass plate with two 4 cm-wide 'channels' defined at the edges by adhesive tape (**Figure 2.2**). The glass plate was

sandblasted in order to supply sites for calcite nucleation and held at a 3° angle. A thin film of the solution was established in both channels, the characteristics of which will be described in detail in **Section 2.2.3**. During the first few cm (~4 cm for all experiments), degassing of the dissolved CO_2 occurred and the pH of the solution rose to *ca.* 8 and thus the solution became supersaturated with respect to calcite, as was seen by Hansen *et al.* (2013).[18] As the thin solution film flowed down the plate, $CaCO_3$ was progressively precipitated out on to the glass. At the end of the plate the solution dripped into the sampling port, where it drained to waste. This process of precipitation was allowed to occur uninterrupted for 72 hours. During this time, samples were taken from the reservoir for pH, conductance and ICP-MS measurements using the isolator-box gloves so that the solution composition could be monitored.

The use of two channels for these experiments were necessary in order for K_d values to be calculated for each trace element at different distances (i.e. after different amounts of prior calcite precipitation, PCP, had occurred). After 72 hours, flow to one of the channels (referred to as the reference channel) was ceased, so that the precipitated calcite in this channel could be sampled at different distances in order to determine trace element (and in some cases organic ligand) content. The other channel (referred to as the sampling channel) continued flowing and was used to collect water samples at different distances of flow so that the trace element and organic matter content of the 'dripwater' could be measured. The distance of flow was adjusted by shifting the drip site down the plate, and at each new distance the thin film was left to equilibrate for 30 min. Three samples were taken at each distance for the majority of the experiments; one for pH and conductance measurements, one for Cu isotope measurements, and one for ICP-MS measurements. An extra sample was taken at each distance for the organic experiments so that the organic ligand concentration could be measured.

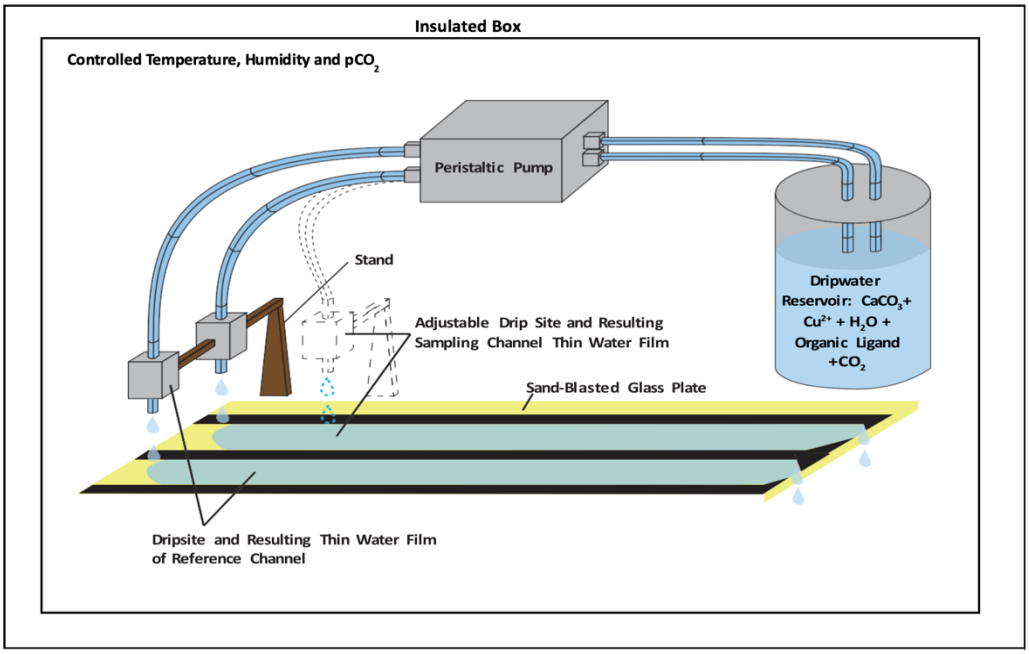

Figure 2.2. Schematic of the experimental design inside GeoMIC used for the crystal growth experiments. A 10 L solution supersaturated with respect to calcite (with trace elements and organic ligands added) was pumped via a peristaltic pump and dripped onto an inclined glass plate at discrete intervals and at a defined rate, the flow being routed along into two channels. The distance of flow in the sampling channel was adjustable to allow for K_d values to be calculated for each trace element at different distances (i.e. after different amounts of PCP had occurred)

2.2.3 Solution Thin Film Characteristics

It was discussed in **Section 1.2.4** that when **Equation 1.4** (the equation derived by Buhmann and Dreybrodt in 1985 to calculate the precipitation rate, F, of $CaCO_3$ from a thin film) is applied to water films as thin as those seen in caves (~ 0.1 mm), the rate constant κ becomes independent of the film thickness.[23, 27] Thus as calcite precipitates from such a film, calcite supersaturation decreases exponentially according to a characteristic decay time, τ_{pr}, and the change in concentration of Ca^{2+} and HCO_3^- with time can be described by **Equation 1.6**. The growth rate can then be calculated according to derivatised version of this equation (**Equation 1.7**). Therefore the film thickness of the solution in each channel of each experiment was calculated in order to ensure this equation could be used to calculate the $CaCO_3$ growth rate.[18] The thickness of the water film, δ, was measured using the method outlined by Hansen *et al.* (2013). This method requires that the average flow

velocity of the film and the flow rate of the film are measured prior to the experiment (**Equation 2.1**):[18]

$$\delta = \frac{Q}{B.V_{ave}} \quad (\mathbf{2.1})$$

where Q is the flow rate of the thin film (in $cm^2\ s^{-1}$), B is the width of the thin film (in cm) and V_{ave} is the average flow velocity of the film (in $cm\ s^{-1}$). V_{ave} was calculated for each experiment according to the method outlined by Hansen *et al*. (2013), whereby the maximum flow velocity (V_{max}) of the film is first measured, and the V_{ave} is calculated according to **Equation 2.2**:[18]

$$V_{ave} = \frac{2}{3}V_{max} \quad (\mathbf{2.2})$$

The maximum flow velocity of the thin film was determined for each experiment, again using the method described by Hansen *et al*. (2013).[18] Briefly, the time taken for a small volume of superhydrophobic lycopodium powder to travel 50 cm down the centre of the channel was measured and taken to be V_{max}.[18] The characteristics of the thin film for each experiment are outlined below in **Table 2.2**. All thin films were within the range 0.8-0.14 mm, and thus it was determined that the use of **Equation 1.7** to calculate growth rate was appropriate. Measurement of the flow velocity also allowed the residence time of the thin film on the plate to be calculated.[18]

Table 2.2. Characteristics of the thin solution films in both channels for the four experiments. Errors correspond to one standard deviation in V_{max} and Q measurements, and systematic errors associated with lab equipment are also accounted for.

Experiment	Channel	V_{max} (cm s^{-1})	V_{ave} (cm s^{-1})	Q (cm^3 s^{-1})	δ (mm)	Total Residence Time (s)
1 (Inorganic)	Sampling	0.44 ± 0.08	0.29 ± 0.05	0.0121*	0.10 ± 0.02	287 ± 49
	Reference	0.51 ± 0.05	0.34 ± 0.03	0.0112*	0.08 ± 0.01	250 ± 24
2 (Inorganic)	Sampling	0.49 ± 0.02	0.33 ± 0.02	0.0152 ± 0.0004	0.12 ± 0.01	258 ± 12
	Reference	0.53 ± 0.02	0.35 ± 0.01	0.0164 ± 0.0005	0.12 ± 0.01	241 ± 9
3 (NTA Ligand)†	Sampling	0.38 ± 0.02	0.25 ± 0.01	0.0144 ± 0.0006	0.14 ± 0.02	350 ± 20
	Reference	0.33 ± 0.01	0.22 ± 0.01	0.0129 ± 0.0008	0.14 ± 0.02	402 ± 13
4 (SRFA Ligand)	Sampling	0.53 ± 0.02	0.35 ± 0.01	0.0149 ± 0.0002	0.11 ± 0.01	241 ± 10
	Reference	0.56 ± 0.08	0.37 ± 0.06	0.0155 ± 0.0002	0.10 ± 0.02	228 ± 34

* Only one volume measurement was taken for each channel during experiment 1 so no measurement error could be calculated.

† The total distance travelled by the thin film was increased by 4 cm (89 cm in total) in this experiment, which accounts in part for the increased total residence time.

2.2.4 Solution Composition and Aqueous Speciation Modelling

In order for the results of these experiments to provide data relevant to the speleothem science community, the composition of the reservoir solution for each experiment was designed to be as similar as possible to both 'typical' cave dripwaters and previously published experimental solutions. Analytical capabilities (e.g. quantification limits of the ICP-MS methods used) were also taken into account.

The concentration of $CaCO_3$ used (5 mM) was higher than what is usually seen in a 'typical' cave environment;‡ this concentration was used in order to ensure precipitation of sufficient calcite during the experimental time frame, and was based on the concentration used by Hansen *et al.* (2017).[19] Due to the increase in [Ca^{2+}] compared to a 'natural' system, the concentration of trace elements were also increased so that the X/Ca ratios in the reservoir solution was similar to those observed in 'natural' samples. **Table 2.3** indicates X/Ca ratios used for each experiment alongside the same ratios seen in dripwater and stream samples taken

‡ For example, the average Ca concentration in 23 dripwater samples taken from an actively growing speleothem in Waipuna cave, Waitomo, Aotearoa (New Zealand) between 18/10/2016 and 3/1/2019 was 1.06 mM.

from Waipuna cave in Waitomo, Aotearoa (New Zealand). It can be seen from **Table 2.3** that the Co/Ca and Cu/Ca ratios were significantly higher in the experimental solutions than the same ratios seen in the dripwater and stream samples of Waipuna cave. These elevated solution ratios were required because the desire for 'natural' X/Ca ratios had to be balanced with the analytical capabilities of the ICP-MS method used. Specifically, the high Ca^{2+} concentration in the solution samples required them to be diluted before analysis. Therefore, to ensure trace element concentrations above the quantification limit of the instrument after dilution, trace element concentrations had to be increased. The high concentration of Cu^{2+} was also required in order to ensure that sufficient Cu was available in the precipitate for isotopic analysis via Multi-Collector ICP-MS (MC-ICP-MS).

Table 2.3. Trace element to Ca ratios (X/Ca) observed in dripwater and stream samples from Waipuna Cave, Waitomo, Aotearoa (New Zealand) and in the reservoir solutions prepared during this study.

	Waipuna Dripwater*	Waipuna Stream†	Reservoir Solutions (Experiments 1-3)	Reservoir Solution (Experiment 4)
Co/Ca (mM/M)	9.0×10^{-4}	9.9×10^{-4}	1.7	-
Ni/Ca (mM/M)	0.15	0.10	1.7	-
Cu/Ca (mM/M)	5.3×10^{-3}	7.1×10^{-3}	1.6	1.6

*Average of 23 samples taken from the dripwater of an actively growing speleothem between 18/10/2016 and 3/1/2019.

† Average of 18 samples taken from the stream inside Waipuna cave between 16/11/2016 and 3/1/2019.

The organic ligand concentrations that were used in experiments 3 and 4 were chosen to maximise complexation of Cu^{2+}, Ni^{2+} and Co^{2+}. The species distribution of the reservoir solutions for both the inorganic and organic experimental solutions was modelled using Visual MINTEQ, and will be discussed in **Chapter 4**.[87, 89] The concentration of NTA used in experiment 3 was also based on the molar ratio of NTA to Ni used by Zhang *et al.* (2013) during their kinetic studies of Ni organic complexes via diffusive gradients in thin films (DGT).[80] The initial composition of the reservoir solutions used in each experiment is given below in **Table 2.4**.

Table 2.4. Initial composition of the experimental reservoir solutions.

Experiment	[$CaCO_3$] (mM)	[Co] (ppb)	[Ni] (ppb)	[Cu] (ppb)	[NTA] (ppm)	[SRFA] (ppm)	Initial pH	Initial Conductance ($\mu S\ cm^{-1}$)
1 (Inorganic)	5	50	50	50	0	0	6.50	848
2 (Inorganic)	5	50	50	50	0	0	6.45	848
2 (NTA Ligand)	5	50	50	50	2	0	6.56	852
3 (SRFA Ligand)	5	0	0	50	0	20	6.66	850

2.3 Analytical Methods

2.3.1 Inductively Coupled Plasma Mass Spectrometry (ICP-MS)

Solution samples were acidified with double Teflon distilled HNO_3 (Savillex DST-1000 Acid Purification System; Eden Prairie, MN, USA) to 2% (v/v) prior to analysis. For precipitate samples, ~ 2 mg of solid were removed from the plate at each distance of flow and dissolved in HNO_3 (5%, 8 mL). Acid blanks of 2% doubly distilled HNO_3 (v/v) were included in each run.

Elemental analysis was performed using an Agilent 8900 Inductively Coupled Plasma Mass Spectrometer (ICP-MS) controlled by MassHunter Workstation Version 4.5. An SPS4 autosampler was used for sample introduction. A 0.05-0.1 mL min^{-1} micromist U-Series nebuliser was attached to a quartz cyclonic spray chamber followed by a quartz torch with a 2.0 mm injector. A nickel sampler and skimmer cone followed the plasma torch, and an omega lens was used to focus the ion beam. The ICP-MS instrument was optimized to maximum sensitivity before each run, to ensure oxides and doubly-charged ions were fewer than 2%.

Five-point calibration curves for Co, Ni and Cu were constructed using a multi-element standard with concentrations ranging between 0.1 and 500 ppb, while the five point calibration curve for Ca consisted of concentrations between 100 and 10,000 ppb. A single-element standard was used for the Ca calibration curves. Re-calibration was undertaken after every 100 samples, check-standards were analysed

after each 20-sample batch, and blank samples were also analysed after every 10-sample batch to reduce sample carry-over. Samples were analysed in triplicate to assess analytical error. Isotopes used for quantification were ^{43}Ca, ^{59}Co, ^{60}Ni and ^{65}Cu for all experiments except Experiment 4 (SRFA), where ^{44}Ca was used due to matrix interferences with ^{43}Ca.

2.3.2 Raman Spectroscopy

A Perkin Elmer Ramanstation 400-R spectrometer equipped with an air cooled Charge Coupled Device (CCD) detector and 785 nm near infrared laser was used to collect Raman spectra of $CaCO_3$ samples. Data points were collected every 1 cm^{-1} and the laser was focussed on a ~190 μm diameter spot on the samples. The day-to-day variation of the instrument was checked via comparison of the Raman spectrum of a high density polyethylene pellet (Sigma Aldrich) to previously obtained spectra, in order to ensure the instrument was functioning correctly. A Perking Elmer polystyrene standard disk supplied by Sigma Aldrich was used for calibration.

2.3.3 Fourier Transform Infra-Red (FTIR) Spectroscopy

The precipitate from between 20 and 25 cm on the sampling channel of each experiment were taken for structural characterisation. Sub-samples were mixed and homogenised with oven-dried (100°C) KBr at an approximate ratio of 1:50 in a mortar and pestle, before being compressed into discs under 10,000 kg of pressure. Spectra were collected on a Perkin-Elmer Spectrum 100 spectrometer at a resolution of 1 cm^{-1} with eight scans ranging between 600–1200 cm^{-1}, following the method developed by Ni and Ratner (2008). Background measurements of a blank KBr disc were taken and subtracted from the sample spectra using the software package Spectrum (version 6.3) default method.

2.3.4 Powder X-ray diffraction (pXRD) of crystals

$CaCO_3$ crystals precipitated during each experiment were characterised on a Panalytical Empyrean XRD. The XRD patterns were collected at a scanning rate of $0.02 \circ s^{-1}$ in 2θ with diffraction angles from 20 θ to 60 θ, and Cu Kα radiation energy of 40 kV and 20 mA was used, following the procedure outlined by Ni and Ratner (2008).[90]

2.3.5 Scanning Electron Microscopy (SEM)

Scanning electron microscopy was undertaken to characterise the microstructures of the crystals precipitated from each experiment, using an Hitachi S-4700 cold field emission microscope. Samples were sputter coated in an ultra-thin layer of platinum and palladium for sample conductivity. After coating, the $CaCO_3$ crystals were taped to aluminium stubs and observed in scanning mode using a voltage of 5 kV.

2.3.6 Fluorescence Analysis of Growth Solutions and Calcite Samples

In order to determine the extent of SRFA ligand incorporation into the $CaCO_3$ during the second organic ligand experiment, both solution and precipitate samples were measured for 3D excitation emission matrix (3D EEM) fluorescence using a Horiba Jobin Yvon Aqualog spectrometer with a CCD detector. A measurement range of 240-600 nm excitation and 245-800 nm emission was used, along with a 0.5 sec integration time and a 3 nm step-size.[91] Each matrix was corrected for inner-filter effects, scatter lines were Rayleigh masked (both first and second order), and spectra were normalised to the average Raman intensity of deionised water using Aqualog's data processing software.[92]

Prior to 3D EEM analysis, solution samples were acidified to 0.025 M HCl in order to ensure complete dissolution of organic matter and $CaCO_3$. Precipitate samples (2 mg) were dissolved in dilute HCl (0.025 M, 4 mL) following the method outlined by Pearson *et al*.[91] A five-point calibration curve for SRFA was constructed with

concentrations ranging between 1 and 20 ppb. Standards were acidified to 0.025 M HCl and matrixed matched to the solution samples via addition of $CaCl_2$ to the same ionic strength as that of the reservoir solution (I=0.02). Blank samples were analysed after every 10-sample batch.

The 3D EEM data were processed with MATLAB using parallel factor analysis (PARAFAC) as implemented in the N-way toolbox,[93] and the drEEM toolbox.[94] PARAFAC provides multi-way data analysis in which the underlying phenomena of fluorescence can be distinguished and separated into statistically valid components.[95-96] A one component PARAFAC model was used for all samples, as only one meaningful fluorescence component (humic-like) was produced, as expected. The fluorescence spectra of the SRFA solutions were dominated by the humic-like fluorescence peak 'A' (ex 250-260; em 380-480) (**Figure 2.3**).[97] This peak has been well documented in humic material from terrestrial environments including cave systems.[97-99] The calibration curve obtained demonstrating the correlation between PARAFAC C1 scores and SRFA concentration used to calculate [SRFA] in experiment 4 is presented in **Figure 2.4**.

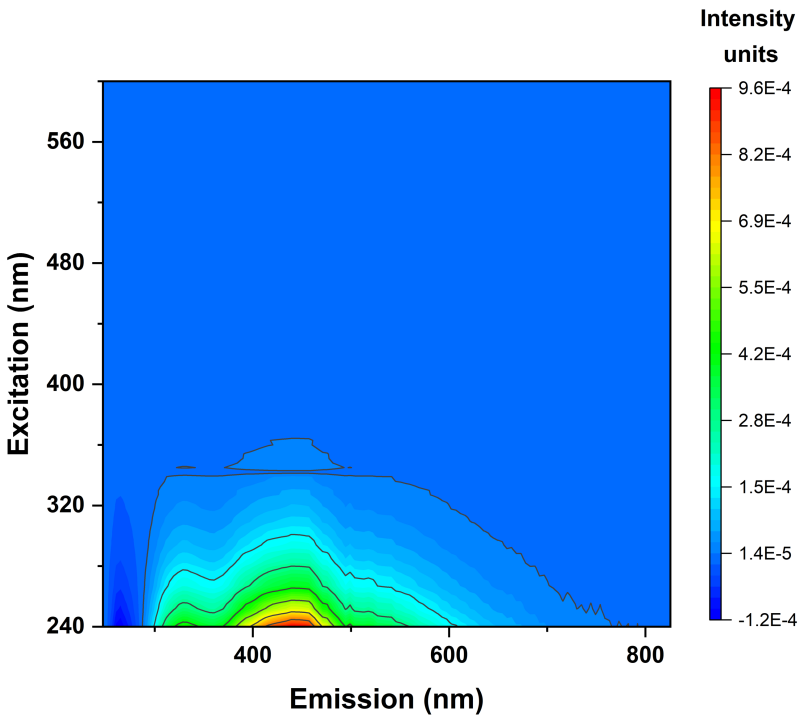

Figure 2.3. 3D-EEM of PARAFAC component 1 showing dominance of humic-like peak 'A'.

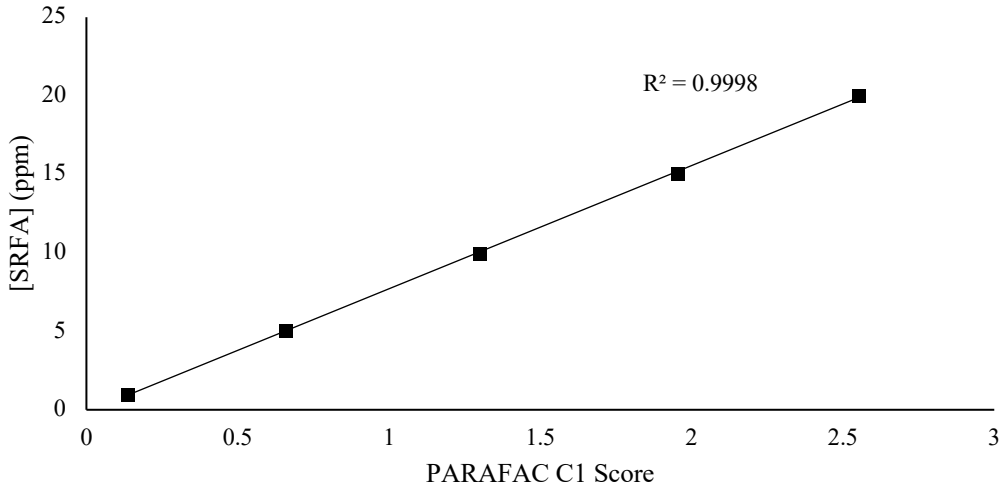

Figure 2.4. Correlation between PARAFAC C1 score and [SRFA]. The equation was applied to sample C1 scores to calculate [SRFA] in samples taken during experiment 4

3 Method Development and Preliminary Results

3.1 Introduction

In order to carry out calcite growth experiments allowing investigation into the partitioning behaviour of the first-row transition metals, and to provide results useful to the speleothem science community, a robust and relevant method needed to be developed. Therefore the first part of this project was designing and carrying out preliminary experiments to ensure the data obtained from the following experiments were valid. This chapter discusses the preliminary experiments carried out using the methods described in **Sections 2.2.1 - 2.2.3**, and the applicability of the results obtained from crystal growth experiments carried out via this method to 'real-world' speleothem and cave dripwater samples.

3.2 Methods

3.2.1 Experimental Design

The preliminary crystal growth experiment was primarily carried out according to the method described in **Section 2.2.2** above, with some minor differences. Briefly, a 10 L reservoir of 'dripwater' solution (5 mM $CaCO_3$) was sparged with CO_2 to dissolve the $CaCO_3$ (3 hr). The solution was then sparged with N_2 until the SI of calcite in solution reached -0.04. This corresponded with a solution pH of 6.48 (calculated using PHREEQC).[87] The solution was sealed and equilibrated to 20 °C inside the GeoMIC chamber (48 hr). Once equilibrated, the solution was pumped via a high precision peristaltic pump into two channels on an inclined, sandblasted glass plate (channel dimensions: 4 cm wide, 87 cm long, 2° incline). A thin film of solution was established in both channels and the solution was left to flow along

the channels for 3 days. On the fourth day, flow to the reference channel was terminated and the position of the dripsite on the sampling channel was decreased periodically. Two samples of dripwater were collected at the end of the plate for each distance of flow. An equilibration time of 30 min was allowed at each new distance before sample collection commenced. Control of environmental variables in the GeoMIC chamber was carried out automatically by the Labview software, with pCO_2 set to 1000 ppm, humidity to 100% and temperature to 20° C. Unfortunately due to issues with the GeoMIC software, logging of the environmental variables could not be undertaken during this preliminary experiment.

3.2.2 Thin Film Characteristics

The average flow velocity of the film and the flow rate of the film were measured prior to the experiment via the method described by Hansen *et al*. (2013), outlined in **Section 2.2.3**.[18] This allowed the thickness of the thin film to be calculated using **Equations 2.1** and **2.2**. The calculated values are given in **Table 3.1**.

Table 3.1. Characteristics of the thin solution films established in both channels during the preliminary crystal growth experiment.

	Sampling Channel	Reference Channel
Q (cm^3 s^{-1})	0.0071 ± 0.0004	0.0077 ± 0.0006
V_{max} (cm s^{-1})	0.30 ± 0.01	0.34 ± 0.03
V_{ave} (cm s^{-1})	0.20 ± 0.01	0.23 ± 0.02
δ (mm)	0.09 ± 0.01	0.09 ± 0.02
Total Residence Time (s)	431 ± 18	386 ± 34

During the experiment, small 'holes' without flowing solution were observed in the thin film. This was deemed to be a result of evaporation caused by a very thin film (0.09 mm) and thus the film thickness was increased slightly for all following experiments. Trials with various plate angles and flow rates were carried out to determine the optimum parameters for a film of thickness 0.1-0.12 mm, and both were increased accordingly for all further crystal growth experiments to ensure uniform precipitation across both channels.

3.2.3 Solution Composition and Aqueous Speciation Modelling

The composition of the reservoir solution used in the preliminary experiment is given below in **Table 3.2**. It should be noted that the trace element concentrations used here are lower than those used in the following four experiments. This was done in order to determine whether the trace element content in the precipitated carbonate would be sufficient for isotope analysis and ICP-MS measurements when X/Ca ratios were closer to those observed in typical cave dripwaters.

Table 3.2. Initial solution composition of the reservoir used in the preliminary experiment.

Selected Parameters of Solution	
[$CaCO_3$] (mM)	5
[Co] (ppb)	10
[Ni] (ppb)	10
[Cu] (ppb)	10
Initial pH	6.49
Initial Conductance ($\mu S\ cm^{-1}$)	858

The species distribution in the initial reservoir solution was modelled using visual MINTEQ 3.0 speciation codes. The modelling results are given in **Table 3.3**.

3.2.4 Analytical Methods

Details of the ICP-MS, Raman spectroscopy, FT-IR spectroscopy, SEM and pXRD methodologies used for sample analysis are outlined in **Section 2.3** above.

Table 3.3. The distribution of species modelled for the reservoir solution using the visual MINTEQ 3.0 speciation codes.

Component	Species	Proportion of Total Concentration (%)
Cu^{2+}	Cu^{2+}	19
	$CuOH^{+}$	0.97
	$CuCO_{3\ (aq)}$	74
	$CuHCO^{3+}$	6.4
	$Cu(CO_3)_2^{2-}$	0.35
Ni^{2+}	Ni^{2+}	59
	$NiOH^{+}$	0.011
	$NiCO_{3\ (aq)}$	1.5
	$NiHCO_3^{+}$	39
Co^{2+}	Co^{2+}	70
	$CoOH^{+}$	0.029
	$CoCO_{3\ (aq)}$	0.89
	$CoHCO_3^{+}$	29
Ca^{2+}	Ca^{2+}	93
	$CaHCO_3^{+}$	6.6
	$CaCO_{3\ (aq)}$	0.095
CO_3^{2-}	CO_3^{2-}	0.010
	$CaHCO_3^{+}$	1.9
	$CaCO_{3\ (aq)}$	0.028
	HCO_3^{-}	57
	$H_2CO_3^{*}{}_{(aq)}$	41

3.3 Results and Discussion

3.3.1 Evolution of Solution Carbonate Chemistry

The first solution samples to be taken at each distance of flow from the sampling channel were used to determine pH and conductivity. This allowed for the temporal evolution of the carbonate chemistry of the thin film to be monitored, and for the precipitation rate of the $CaCO_3$ to be calculated (see **Section 3.3.3**).

The pH of the solution increased from 6.49 (in the reservoir) to 7.08 at a flow distance of 0 cm, indicating degassing of dissolved CO_2 occurred almost instantaneously from the solution, as expected. The pH increased steadily with

increasing distance of flow to a pH of 8.07 after 87 cm. This indicated further evolution of CO_2 from solution occurred, likely a result of precipitating $CaCO_3$ (see **Equation 1.3**).

Further evidence for the precipitation of $CaCO_3$ as a result of degassing was the decrease in conductance seen as residence time increased. **Figure 3.1** shows the change in conductance with distance of flow. The exponential decrease in conductance was consistent with that observed by Hansen *et al.* (2013) and Hansen *et al.* (2017).[18-19]

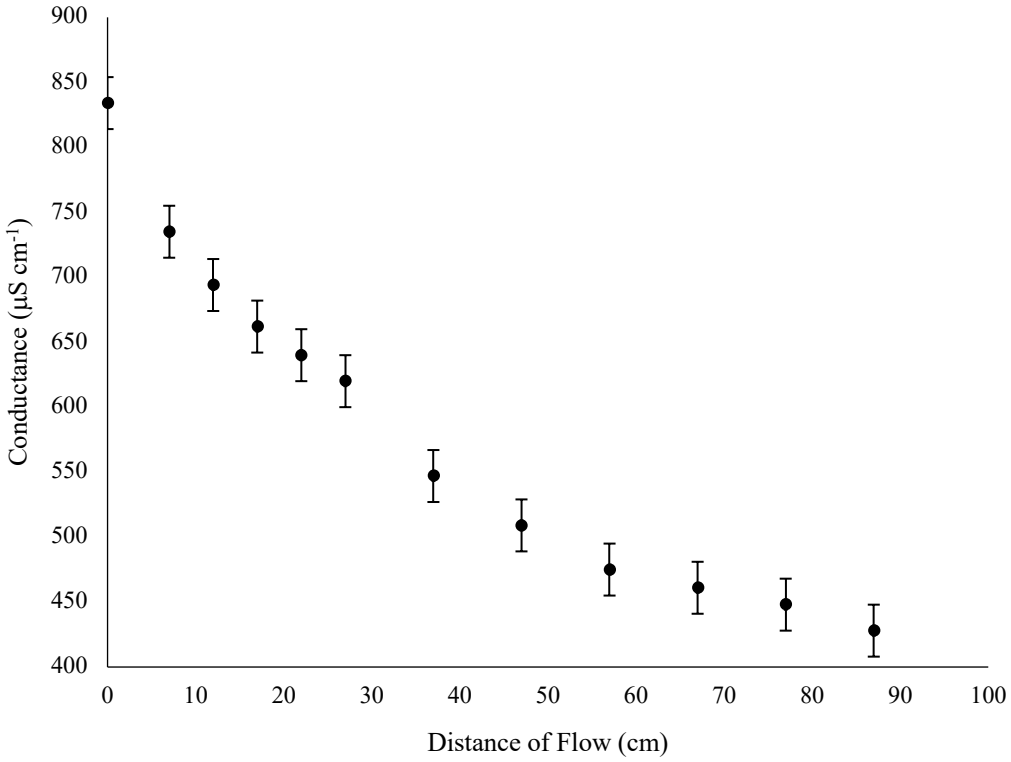

Figure 3.1. An exponential decrease in conductance was seen with increasing residence times during the preliminary experiment, consistent with the literature.

At the conclusion of the experiment, a thin layer of white crystalline material was observed in both channels on the glass plate. The precipitate was fairly uniform across the channels, however small patches of morphologically distinct precipitate were also observed, particularly in the last 10 cm of the plate. Structural characterisation of both precipitates was thus carried out in order to ensure that

calcite was the primary precipitate, and thus that the results of subsequent experiments were relevant to speleothem calcite.

3.3.2 Structural Characterisation of $CaCO_3$

The experimental method developed here required that the dominant $CaCO_3$ polymorph precipitated was calcite, as calcite is the most stable polymorph of $CaCO_3$ and thus also the most dominant in speleothem carbonates.[1] Samples of precipitate from the reference channel were therefore analysed using FT-IR spectroscopy, Raman spectroscopy, pXRD and SEM to characterise the morphology of the $CaCO_3$ crystals.

pXRD was initially carried out on the dominant precipitate, however there was insufficient sample to analyse the minor (morphologically distinct) precipitate using this method. **Figure 3.2** shows the pXRD pattern obtained for the precipitate, which was consistent with patterns observed for calcite standards in the literature (e.g. Ni and Ratner, 2008).[90] Peaks indicative of other $CaCO_3$ polymorphs, aragonite and vaterite, were absent from the pattern.[90]

FT-IR spectroscopy was also carried out on the dominant precipitate. In order to ensure the polymorph remained consistent along the flow path, samples from three different distances along the plate were taken for analysis. **Figure 3.3** shows the IR spectra obtained for precipitate samples from 14, 40 and 70 cm. All three spectra displayed the characteristic v_4 band of calcite at 713 cm^{-1} and v_2 band of calcite at 874 cm^{-1}, and were consistent with the calcite spectra reported by Ni and Ratner (2008). Bands characteristic of aragonite and vaterite were notably absent.[90]

Neither pXRD nor FT-IR spectroscopy could be carried out on the minor polymorph due to the sample size requirement of both methods. Thus, Raman spectroscopy and SEM were also carried out on precipitate samples. **Figures 3.4**

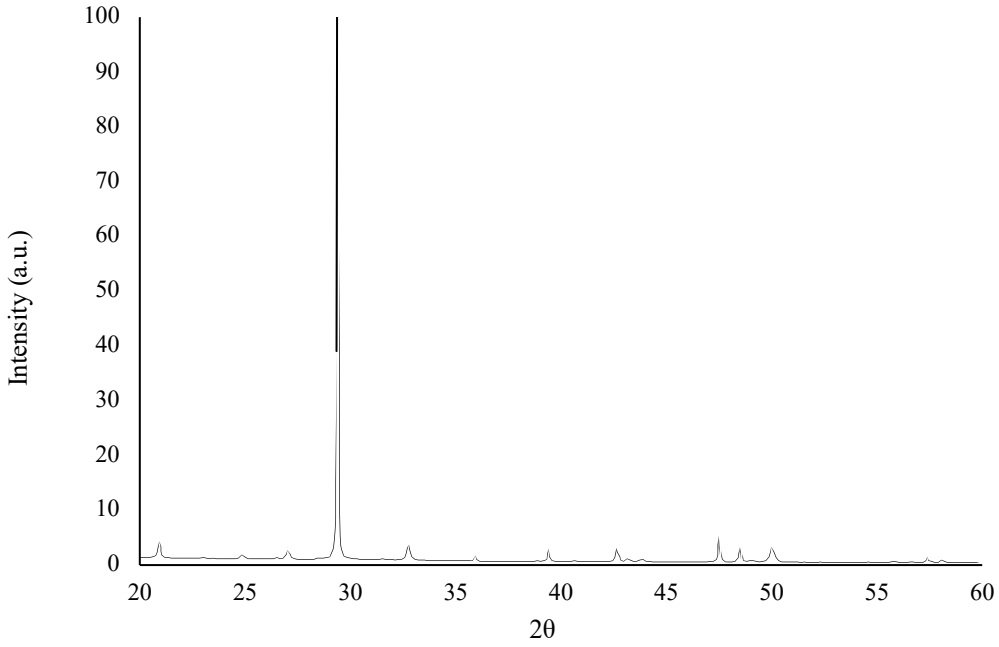

Figure 3.2. pXRD pattern observed for the dominant precipitate produced during the preliminary experiment.

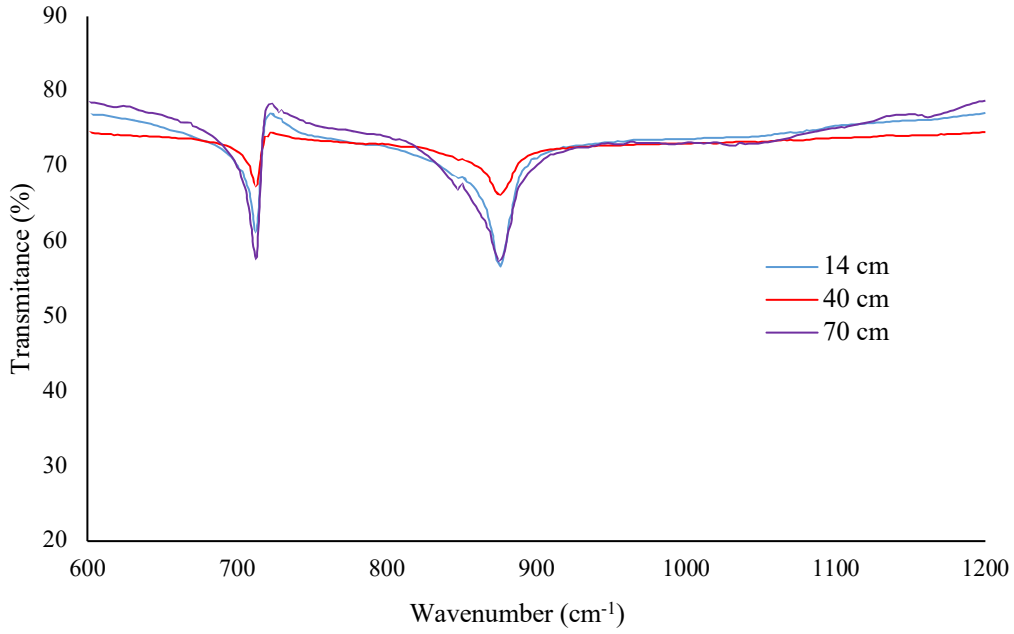

Figure 3.3. FT-IR spectrum of the dominant precipitate produced during the preliminary crystal growth experiment at three different distances of flow.

and **3.5** show the Raman spectra of the dominant and minor $CaCO_3$ polymorph, respectively. The spectrum of the dominant polymorph displayed the characteristic v_4 band of calcite at 711 cm^{-1} and v_1 band of calcite at 1085 cm^{-1}, and were consistent with calcite spectra reported in the literature.[100-101] The spectrum of the minor polymorph however displayed the characteristic v_4 band of the polymorph vaterite at 740-750 cm^{-1} and v_1 band of vaterite at 1074-1090 cm^{-1}, and was consistent with Raman spectra of vaterite reported in the literature.[101-102]

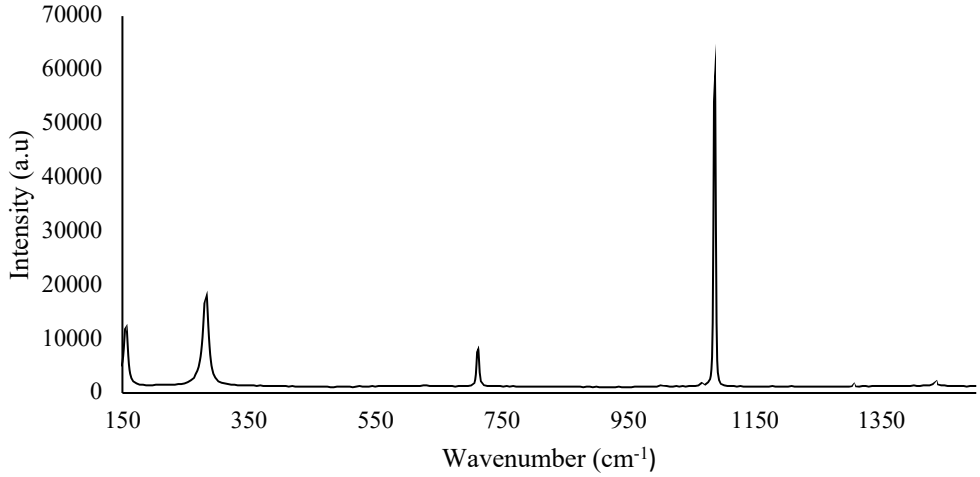

Figure 3.4. Raman spectrum of the dominant precipitate produced during the preliminary experiment, consistent with spectra reported in the literature for the calcite polymorph.

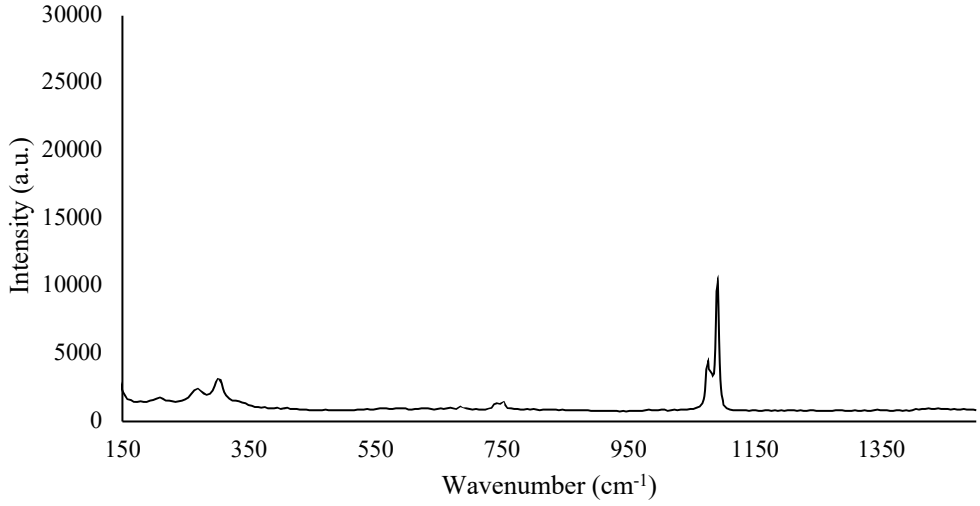

Figure 3.5. Raman spectrum of the minor precipitate produced during the preliminary experiment, consistent with spectra reported in the literature for the vaterite polymorph.

SEM images taken of the dominant and minor precipitates (**Figure 3.6**) were consistent with the findings of the Raman spectra. The dominant polymorph displayed crystals of clear rhombohedral morphology with defined edges and corners and well-developed flat faces, consistent with calcite.[91] Some aggregation of crystals was observed.[91] Conversely, the minor polymorph displayed aggregates of flat sheets with diameters of ≈ 20 μm and with morphology typical of vaterite grains.[103]

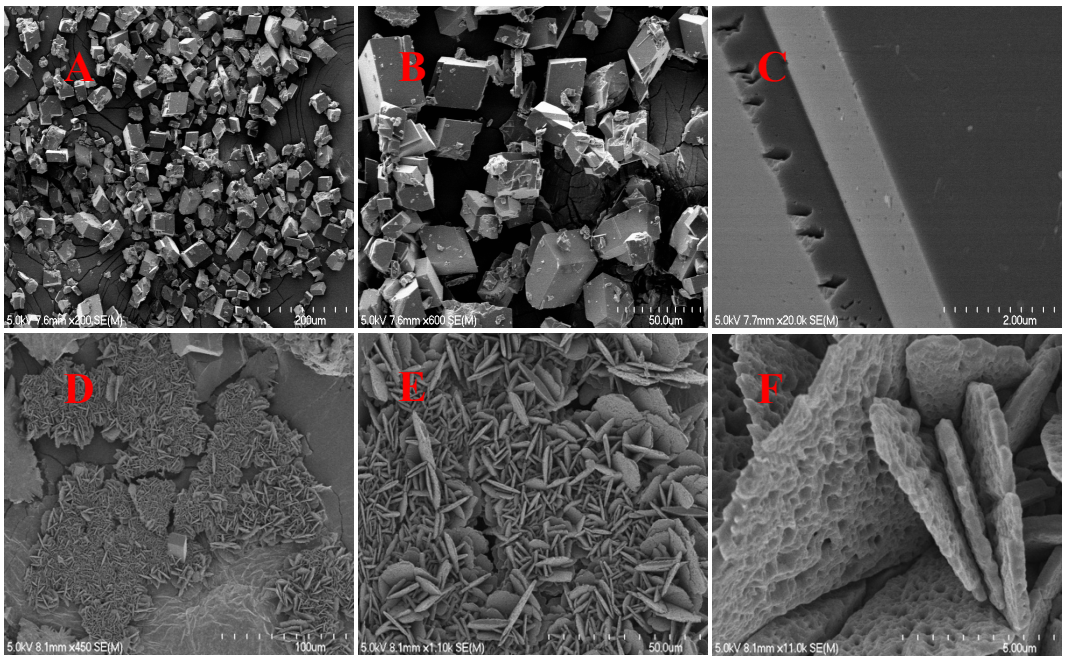

Figure 3.6. Representative SEM micrographs of the dominant (A-C) and minor (D-F) polymorphs of $CaCO_3$ precipitated during the preliminary experiment.

Structural characterisation of the precipitate confirmed that the main fraction was calcite, and thus the $CaCO_3$ crystals grown during the preliminary experiment were considered to be representative of speleothem calcite. As vaterite is uncommonly reported in speleothem samples, these patches were avoided when sampling for ICP-MS as the partitioning behaviour of metals would likely differ between polymorphs due to differences in coordination environments of the trace ions.

3.3.3 $CaCO_3$ Growth Rate

Growth rate of the $CaCO_3$ precipitate along the plate was determined according to the method reported by Hansen *et al.* (2013; 2017), details of which are given in

Section 1.2.4.[18, 20] Briefly, as electrical conductivity of the solution is dependent on $[Ca^{2+}]$, the conductivity data presented above were fitted to **Equation 1.6** using the statistical computing package R (**Figure 3.7**).[104] This allowed calculation of the time constant for precipitation of calcite, τ_{pr}, which was found to be 189 ± 18 s (see **Appendix I** for the R script). The relationship between conductance and $[Ca^{2+}]$ was then modelled using PHREEQC (**Figure 3.8**) so that the temporal evolution of electrical conductivity could be translated into the temporal evolution of $[Ca^{2+}]$ (see **Appendix I** for the PHREEQC script). **Equation 1.7** was then used alongside the linear relationship determined using PHREEQC to calculate the change in $[Ca^{2+}]$. Growth rates of $CaCO_3$ could then be calculated for each distance of flow, and the results are provided in **Table 3.4**. The calculated growth rates were similar to those observed in previous laboratory-based calcite growth experiments. Day and Henderson (2013) for instance observed growth rates ranging from 1.2 x 10^{-8} mmol cm^{-2} s^{-1} to 3.0 x 10^{-8} mmol cm^{-2} s^{-1}.

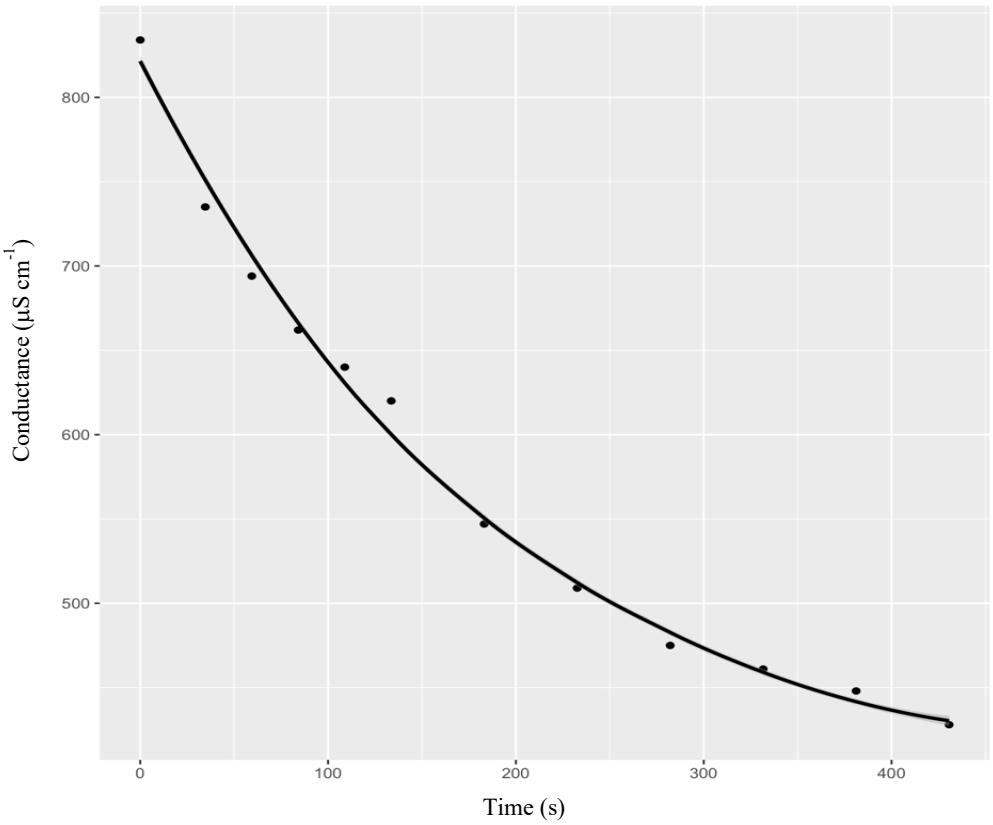

Figure 3.7. Evolution of the electrical conductivity of solution as a function of residence time on the glass plate. The solid line is the exponential fit of the experimental data according to Equation 1.7.[104-105]

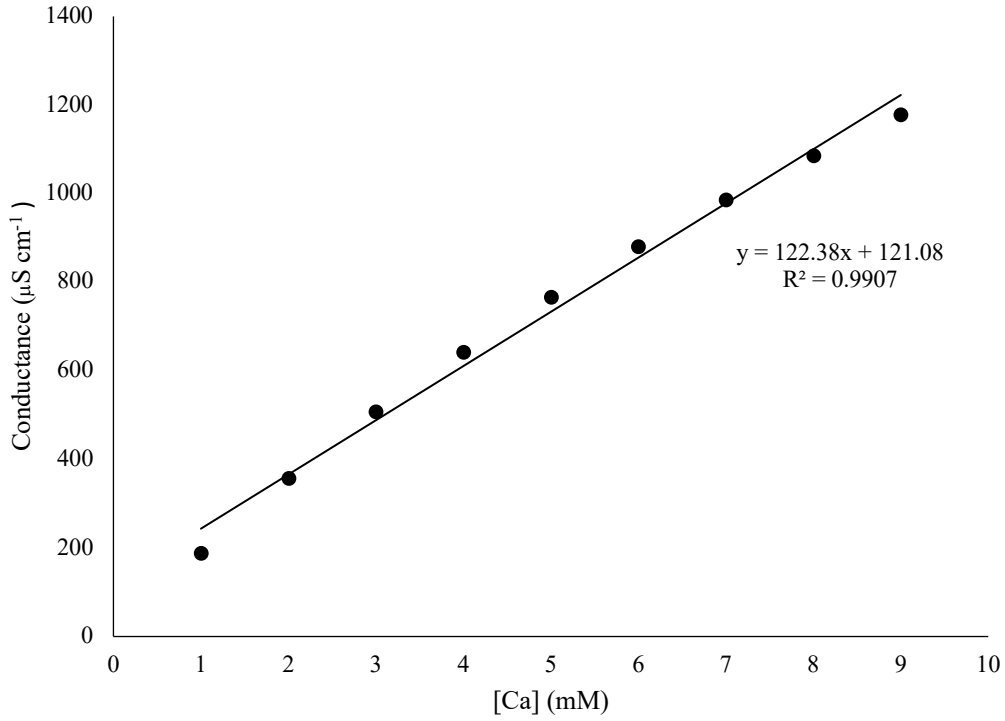

Figure 3.8. Linear relationship between the concentration of calcium and the conductance of the solution, modelled using PHREEQC.

Table 3.4. The conductance, residence time and growth rate of $CaCO_3$, *R*, calculated for each distance of flow during the preliminary experiment.

Distance of Flow (cm)	Conductance (µs cm^{-1})	Residence Time (s)	*R* (mmol cm^{-2} s^{-1})
0	834	0	1.33×10^{-7}
7	735	35	1.11×10^{-7}
12	694	59	9.70×10^{-8}
17	662	84	8.51×10^{-8}
22	640	109	7.46×10^{-8}
27	620	134	6.55×10^{-8}
37	547	183	5.04×10^{-8}
47	509	233	3.87×10^{-8}
57	475	282	2.98×10^{-8}
67	461	332	2.29×10^{-8}
77	448	381	1.76×10^{-8}
87	428	431	1.36×10^{-8}

3.3.4 Trace Element Partitioning

Although the primary purpose of the preliminary experiment was to establish a suitable method of precipitating $CaCO_3$ from a thin film in a manner analogous to precipitation on a speleothem surface, the partitioning of trace metals into calcite was also assessed and will be discussed here in brief. **Figure 3.9** below shows the trace element to calcium ratios (X/Ca) for Ni and Co in solution as precipitation progressed along the plate. No Cu/Ca data is presented as [Cu] was below the ICP-MS quantification limit in all but one of the solution samples, indicating Cu^{2+} was quickly lost from solution and readily incorporated into the $CaCO_3$ precipitate. This suggested that of the three transition metals investigated, Cu likely had the greatest affinity for the calcite lattice (assuming lattice substitution as the primary mode of trace element incorporation). The Cu/Ca ratio at 0 cm distance of flow was 0.018 ± 0.002.

Figure 3.9 shows an initial decrease in Co/Ca was observed in solution, followed by a slow increase as the distance of flow (i.e. residence time of the solution) increased. [Co]/[Ca] ratios ranged from 0.016 ± 0.002 to 0.027 ± 0.001 mM/M. An increasing trend in [Ni]/[Ca] as distance of flow increased was also observed, from 0.027 ± 0.002 to 0.048 ± 0.003 mM/M. These results indicated that Co^{2+} partitioned more readily into calcite under these conditions than Ni^{2+}. It was therefore expected that calculated partition coefficients (K_d values) would decrease in the order Cu > Co > Ni.

It can be seen from **Figure 3.9 (**C and D) that the calculated values for prior calcite precipitation (PCP) did not show a steady decrease with residence time, and thus were not in accordance with the observed conductance values. This likely resulted from the increased analytical error associated with measuring high concentrations of Ca, and made the effects of PCP on the partitioning of these metals during the preliminary experiment difficult to assess. For all following experiments the concentration range of the Ca standard curves was increased in order to reduce this error.

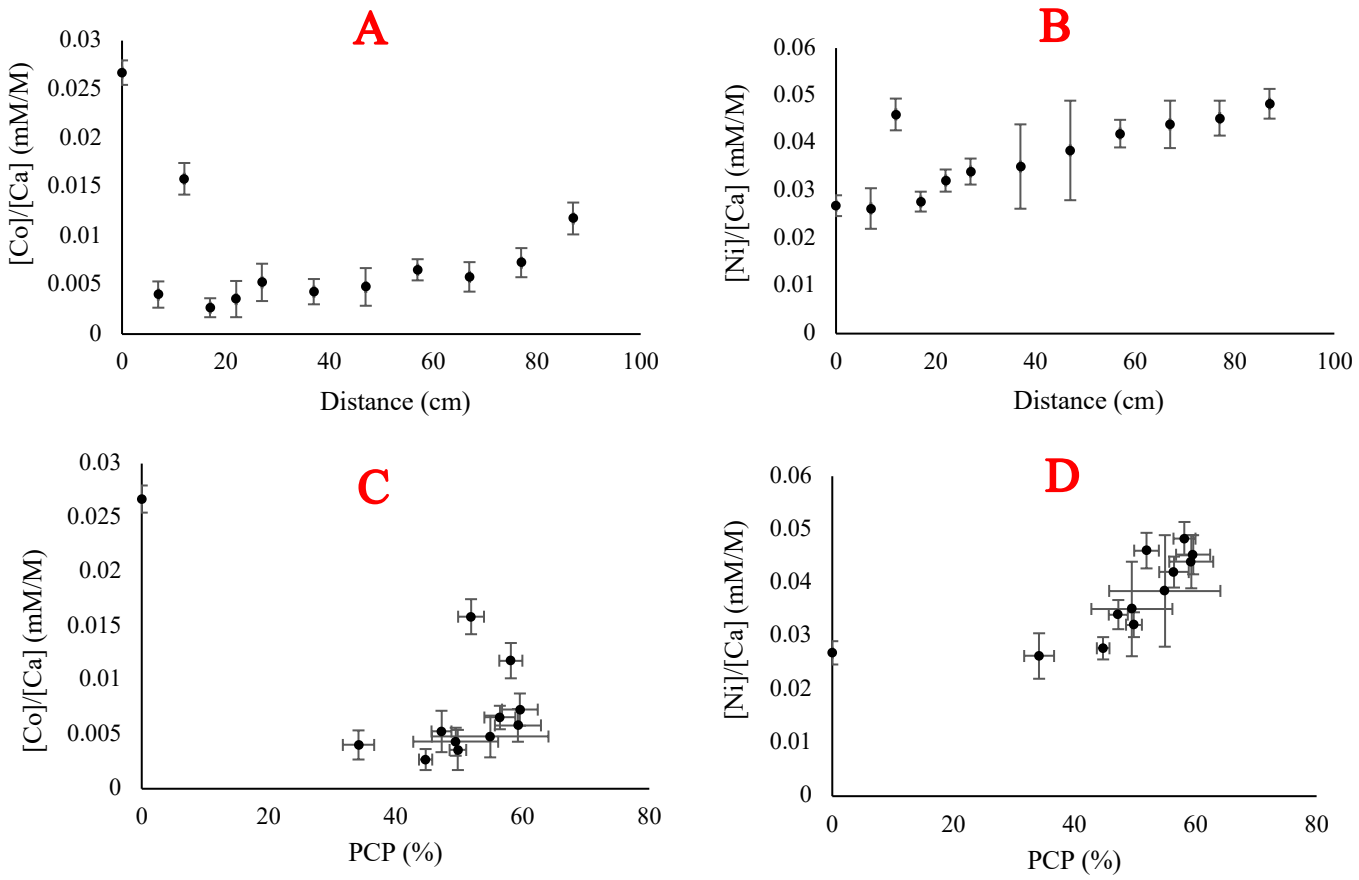

Figure 3.9. A) [Co]/[Ca] ratios measured in the solution samples taken at each distance of flow. B) [Ni]/[Ca] ratios measured in the solution samples taken at each distance of flow. C) The [Co]/[Ca] ratios plotted as a function of PCP. D) The [Ni]/[Ca] ratios plotted as a function of PCP. All errors are calculated from the standard deviation of triplicate ICP-MS measurements, and represent the analytical error only.

Corresponding X/Ca ratios measured in the precipitated calcite are presented in **Figure 3.10**. Cu/Ca ratios decreased as distance of flow increased, with [Cu] decreasing below the limit of quantification for ICP-MS measurements after 22 cm. This again was indicative of Cu^{2+} showing the highest degree of affinity for the calcite lattice. Both Co/Ca and Ni/Ca show fairly consistent values along the plate, with [Co]/[Ca] values in the range 0.025 ± 0.001 to 0.089 ± 0.02 mM/M and [Ni]/[Ca] values in the range 0.0043 ± 0.003 to 0.046 ± 0.004 mM/M. Sharp, unexpected increases in Ni/Ca and Co/Ca that could not be explained by analytical error were observed at 77 and 87 cm. The cause of these increases are not known with certainty, however significant amounts of vaterite were present in the last 10 cm of the glass plate. Thus, despite efforts to avoid vaterite during sampling, it is

probable some vaterite was sampled at 77 and 87 cm and analysed by ICP-MS. If partitioning of trace metals into the vaterite lattice occurs more readily than into calcite, this could account for the higher Co/Ca and Ni/Ca ratios observed. Further investigations into the partitioning behaviour of first-row transition metals into vaterite are required in order for this hypothesis to be tested.

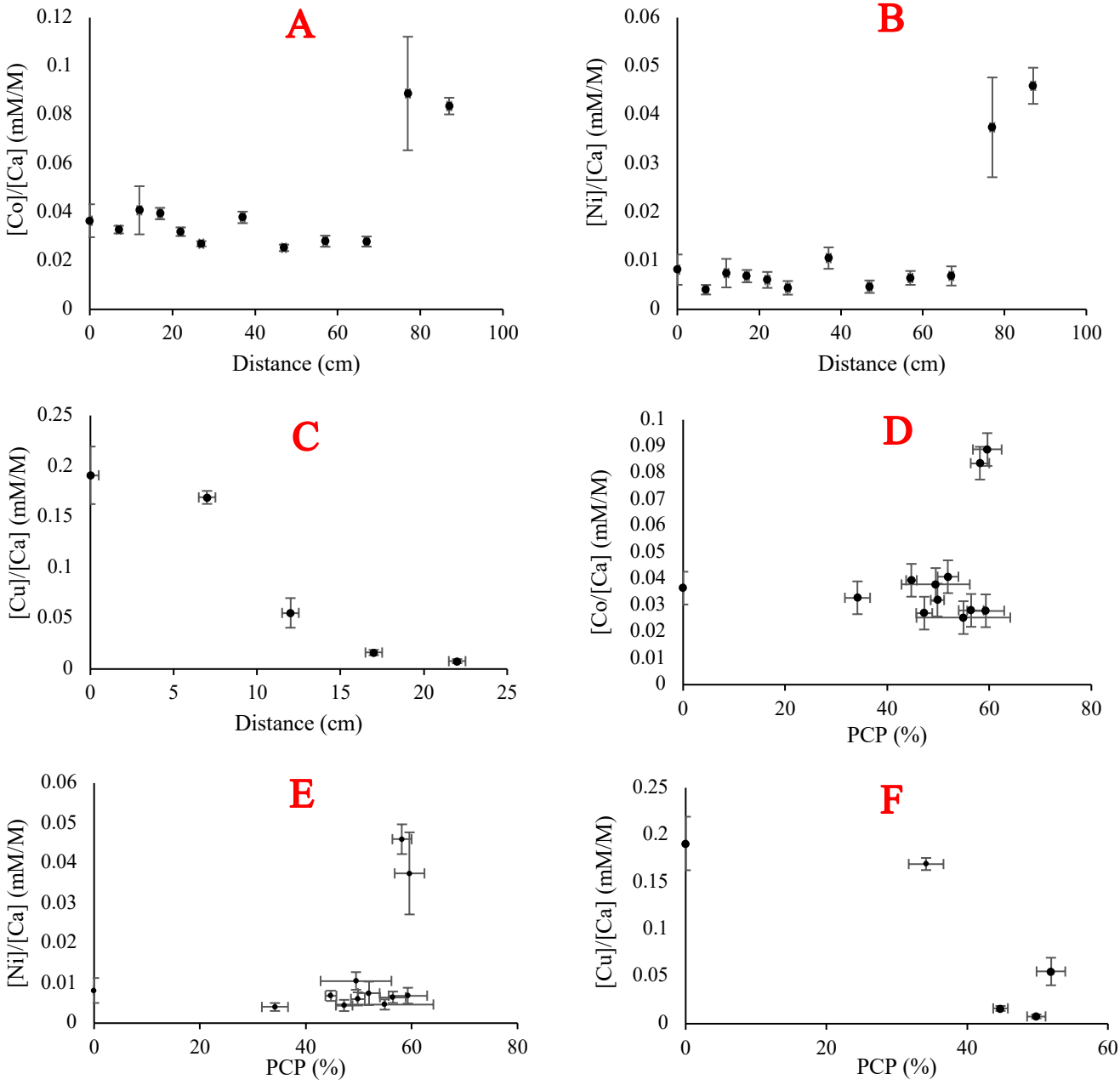

Figure 3.10. A) [Co]/[Ca] ratios measured in the calcite samples taken at each distance of flow. B) [Ni]/[Ca] ratios measured in the calcite samples taken at each distance of flow. C) [Cu]/[Ca] ratios measured in the calcite samples taken at each distance of flow. D) The [Co]/[Ca] ratios plotted as a function of PCP. E) The [Ni]/[Ca] ratios plotted as a function of PCP. F) The [Cu]/[Ca] ratios plotted as a function of PCP. All errors are calculated from the standard deviation of triplicate ICP-MS measurements, and represent the analytical error only.

The X/Ca ratios in the solution and precipitate were used to calculate K_d values for each metal along the plate (**Table 3.5**). Although large variations in K_d values were observed at different residence times, no overall trend in K_d with PCP, calcite growth rate or pH was observed for the metals. Despite the large error associated with most K_d values, these preliminary results shows distinctly different average K_d values for each metal, increasing in the order Ni (0.31 ± 0.27) < Co (6.9 ± 3.7) < Cu (10.6 ± 2.8).

Table 3.5. K_d values for Co, Ni and Cu measured at each distance of flow for the preliminary experiment. Errors in K_d values and PCP were calculated from the standard deviation of triplicate ICP-MS measurements.

Distance of Flow (cm)	Residence Time- Sampling Channel (s)	Residence Time- Reference Channel (s)	Extent of PCP (%)	K_d		
				Co	Ni	Cu
0	0	0	0	1.4 ± 0.32	0.30 ± 0.14	10.6 ± 2.8
7	35 ± 1	31 ± 3	34 ± 2	8.1 ± 3.1	0.15 ± 0.062	-
12	59 ± 2	53 ± 5	52 ± 8	2.6 ± 0.89	0.16 ± 0.075	-
17	84 ± 4	75 ± 7	45 ± 3	14.6 ± 6.1	0.25 ± 0.065	-
22	109 ± 5	98 ± 9	50 ± 15	8.9 ± 5.1	0.19 ±0.065	-
27	134 ± 6	120 ± 10	47 ± 9	5.1 ± 2.0	0.13 ± 0.052	-
37	183 ± 8	164 ± 14	49 ± 5	8.7 ± 3.1	0.30 ± 0.14	-
47	233 ± 10	209 ± 18	55 ± 9	5.3 ± 2.4	0.12 ± 0.066	-
57	282 ± 12	253 ± 22	56 ± 2	4.3 ± 1.1	0.15 ± 0.045	-
67	332 ± 14	297 ± 26	59 ± 4	4.8 ± 1.5	0.16 ± 0.063	-
77	381 ± 16	342 ± 30	60 ± 3	12.2 ± 5.7	0.83 ± 0.29	-
87	431 ± 18	386 ± 34	58 ± 2	7.1 ± 1.3	0.95 ± 0.14	-
			Average:	6.9 ± 3.7	0.31 ± 0.27	10.6 ± 2.8

It should be noted that the amount of Cu in the precipitated calcite was insufficient for isotopic measurements using Multi-Collector ICP-MS (MC-ICP-MS) at almost all distances of flow. This, coupled with the loss of measurable quantities of Cu^{2+} from solution within the first few centimetres, informed the decision to increase the Cu^{2+} concentration five-fold for the following experiments. Concentrations of Co^{2+} and Ni^{2+} were also increased to 50 ppb for ease of comparison.

3.4 Conclusion

The primary purpose of the preliminary crystal growth experiment carried out here was to develop a suitable method for calcite precipitation from a thin film in a manner analogous to growth on a speleothem surface. The results discussed above indicate that the method developed was suitable for the desired purpose, with film thickness, pH, electrical conductance and calcite growth rates comparable to those observed in similar experimental studies. Structural characterisation of the precipitate demonstrated that the major $CaCO_3$ polymorph was calcite and thus that the precipitate could thus be considered representative of speleothem calcite. Some minor changes to the experimental design were made based on these results, namely the aforementioned increases in film thickness and trace metal concentrations.

The preliminary trace element partitioning results indicated that Cu demonstrates the strongest partitioning behaviour into speleothem calcite, followed by Co and then Ni. These results are of relevance to speleothem science, as they indicate that at times of high PCP, it would be expected that very little Cu and possibly also Co would be present in the speleothem-forming dripwater *if no complexation with OM were occurring*. The following four experiments (discussed in **Chapter 4**) will investigate this in further detail, and the effects of organic ligand complexation on partitioning behaviour will be assessed.

4 Partitioning of Co, Ni and Cu Into Calcite Grown Under Cave Analogue Conditions

4.1 Introduction

It has become apparent in the past half century that speleothems are fundamental tools for terrestrial paleoclimate reconstructions.[1, 3, 5, 10, 13, 54, 88] Their wide geographical coverage and the ability to date their growth layers using U-Th and U-Pb radiometric dating has prompted extensive research into a range of paleoproxies.[1] To date, a significant number of proxies have been established and are used routinely, including stable oxygen and carbon isotopes (known to respond to variations in rainfall and temperature), fluorescence (indicative of the quality and quantity of organic matter present in cave dripwaters) and speleothem minerology (e.g. fabric defects and nano-crystal aggregation).[1] Trace metal proxies in speleothem archives have also garnered attention, as concentrations of trace metals and their stable isotopic ratios have been shown to respond to a variety of processes that occur in the karst system due to variations in environmental variables.[1, 4-5, 54]

Trace element incorporation into speleothem calcite is frequently described by the partition coefficient, $K_{d,}$. The partition coefficient may be used to relate the trace element content of a mineral phase to that of the solution phase from which it precipitated and is frequently normalised to the concentration of the 'carrier' element (Ca in the case of speleothems) (**Equation 4.1**):

$$K_d = \frac{(x/Ca)_s}{(x/Ca)_{aq}} \qquad (4.1)$$

where x is the trace element of interest. Thus, a $K_d > 1$ indicates preferential incorporation of the trace element over calcium, while a $K_d < 1$ indicates calcium is preferably incorporated into precipitated $CaCO_3$. [4-6, 45-46] The range of trace metals

used routinely as speleothem-based proxies is currently limited almost exclusively to metals which exhibit simple partitioning and for which $K_d << 1$, namely the alkali earth metals Sr and Mg, as the role of these elements in the karst system is comparatively well-constrained. These trace element proxies have proven particularly useful as indicators of past aridity, as a shift to higher Sr/Ca and Mg/Ca values as PCP increases is observed. Dripwater solutions (and subsequently speleothems) are enriched in these alkaline earth elements at times of increased PCP (i.e. aridity).[1,7] Although the use of such trace metals has proven invaluable for terrestrial paleoclimate reconstructions from speleothems, it has become apparent in the past decade that first-row transition metals such as Co, Ni and Cu may prove to be useful additions to the suite of elements used for paleohydrological reconstructions from speleothem archives.

It is known that the partitioning behaviour of metals that act as intermediate or soft Lewis acids (e.g. Cd, Zn, Co, Ni and Cu) is considerably different to the behaviour exhibited by the hard Lewis acids Sr and Mg, with theoretical predictions indicating distribution coefficients > 1 for these metals.[1] However, there are still many remaining uncertainties regarding the controls on their incorporation into speleothem calcite, as although theoretical partition coefficients are useful in understanding partitioning behaviour under certain conditions, the non-thermodynamic nature of partition coefficients during calcite precipitation in most natural contexts requires partitioning behaviour under speleothem-specific conditions to be established.[43] For instance, despite theoretical partition coefficients being greater than 1 for transition metals, apparent partition coefficients ($K_{d\ app}$) observed for actual speleothem samples are frequently less than 1 due to the dependence of $K_{d\ app}$ on a number of factors including calcite precipitation rate, crystal morphology, and, perhaps most importantly, complexation reactions between organic matter (OM) and trace ions. Data from Obir cave (Austria) for instance indicate $K_d << 1$ for Cu and Y, while K_d values obtained for Zn and Pb were >> 1, despite theoretical predictions indicating $K_d >> 1$ for all four elements.[106] It is now understood that this was likely a result of the variable dissociation kinetics of different metal-natural organic matter (NOM) complexes, with Cu and Y demonstrating a greater binding affinity for NOM.

Thus, it has become increasingly apparent that if transition metals are to be used as robust and reliable paleo-proxies, the role of NOM complexation in their transport through karst systems and on their partitioning behaviour into speleothem calcite must be accounted for. It has previously been mentioned (**Chapter 1**) that a strong correlation between trace metals and organic material has been observed in speleothem samples. [12, 14, 36, 40, 56, 61] For instance, Borsato *et al.* (2007) found that first-row transition metals were enriched in layers alongside NOM in the hierarchy Y > Zn, Cu, Pb > P and Br, reflecting the selectivity of transport by organic colloids flushed from the soil zone during seasonal infiltration events.[56] Further research in this area, undertaken by Hartland *et al.* (2011), demonstrated that colloidal NOM was a dominant complexant of Co, Ni, Cu and V in Poole's Cavern (Derbyshire, UK), highlighting the pitfalls associated with interpreting partitioning of these trace metals into speleothem carbonates as if they were present as free ions. Complexation of transition metals with NOM is likely to have significant effects on their partitioning into speleothem calcite and must be taken into account.[36]

As mentioned in **Chapter 1**, it has been suggested that the ratio of different first-row transition metals in speleothem samples could likely prove useful for providing insights into the composition of dripwaters with respect to NOM. [12-13] Hartland *et al.* (2012) observed distinct linear trends between Cu:Ni ratios and the acid-soluble NOM and poorly-soluble NOM end members in the soil leachates and cave dripwaters. Increases in mobilised particulate and colloidal OM during periods of increased infiltration (that also corresponded with increased concentrations of Cu, Ni, Fe, Sn and Mn) were also observed, and NOM present during periods of decreased infiltration was found to be substantially finer and primarily dissolved. The differences in Cu:Ni ratios between periods of high and low water supply were thus attributed to the presence of stronger binding sites in coarser OM compared to smaller humic like colloids, and the competitive binding of Cu over Ni for these sites.[12, 57] This study further illustrated the potential of first-row transition metals, which have historically been largely overlooked as speleothem-based proxies, to provide important paleoclimatic information.[12-13]

Co, Ni and Cu may be particularly good candidates for novel paleoclimate proxies as they are abundant members of the first-row transition metals, are present in both

cave waters and speleothems, and, being transition metals, they exhibit a range of behaviours that are not shown by the alkali earth metals. Notably they complex strongly to organic ligands (as dictated by the Irvin-Williams series), and the strong complexation of these elements by NOM is likely to significantly alter both their availability for incorporation into calcite and their isotopic fractionation.[66] Cu in particular forms highly stable complexes with organic ligands, due to stabilisation caused by the Jahn-Teller distortion, and thus is of particular interest in this study. Proof of the importance of this stability on Cu speciation in cave waters was provided by Hartland and Zitoun (2018).[61] They confirmed that Cu complexation by NOM is almost certainly a universal property of cave waters and were also able to determine that the presence of NOM reduced the concentration of 'available' Cu (i.e. Cu present in simple inorganic complexes or as aquo-Cu^{2+} species) in solution by five orders of magnitude when compared to the total Cu concentration.[61] They demonstrated that even when the concentration of total Cu increased, the concentration of available Cu stayed consistently low, indicating that complexation with NOM was inhibiting the available Cu for partitioning into the Ca^{2+} lattice position of calcite.[61]

As mentioned in **Chapter 1**, Hartland *et al.* (2014) also found the strength of metal-NOM complexes to be a significant factor in determining the trace element content of speleothems. They found that the empirical $K_{d\ app}$ values observed were dependent on the 'free' aqueous fraction of metal, f_m, (i.e. the fraction of metal not bound to NOM) and proposed that divergences between the $K_{d\ app}$ and $K_{d\ act}$ values of these transition metals were largely explained by the concentration of 'free' metal in the dripwaters, according to **Equation 1.16** (equation repeated below for the ease of the reader).[40] It was proposed, therefore, that differences in the preservation of each trace metal in calcite could be explained quantitatively by their complexation behaviour with NOM if further data on inorganic $K_{d\ act}$ values and complexation reactions between NOM and metals were available.[40]

$$f_{m(aq)} = \frac{\frac{M_{(s)}}{Ca_{(s)}}Ca(aq)}{K_d} M_{(aq)} \qquad \textbf{(1.16)}$$

The purpose of this chapter is therefore twofold: Firstly, the study aims to address the need for the partitioning behaviour of the promising new proxies Co, Ni and Cu to be established for speleothem-specific conditions so that reliable $K_{d\ act}$ values may be obtained. Although empirical partition coefficients for these first-row transition metals are available, they are only available from marine-type studies or from calcite precipitation in caves where complexation by NOM results in empirical partition coefficients dependent on the concentration of 'free' (i.e. non-complexed) metal in the dripwaters. Secondly, this study aims to assess the degree to which complexation of Co, Ni and Cu by organic ligands affects their partitioning into speleothem-like calcite, to help aid the interpretation of Co, Ni and Cu signals in speleothem samples. These objectives will help to establish whether Cu, Ni and Co are viable and robust paleoclimate proxies in speleothems that may be used in a multi-proxy approach for paleoclimate reconstructions. This in turn may assist speleothem scientists worldwide to interpret their records with a higher degree of certainty and provide information on past climatic events that could help us to better understand our current and changing climate.

4.2 Methods

Four experiments were carried out in order to meet the aims of this study. Two solely inorganic crystal growth experiments (experiments 1 and 2) were undertaken initially to provide speleothem-specific $K_{d\ act}$ values for Co, Ni and Cu. Two experiments with organic ligands of varying binding strengths were subsequently carried out to determine the degree to which NOM complexation affects the partitioning of these metals. The chelating ligand NTA (experiment 3) was chosen on the basis of the high stability constants observed for Co-NTA, Ni-NTA and Cu-NTA complexes (see **Table 1.1**), and the conditional stability constants found by Hartland and Zitoun (2018) for Cu-NOM complexes in dripwaters from four caves in Aotearoa (New Zealand) ($\log K_{\text{Cu-NOM}} \approx 13.5\text{-}15.5$).[61] SRFA (experiment 4) was chosen as it's heterogeneity is more representative of NOM observed in karst systems, and it has been well-characterised in the literature. Ligand concentrations used were chosen in order to provide high levels of trace metal complexation, as is

observed for Co, Ni and Cu in typical cave dripwaters.[40, 61] Due to limitations on the amount of SRFA available, only Cu was present in experiment 4 so as to ensure a high percentage of metal complexation.

Details of the experimental design, solution composition and thin film characteristics for all four experiments are outlined in **Section 2.2**. Analytical methodologies for ICP-MS, FT-IR spectroscopy, SEM, pXRD and 3DEEM fluorescence are also outlined in **Chapter 2**.

4.3 Results and Discussion

4.3.1 Control of Environmental Parameters

To ensure calcite was grown under cave-analogue conditions, and that subsequently speleothem-specific partition coefficients could be obtained, precise control over environmental variables inside the GeoMIC chamber were required. Conditions of 1000 ppmV CO_2, 80 – 100% humidity and 20° C were chosen based on typical cave conditions and previous work undertaken by Hansen *et al.* (2017).[20] Environmental conditions were logged at 1 min intervals, and were well-controlled throughout each experiment (**Figure 4.1**).

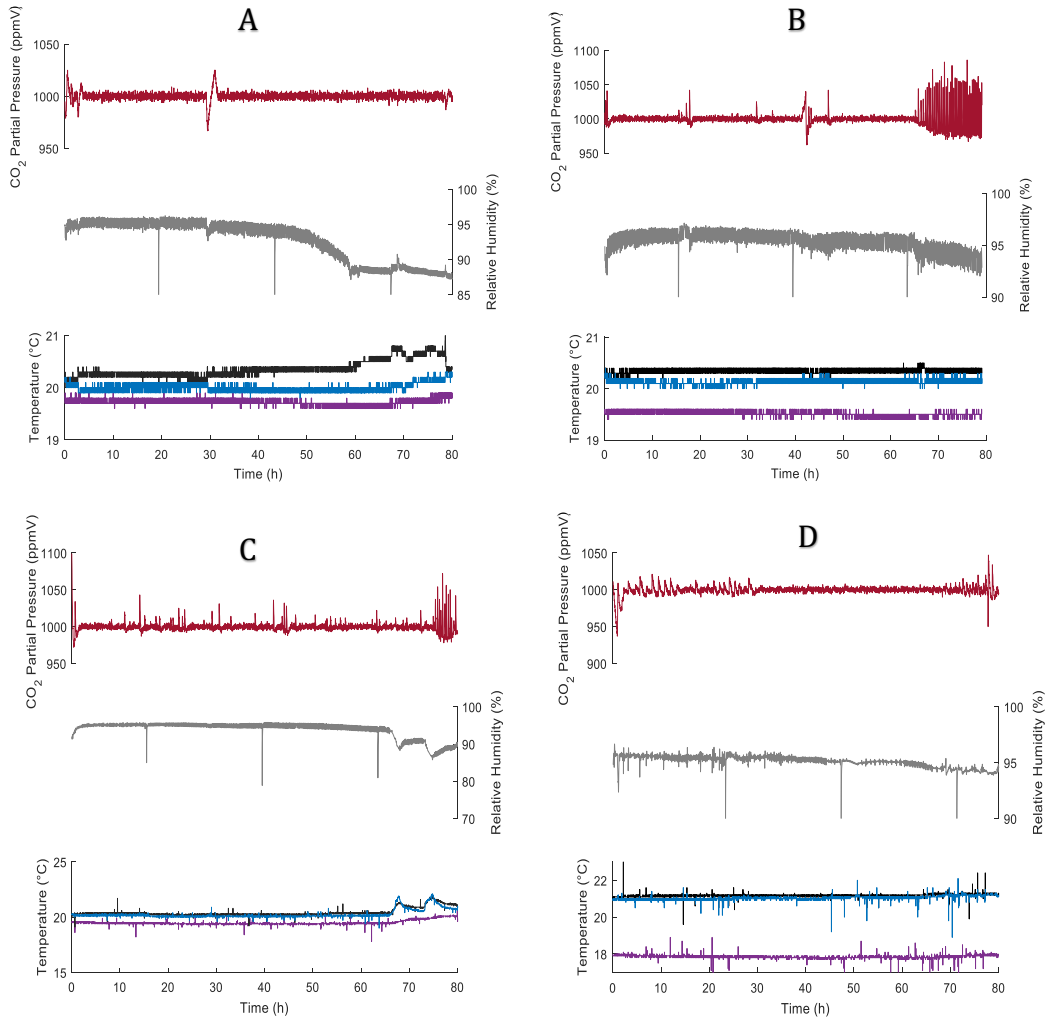

Figure 4.1. Environmental parameters logged at 1 min intervals for experiments 1 (A), 2 (B), 3 (C) and 4 (D). Large decreases in humidity at regular 25 h intervals are assumed to be the result of an instrumental artefact and to not reflect true decreases in humidity. Black and blue lines represent temperature at the sample port end and the drip-site end of the GeoMIC chamber, respectively. The purple line represents the temperature inside the solution reservoir.

4.3.2 Aqueous Speciation Modelling

The species distribution in the initial reservoir solutions was modelled using visual MINTEQ 3.0 speciation codes (**Table 4.1**). Complexation with SRFA was modelled using the NICA-Donnan model in visual MINTEQ which utilises a bimodal, continuous distribution for protons and metal ions.[107] The results indicated that Cu, Ni and Co in the inorganic system (experiments 1 and 2) were present primarily as aquo-M^{2+} species or in simple inorganic complexes expected to be

characterised by fast dissociation rates. In contrast, for experiment 3, model results showed M-NTA$^-$ species constituted 90, 99 and 99.8% of species for Co, Ni and Cu, respectively. Cu-SRFA complexes accounted for 96 % of Cu species in experiment 4. The proportions of complexed metal and free metal were similar to that found for Cu by Hartland and Zitoun (2018) in dripwater samples from four NZ cave sites. They found that available Cu was consistently low despite widely varying concentrations of total Cu, and essentially that all available Cu was strongly complexed to organic ligands.[61]

Table 4.1. Species distributions for initial reservoir solutions modelled using visual MINTEQ 3.0 speciation codes.

		Experiment 1 (Inorganic)	Experiment 2 (Inorganic)	Experiment 3 (NTA)	Experiment 4 (SRFA)
Component	**Species**	**Proportion of Total Concentration (%)**			
Co^{2+}	Co^{2+}	70	70	7.2	-
	$CoHCO_3^+$	29	29	3	-
	$CoCO_{3\ (aq)}$	0.79	0.79	0.082	-
	Co-NTA$^-$	-	-	90	-
Ni^{2+}	Ni^{2+}	59	59	0.56	-
	$NiHCO^{3+}$	39	39	0.38	-
	$NiCO_{3\ (aq)}$	1.3	1.3	0.012	-
	Ni-NTA$^-$	-	-	99	-
Cu^{2+}	Cu^{2+}	20	20	0.019	0.79
	$CuCO_{3\ (aq)}$	71	71	0.065	2.8
	CuNTA$^-$	-	-	99.8	-
	SRFA-Cu	-	-	-	96
Ca^{2+}	Ca^{2+}	93	93	93	93
	$CaHCO_3^+$	6.6	6.6	6.6	6.5
	$CaCO_{3\ (aq)}$	0.085	0.085	0.085	0.084
	Ca-NTA$^-$	-	-	-	-
	SRFA-Ca	-	-	-	0.26
CO_3^{2-}	$CaHCO^{3+}$	1.8	1.8	1.8	1.8
	$CaCO_{3\ (aq)}$	0.024	0.024	0.024	0.024
	HCO_3^-	54	54	54	54
	$H_2CO_{3\ (aq)}$	44	44	44	44

4.3.3 Structural Characterisation of $CaCO_3$

In order to determine the dominant polymorphs of $CaCO_3$ that precipitated during each experiment, Raman Spectroscopy, pXRD and SEM analyses were carried out on representative $CaCO_3$ precipitates from each experiment. The results of these three analytical techniques will be discussed below.

FT-IR spectra (**Figure 4.2**) of the precipitated $CaCO_3$ in each experiment show the characteristic v_4 and v_2 bands of calcite at 713 cm^{-1} and 874 cm^{-1}, respectively, for all four experiments and were consistent with spectra reported by Ni and Ratner (2008) for pure calcite crystals.[90-91] Spectra for experiments 1-3 however also show the characteristic v_4 band of vaterite at 744 cm^{-1} and a band at ~1090 cm^{-1} (mode unknown) also reported for vaterite by Ni and Ratner (2008).[90] These bands were not observed for $CaCO_3$ precipitated during experiment 4. Characteristic bands for aragonite (v_2 at 858 cm^{-1} and v_4 at 700 cm^{-1}) were absent from all spectra.[90] In order to ensure the polymorph remained consistent along the flow path during each experiment, samples from three different distances along the plate were taken for analysis, however only one spectrum for each experiment is included in **Figure 4.2** for purposes of clarity. Results indicated that the polymorphs of $CaCO_3$ along the plate remained consistent in each experiment.

pXRD was also carried out on precipitates from experiments 1-3, however an insufficient amount of $CaCO_3$ for this analysis precipitated during experiment 4. The pXRD pattern obtained for the precipitates were consistent with the FT-IR results, indicating a mixture of calcite and vaterite.[90] All major peaks reported in the literature for calcite were observed, while some minor peaks indicative of vaterite were also seen at 2θ diffraction angles 55, 50, 33 and 25 (**Figure 4.3**).[90]

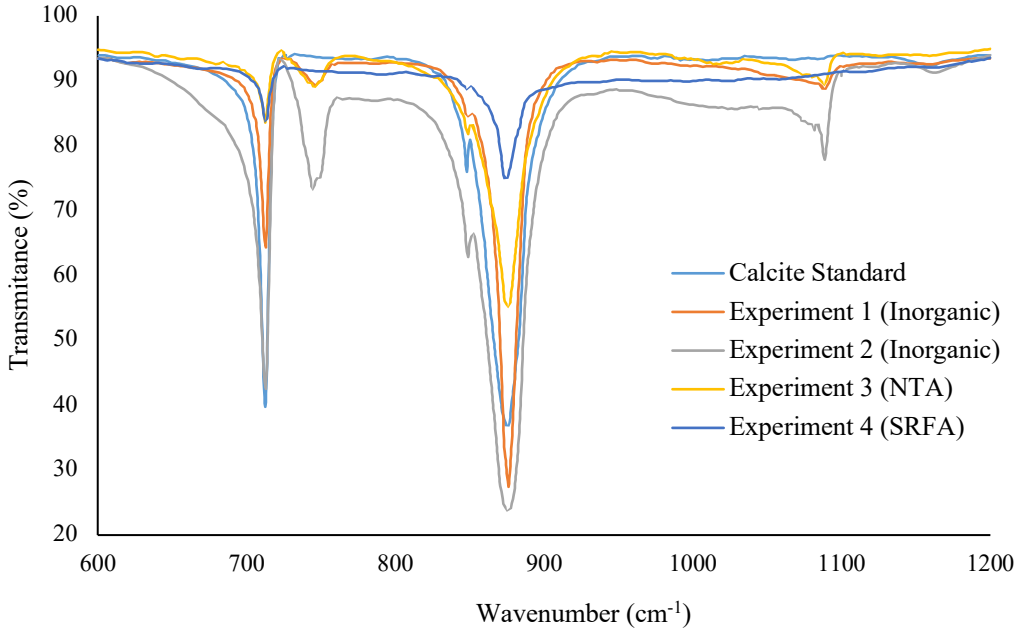

Figure 4.2. IR spectra of the $CaCO_3$ precipitated at a distance of flow of 65-70 cm during experiments 1-4. A spectrum of a calcite standard is included for comparison purposes.

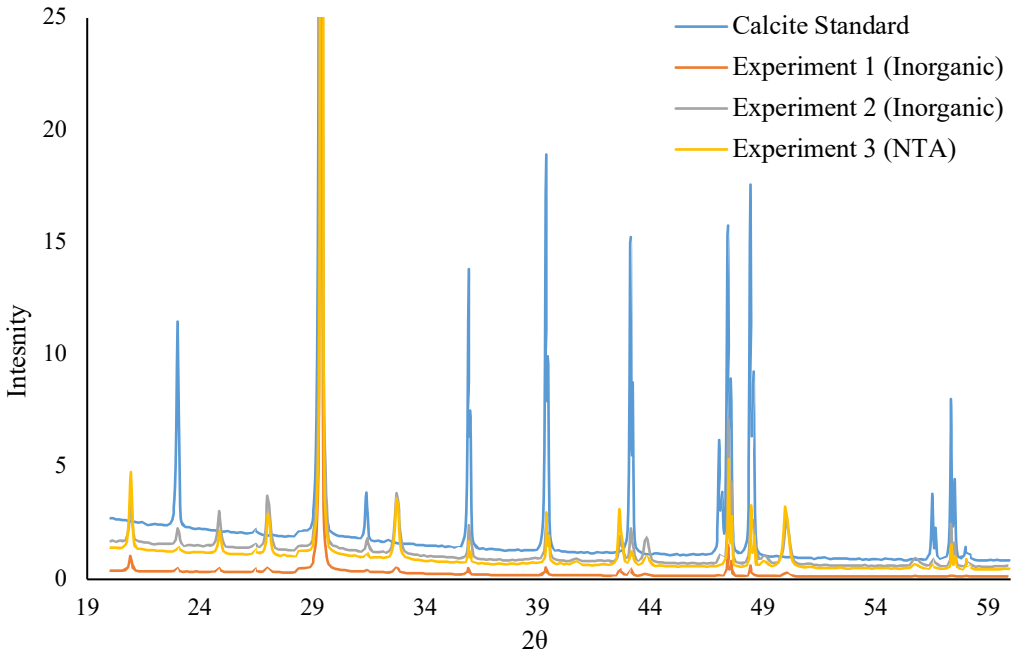

Figure 4.3. pXRD patterns of the $CaCO_3$ precipitated at a distance of flow of 65-70 cm during experiments 1-3. A pXRD pattern of a calcite standard is included for comparison purposes.

The presence of small quantities of vaterite in precipitate samples from experiments 1-3, the absence of vaterite observed for experiment 4 and the absence of vaterite in the dominant precipitate grown during the preliminary experiment (reported in **Chapter 3**) were indicative of changes in polymorph caused by varying total trace metals concentration. It has previously been observed that high concentrations of trace metals cause changes in $CaCO_3$ crystal morphology and polymorph (formation of aragonite at high trace metals concentrations has been well documented) and therefore it is likely the higher concentrations of trace metals in experiments 1-3 ($[M]_{total}$ = 150 ppb) caused the precipitation of vaterite.[108-109] Only rhombohedral calcite was precipitated during experiment 4, presumably due to lower total concentrations of trace metals ($[M]_{total}$ = 50 ppb). Although calcite is the primary $CaCO_3$ polymorph present in speleothems, Frisia *et al.* (2018) identified that vaterite crystals are likely one of the many possible initial states of speleothem crystallization.[110] Because vaterite was only a minor contributor to the $CaCO_3$ precipitated during these experiments, our results are considered to be representative of speleothem $CaCO_3$ deposits.

SEM micrographs were also taken of precipitates from experiments 1-3 to provide details on crystal morphology (**Figure 4.4**). Due to limited access to instrumentation, precipitates from experiment 4 could not be analysed via SEM. If further work were to be undertaken in this area it is suggested that this analysis should be carried out on precipitates from experiment 4 in order to assess the impact of high SRFA concentrations on crystal morphology (and thus potentially trace metal partitioning). SEM micrographs supported the FT-IR spectroscopy and pXRD analyses, with the majority of crystals precipitated in all three experiments displaying rhombohedral morphology consistent with calcite.[91] Overgrowth, aggregation of crystals and growth defects were observed to varying degrees for all experiments, with the highest proportion of defects observed for experiment 3. As expected, a minority of crystals displaying morphology typical of vaterite were also observed in all three experiments.[91]

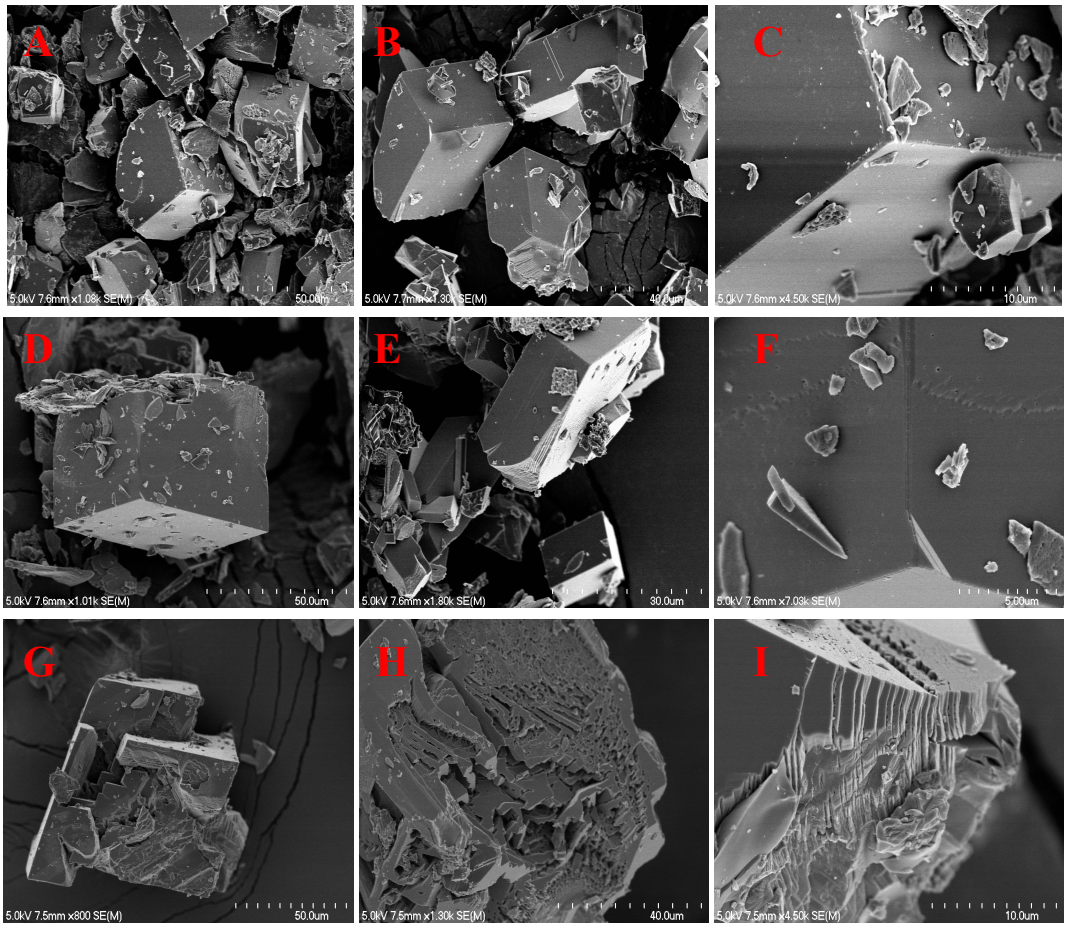

Figure 4.4. Representative SEM micrographs of the $CaCO_3$ precipitated during experiments 1 (A-C), 2 (D-F) and 3 (G-I).

The presence of organic material in solution was found to cause morphological changes in calcite crystals. Crystals formed under inorganic conditions displayed clear rhombohedral morphology with defined edges and corners and well-developed flat faces. Calcite crystals grown in the presence of 2 ppm NTA in contrast displayed rounded corners and a high density of steps and of sub-micron scale kinks on the crystal faces. These features have previously been identified in calcite grown in the presence of OM.[91, 110] Although no SEM data could be obtained for precipitates formed in the presence of SRFA, it is likely that these effects would be more pronounced in the calcite crystals grown during experiment 4 due to the high concentrations of SRFA (20 ppm).

4.3.4 $CaCO_3$ Growth Rates

Growth rate (*R*) of the $CaCO_3$ precipitate along the plate (**Table 4.2**) was determined according to the method reported by Hansen *et al.* (2013; 2017), details of which are given in **Sections 1.2.4** and **3.3.3**.[18, 20] Conductivity data fitted to **Equation 1.6** (used to calculate the time constant for precipitation of calcite, τ_{pr}) for all four experiments can be found in **Appendix II**. Growth rates were similar to those observed in previous laboratory-based calcite growth experiments, for example Day and Henderson (2013) observed growth rates ranging from 1.2×10^{-8} mmol cm^{-2} s^{-1} to 3.0×10^{-8} mmol cm^{-2} s^{-1}.

Growth rates determined for experiment 4 were significantly lower than those calculated for other experiments. This was consistent with the observation that very little precipitate was deposited on the glass plate during experiment four. This resulted in an insufficient amount of precipitate sample for ICP-MS at most distances of flow. The inhibitory effect of high concentrations of OM on calcite growth have previously been documented in the literature (e.g. Pearson *et al.* 2020), however the concentration of SRFA utilised in this experiment was necessary in order to ensure complexation of the majority of the Cu present in solution, so as to replicate conditions found in real karst systems.[61] If less Cu had been present in solution, a lower concentration of SRFA could have been used to ensure these conditions, however there would then have been insufficient Cu available for isotopic fractionation to be assessed.

Table 4.2. Growth rates, *R*, and corresponding residence times calculated for each distance of flow during experiments 1-4.

Distance of Flow (cm)	Experiment 1		Experiment 2		Experiment 3		Experiment 4	
	Residence Time (s)	*R* (mmol cm^{-2} s^{-1})	Residence Time (s)	*R* (mmol cm^{-2} s^{-1})	Residence Time (s)	*R* (mmol cm^{-2} s^{-1})	Residence Time (s)	*R* (mmol cm^{-2} s^{-1})
0	0	2.0×10^{-7}	0	3.8×10^{-7}	0	1.9×10^{-7}	0	1.3×10^{-7}
2	6 ± 0.56	1.9×10^{-7}	-	-	-	-	-	-
3	-	-	-	-	-	-	8 ± 1.2	1.2×10^{-7}
5	-	-	14 ± 0.53	3.2×10^{-7}	23 ± 0.8	1.7×10^{-7}	-	-
7	21 ± 2.0	1.8×10^{-7}	-	-	-	-	-	-
9	-	-	26 ± 1.0	2.8×10^{-7}	41 ± 1.4	1.6×10^{-7}	24 ± 3.6	9.8×10^{-8}
12	35 ± 3.4	1.6×10^{-7}	34 ± 1.3	2.6×10^{-7}	54 ± 1.8	1.5×10^{-7}	32 ± 4.8	9.0×10^{-8}
17	50 ± 4.8	1.5×10^{-7}	48 ± 1.8	2.2×10^{-7}	77 ± 2.6	1.4×10^{-7}	46 ± 6.8	7.9×10^{-8}
27	79 ± 7.6	1.2×10^{-7}	77 ± 2.9	1.6×10^{-7}	122 ± 4.1	1.2×10^{-7}	72 ± 11	6.0×10^{-8}
37	109 ± 10	1.0×10^{-7}	105 ± 3.9	1.1×10^{-7}	167 ± 5.6	9.7×10^{-8}	99 ± 15	4.6×10^{-8}
47	138 ± 13	8.7×10^{-8}	134 ± 5.0	8.0×10^{-8}	212 ± 7.1	8.1×10^{-8}	126 ± 19	3.5×10^{-8}
57	168 ± 16	7.3×10^{-8}	162 ± 6.1	5.7×10^{-8}	257 ± 8.6	6.8×10^{-8}	153 ± 23	2.6×10^{-8}
65	-	-	-	-	-	-	175 ± 26	2.1×10^{-8}
67	197 ± 19	6.1×10^{-8}	191 ± 7.1	4.1×10^{-8}	302 ± 10	5.6×10^{-8}	-	-
85	250 ± 24	4.5×10^{-8}	242 ± 9.0	2.3×10^{-8}	-	-	228 ± 34	1.2×10^{-8}
89	-	-	-	-	401 ± 14	3.8×10^{-8}	-	-

4.3.5 Trace Metal Partitioning Under Inorganic Conditions

The partitioning of Co and Ni into $CaCO_3$ was assessed at a range of distances along the plate for experiments 1-2. In order to do this, trace metal and Ca concentrations in solution and precipitate samples at each distance were assessed via ICP-MS. These concentrations are presented in **Appendix II**. **Equation 4.1** was used in order to calculate K_d values for each element at different distances of flow, and to calculate a K_d value averaged over the entire plate for each element (**Table 4.3**). It should be noted that no Cu data is available for experiment 2. This is a result of [Cu] falling below the quantification limit (QL) of ICP-MS for solution samples taken from all distances of flow. This is likely the result of a small amount of $CaCO_3$ precipitation occurring in the solution reservoir and tubing before sampling was

undertaken, and the high partition coefficient of Cu ensuring its incorporation into this precipitate. Although Cu was measurable in three of the solution samples taken during experiment 1, its high partition coefficient again resulted in [Cu] falling below the QL after 12 % PCP had occurred as it was readily incorporated into the precipitated calcite. This is consistent with the high K_d values reported for Cu in the literature.[48]

Table 4.3. Partition coefficients calculated for Co, Ni and Cu during inorganic experiments 1 and 2.

Experiment 1					Experiment 2				
Distance of Flow (cm)	PCP (%)	K_d			Distance of Flow (cm)	PCP (%)	K_d		
		Co	Ni	Cu			Co	Ni	Cu
2 ± 0.5	0	2.6 ± 0.2	0.75 ± 0.05	34 ± 3	5 ± 0.5	0	1.80 ± 0.3	0.35 ± 0.07	< QL
7 ± 0.5	7.9 ± 0.2	2.5 ± 0.1	0.46 ± 0.03	60 ± 2	9 ± 0.5	10.5 ± 0.5	1.97 ± 0.1	0.27 ± 0.02	< QL
12 ± 0.5	11.5 ± 0.4	3.0 ± 0.2	0.55 ± 0.03	120 ± 7	12 ± 0.5	13.0 ± 0.5	2.49 ± 0.5	0.32 ± 0.07	< QL
17 ± 0.5	15.0 ± 0.6	6.0 ± 0.3	1.1 ± 0.07	< QL	17 ± 0.5	16.7 ± 0.7	2.80 ± 0.2	0.31 ± 0.03	< QL
27 ± 0.5	21.6 ± 0.4	8.8 ± 0.3	1.5 ± 0.04	< QL	37 ± 0.5	25.6 ± 1.4	5.92 ± 0.6	0.76 ± 0.08	< QL
37 ± 0.5	27.0 ± 1.1	9.7 ± 1.1	1.6 ± 0.15	< QL	47 ± 0.5	28.0 ± 1.7	7.87 ± 0.7	0.98 ± 0.08	< QL
47 ± 0.5	32.2 ± 1.2	8.7 ± 0.5	1.4 ± 0.06	< QL	67 ± 0.5	34.2 ± 1.6	7.09 ± 0.6	1.08 ± 0.10	< QL
57 ± 0.5	35.1 ± 0.9	7.8 ± 0.6	1.4 ± 0.07	< QL	85 ± 0.5	36.2 ± 1.8	12.46 ± 1.0	1.30 ± 0.11	< QL
67 ± 0.5	39.1 ± 1.6	8.5 ± 1.1	1.6 ± 0.20	< QL	-	-	-	-	-
85 ± 0.5	47.0 ± 1.9	3.7 ± 0.2	0.96 ± 0.05	< QL	-	-	-	-	-
Average K_d for Entire Plate:		**4.4 ± 0.3**	**1.1 ± 0.1**	**44 ± 3**	**Average K_d for Entire Plate:**		**3.6 ± 0.5**	**0.7 ± 0.01**	< QL

The order of partition coefficients calculated for Co, Ni and Cu from both inorganic experiments were consistent with previously determined literature values. Wang and Xu (2001) for instance, developed a linear free energy correlation model to predict unknown partition coefficients based on only the chemical bonding energies of cations within a host mineral and the excess energy resulting from size differences between the host cations and the substituting trace ion.[48] They predicted partition coefficients for Co, Ni and Cu partitioning into calcite of 9.33, 3.47 and 37.15, respectively indicating that Cu would incorporated most readily into the calcite, followed by Co and then Ni. The results found here are evidently consistent with this prediction.

Apparent partition coefficients ($K_{d\ app}$ values) reported for these trace metals in cave systems are significantly lower than those determined here. For example Hartland *et al.* (2014), studying partitioning in a hyperalkaline cave system, found $K_{d\ app}$ values of 0.05, 0.36 and 0.62 for Co, Ni and Cu, respectively.[40] The discrepancy between these values is consistent with the interpretation that their partitioning must have been mediated to a large degree by OM complexation. The high inorganic K_d values calculated here also indicate that if little or no complexation of metals such as Cu and Co were occurring in karst systems, it is likely they would not be present in an appreciable amount at all in cave dripwaters or speleothem formations, as their high affinity for adsorption, substitution into the calcite lattice, or formation of other insoluble phases (e.g. $Cu(OH)_2$) would likely result in their loss from solution altogether up-flow from the speleothem, especially during periods of high PCP. The calculated K_d values therefore highlight that the transport and partitioning of first-row transition metals in cave systems must be heavily mediated by OM complexation.

The average K_d value determined in experiment 1 for Ni is consistent within error with that determined by Stipp and Lakshtanov (2007), who found that for dilute solid solutions, Ni partition coefficients were approximately 1.[111] A K_d value of 1 is of significance because, as was found by Stipp and Lakshtanov (2007), calcite precipitation rate should not significantly alter the partitioning behaviour of Ni.[111] Indeed, the results found here indicate that Ni may be a good speleothem-based proxy as its partitioning behaviour, like that of the alkali earth metals, is relatively simple under inorganic conditions, but unlike these elements is not substantially impacted by PCP.

The results provided in **Table 4.3.** indicate that as PCP progressed, K_d values for each element changed. This is unsurprising because as solution composition changes along the plate, the system cannot be considered to be in equilibrium. Thus although average K_d values for the entire plate are presented, it may be insufficient to describe the partitioning of these metals by a singular, static, K_d value. If inorganic partition coefficients from this study were to be applied to a real cave system, it may, therefore, be more appropriate to use the K_d values determined for the first few distances of flow, particularly if the speleothem archive in question is

a stalagmite. The residence time of dripwater on a stalagmite is usually short as drips are replaced quickly and flow down the side of the stalagmite. Thus, the partitioning of uncomplexed Co, Ni and Cu would be better described by the K_d values determined for the shortest residence times, as these are likely to be the closest to the true equilibrium partition coefficients.

Modelling of expected M/Ca ratios as PCP progressed was undertaken using **Equation 4.1** in order to determine whether the M/Ca ratios could be predicted based on known partition coefficients. Both the averaged experimental K_d values determined in this study (presented in **Table 4.3**) and literature partition coefficients discussed above were employed. **Figures 4.5** and **4.6** show modelling results alongside experimental M/Ca ratios determined for experiments 1 and 2, respectively.

Co/Ca ratios in solution samples taken during both inorganic experiments were well described by the predicted model based on **Equation 4.1** and the experimentally determined (static) partition coefficients. In comparison, the model employing the theoretical partition coefficient determined by Wang and Xu (2001) predicted a significant decrease in Co/Ca at each distance of flow, indicating that for speleothem-specific conditions, the theoretically predicted K_d value was insufficient to describe partitioning of Co into calcite. Deviations from the model-predicted Co/Ca values in the precipitate samples were observed, however these deviations were comparatively small. The discrepancies between model-predicted and experimental Co/Ca values are likely a result of at least two factors. Firstly, as precipitation occurs along the plate, the system moves away from equilibrium causing a change in K_d values as PCP progresses. Secondly, it is possible that competition for Ca^{2+} lattice sites between metals caused unexpected deviations from the model. This is supported by the observation that the increase in Co/Ca ratios in the precipitate samples occurred after Cu was lost from solution.

Ni/Ca ratios in solution samples taken during both inorganic experiments were also relatively well described by the predicted model based on **Equation 4.1** and the experimentally determined (static) partition coefficients. Again, the model employing the theoretical partition coefficient determined by Wang and Xu (2001)

predicted a significant decrease in Ni/Ca at each distance of flow, while the experimental data demonstrated fairly consistent Ni/Ca ratios along the length of the plate. As expected, the model based on a partition coefficient of 1, reported by Stipp and Lakshtanov (2007), also predicted the evolution of Ni/Ca relatively accurately. Deviations from model-predicted Ni/Ca ratios were again attributed to both K_d values changing with solution composition and competition for lattice sites with Co and Cu. The data for precipitate samples showed similar trends in Ni/Ca ratios to those observed for Co/Ca, with increases in Ni/Ca values observed as competing trace metals were lost from solution.

The evolution of Cu/Ca ratios during experiment 1 were notably different to the evolution of Co/Ca and Ni/Ca ratios. The high affinity of Cu^{2+} for the calcite lattice caused Cu/Ca ratios to drop steeply as PCP progressed, with concentrations of Cu in solution samples quickly dropping below the ICPMS quantification limit. Although the models presented in **Figure 4.5** capture this decrease, they deviate from the experimental data for both precipitate and solution samples, predicting an even faster loss of Cu from solution than was actually observed. Deviations from the model were assumed to be a result of the factors described above for Co/Ca and Ni/Ca. It can be seen from these results that using a single static partition coefficient to describe metal partitioning provides the best results for Co and Ni, likely indicating that this approach is most suitable for metals with low partition coefficients

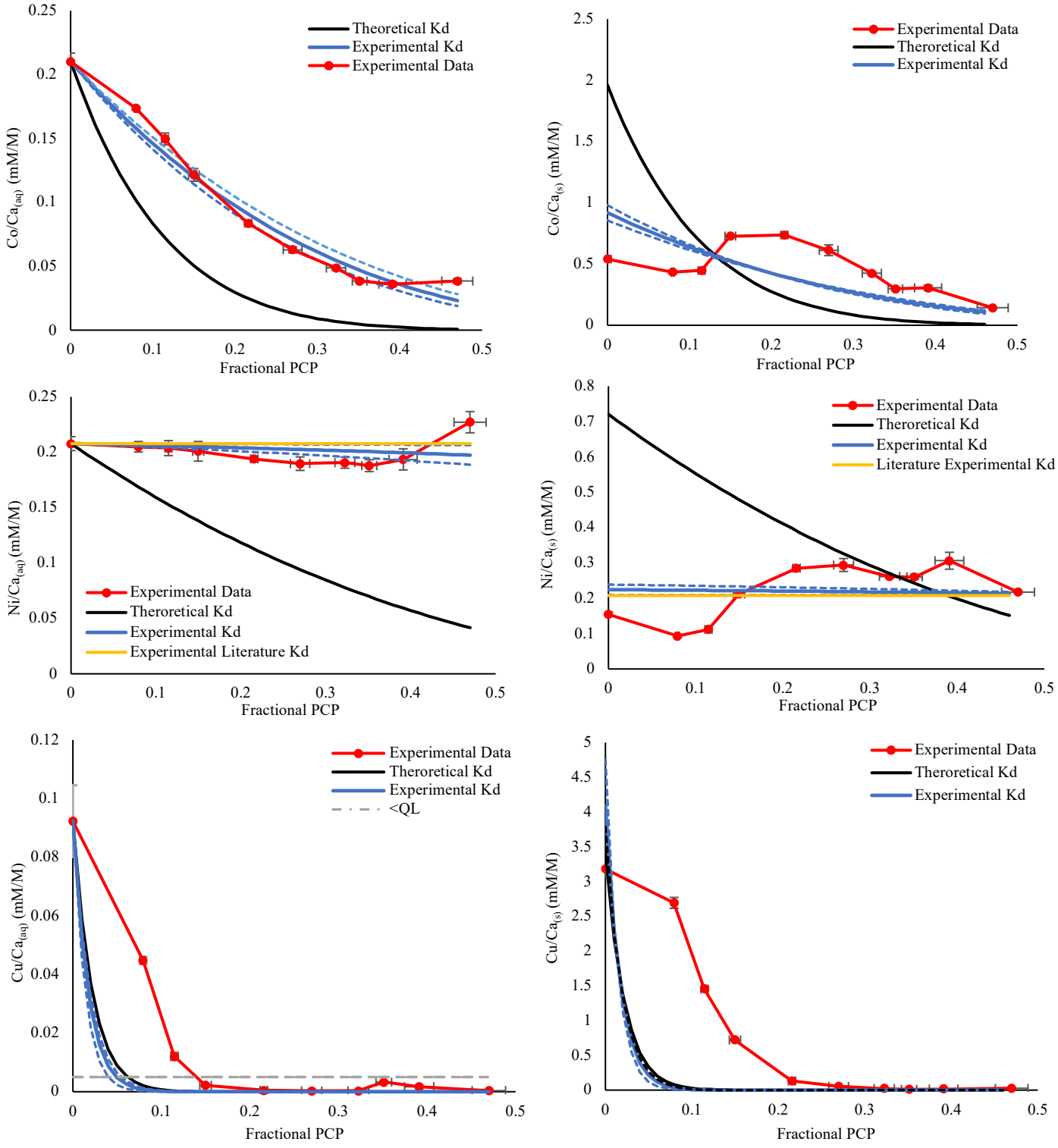

Figure 4.5. M/Ca ratios determined for solution and precipitate samples taken during experiment 1, with modelled M/Ca ratios based on both literature and average experimental K_d values. Black lines represent modelling undertaken with theoretical K_d values predicted by Wang and Xu (2001) using a linear free energy correlation approach,[48] while blue solid lines represent modelling based on the average experimental K_d values determined for each element over the entire plate. Blue dashed lines indicate error associated with the experimental K_d values. Yellow lines indicate modelling results based on the Ni partition coefficient determined for dilute solid solutions by Stipp and Lakshtanov (2007).[111] Data below dashed grey lines indicate the [M] was below the ICP-MS quantification limit.

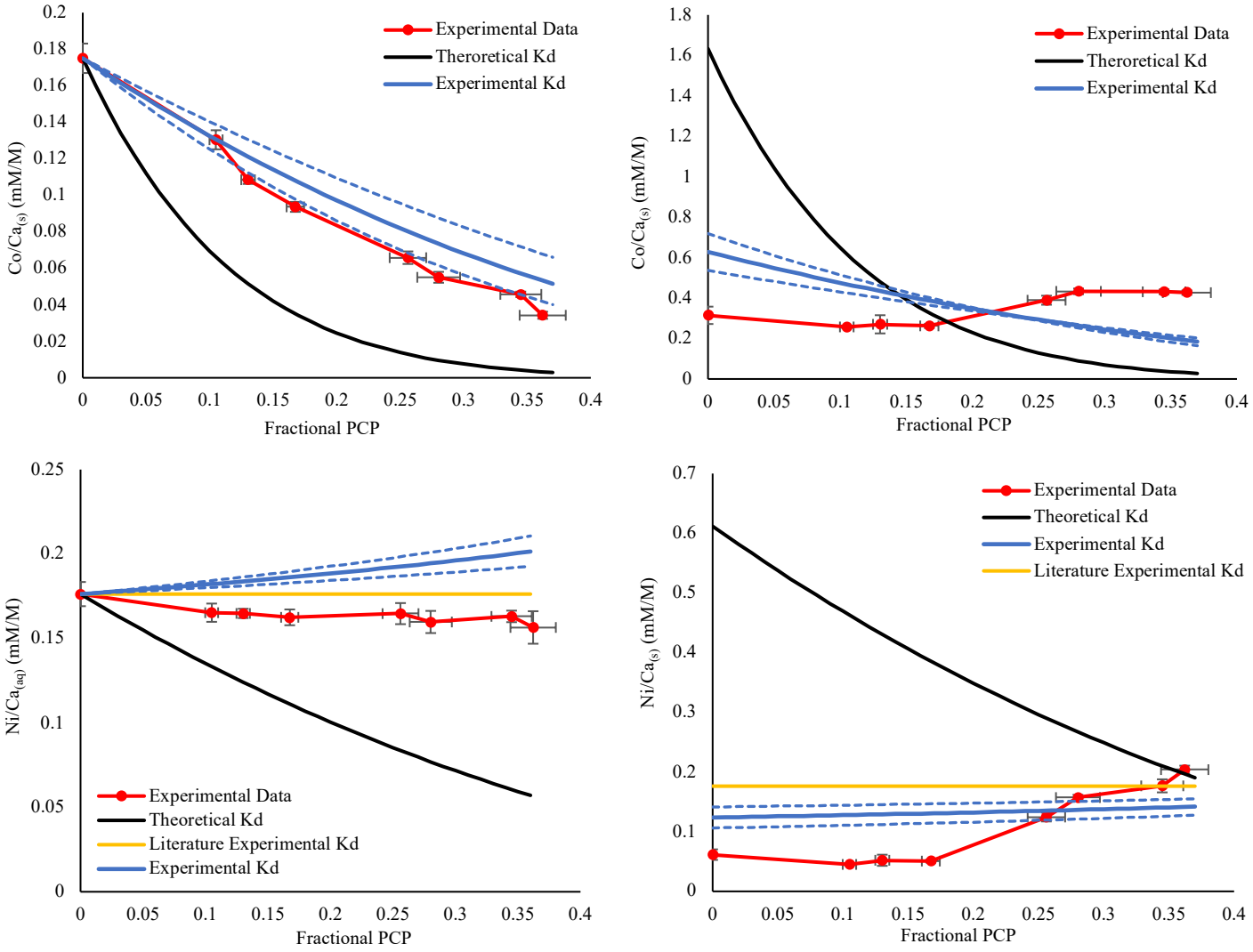

Figure 4.6. M/Ca ratios determined for solution and precipitate samples taken during experiment 2, with modelled M/Ca ratios based on both literature and average experimental K_d values. Black lines represent modelling undertaken with theoretical K_d values predicted by Wang and Xu (2001) using a linear free energy correlation approach, while blue solid lines represent modelling based on the average experimental K_d values determined for each element over the entire plate. Blue dashed lines indicate error associated with the experimental K_d values. Yellow lines indicate modelling results based on the Ni partition coefficient determined for dilute solid solutions by Stipp and Lakshtanov (2007).

It was mentioned above that K_d values for each element changed with solution composition and thus that a single, static, inorganic partition coefficient may be insufficient to fully describe partitioning behaviour of these elements over longer residence times. Therefore in order to determine whether a dynamic K_d value that changed with increasing PCP could better predict the M/Ca ratios observed in solution and precipitate samples, further modelling was undertaken. K_d values for each element were regressed against PCP (regressions presented in **Appendix II**),

and the resulting equations were used to calculate new K_d values for each step in the model. This modelling however (presented in **Appendix II**), did not provide a more accurate prediction of X/Ca ratios in solution and precipitate samples, indicating a simple linear relationship between K_d values and PCP was insufficient to describe the effect of changing solution composition on partitioning behaviour.

4.3.6 Organic Complexation and Trace Metal Partitioning

In order to assess the impact of complexation on partitioning of Co, Ni and Cu into calcite, M/Ca ratios in solution and precipitated calcite were determined for experiments 3 and 4 using the same method as described in **Section 4.3.5**. The ICP-MS results are presented in **Appendix II**. K_d values for each element at different distances of flow and the K_d value averaged over the entire plate for each element are presented in **Table 4.4**.

Table 4.4. Partition coefficients calculated during organic experiments 3 and 4.

Experiment 3 (NTA)					Experiment 4 (SRFA)			
Distance of Flow (cm)	PCP (%)	K_d			Distance of Flow (cm)	PCP (%)	K_d	
		Co	Ni	Cu			Cu	SRFA
5 ± 0.5	0	0.38 ± 0.03	0.06 ± 0.009	0.78 ± 0.07	-	-	-	-
9 ± 0.5	4.5 ± 0.3	0.36 ± 0.03	0.02 ± 0.005	0.78 ± 0.06	-	-	-	-
12 ± 0.5	7.4 ± 0.4	0.43 ± 0.04	0.08 ± 0.012	0.94 ± 0.1	-	-	-	-
17 ± 0.5	9.5 ± 0.8	0.46 ± 0.03	0.02 ± 0.005	1.01 ± 0.07	-	-	-	-
27 ± 0.5	13.5 ± 1.0	0.45 ± 0.04	0.02 ± 0.006	1.04 ± 0.11	-	-	-	-
37 ± 0.5	16.2 ± 1.2	0.47 ± 0.04	0.02 ± 0.006	1.09 ± 0.07	37 ± 0.5	10.5 ± 0.2	3.4 ± 0.1	-
47 ± 0.5	23.7 ± 1.9	0.39 ± 0.03	0.02 ± 0.004	0.93 ± 0.07	47 ± 0.5	12.3 ± 0.2	4.5 ± 0.1	0.44
57 ± 0.5	25.7 ± 2.1	0.35 ± 0.03	0.02 ± 0.006	0.88 ± 0.09	57 ± 0.5	11.4 ± 0.3	3.3 ± 0.4	0.35
67 ± 0.5	29.9 ± 1.6	0.34 ± 0.02	0.02 ± 0.007	0.85 ± 0.05	65 ± 0.5	11.9 ± 0.3	3.1 ± 0.4	0.34
89 ± 0.5	34.1 ± 3.3	0.35 ± 0.03	0.02 ± 0.006	0.83 ± 0.07	85 ± 0.5	16.5 ± 0.4	2.7 ± 0.1	-
Average K_d for entire plate:		**0.41 ± 0.03**	**0.029 ± 0.007**	**0.92 ± 0.08**	**Average K_d for entire plate:**		**3.3 ± 0.3**	**0.37**

It is evident that the presence of organic ligands in solution mediated the partitioning of all three metals into calcite. K_d values for each metal were significantly lower for experiments 3 and 4 than for the inorganic experiments,

indicating complexation by OM reduced the availability of 'free' metal ions for incorporation into the calcite lattice. These partition coefficients were therefore significantly closer to those observed by Hartland *et al.* (2014) in real cave systems. It should be noted that although a significant decrease in partition coefficients were observed, the order of partition coefficients determined for the inorganic experiments (Cu > Co > Ni) was preserved here.

Figures 4.7 and **4.8** show M/Ca ratios measured in solution and in precipitated $CaCO_3$ as PCP progressed for experiments 3 and 4 , respectively. No Cu/Ca data is presented for calcite precipitated in experiment 4 as low growth rates led to an insufficient amount of $CaCO_3$ for sampling at most distances of flow. Cu/Ca data in solution samples are, however, presented.

Modelling of expected M/Ca ratios as PCP progressed was also undertaken for experiments 3 and 4 (results presented in **Figures 4.7** and **4.8**). In order to do this the concentration of complexed metal was calculated for a range of residence times according to the first order rate law (**Equation 4.2**):[62]

$$[ML] = [ML]_i e^{-kt} \qquad (\mathbf{4.2})$$

where [ML] is the concentration of complexed ligand at time *t*, $[ML]_i$ is the initial concentration of complexed metal and *-k* is the dissociation rate constant. This allowed the amount of 'free' (i.e. uncomplexed) metal, f_m, to be calculated, and thus the partitioning of f_m as PCP occurred to be modelled according to **Equation 4.1**. Residence times were correlated to PCP via a linear regression for each experiment. Partitioning of metals was modelled using the averaged experimental inorganic K_d values determined in experiment 1 of this study (presented in **Table 4.3**). The first order dissociation rate constant used for modelling Ni dissociation from NTA (2 x 10^{-4} s^{-1}) was taken from Zhang *et al.* (2013), however no dissociation constants for CoNTA or CuNTA complexes could be found.[80] Therefore dissociation constants that provided a model with the best fit to the data (9.5 x 10^{-4} s^{-1} and 1.4 x 10^{-3} s^{-1} for Co and Cu respectively) were selected for these metals. Although these rate constants need to be verified, they provide a reasonable estimation of dissociation rate constants for the desired purpose. The rate constant used for modelling the

dissociation of CuSRFA complexes was 3.1 x 10^{-3} s^{-1}, based on the constant found by Chakraborty *et al.* (2013) for dissociation of Cu complexes with Suwannee River Natural Organic Matter (SRNOM).[112]

Solution data presented for the NTA experiment (experiment 4) show that the models and experimental results were in agreement (within error). A slow increase in Co/Ca and Ni/Ca in solution with progressing PCP was observed, in stark contrast to the inorganic results presented above. This indicates that for Co and Ni, complexation by NTA acts as a stronger 'sink' than the calcite lattice. $Cu/Ca_{(aq)}$ ratios demonstrated an initial decrease followed by an increase, as predicted by the model, but stayed fairly consistent along the plate with some slight variation around a mean of 0.135 mM/M. Again this is in stark contrast to the steep decrease observed for Cu in the inorganic system, and indicates that the calcite and organic ligand 'sinks' for Cu effectively balance each other in this scenario. So although Cu has a particularly high inorganic partition coefficient, the high stability of CuNTA complexes ensures that Cu is lost from solution at an almost constant rate.

Experiment 3 data presented for the precipitate samples were less well described by the model predictions. The models predict a slow increase in Co/Ca and Ni/Ca as PCP progresses, however experimental data shows Co/Ca and Ni/Ca stay fairly consistent along the plate, with some variation around mean values of 0.07 and 0.06 mM/M, respectively. A decrease in Cu/Ca was predicted by the model, which was consistent with the experimental data determined for the last half of the plate. However an initial increase in experimental Cu/Ca that was not captured by the model was observed at the start of the plate.

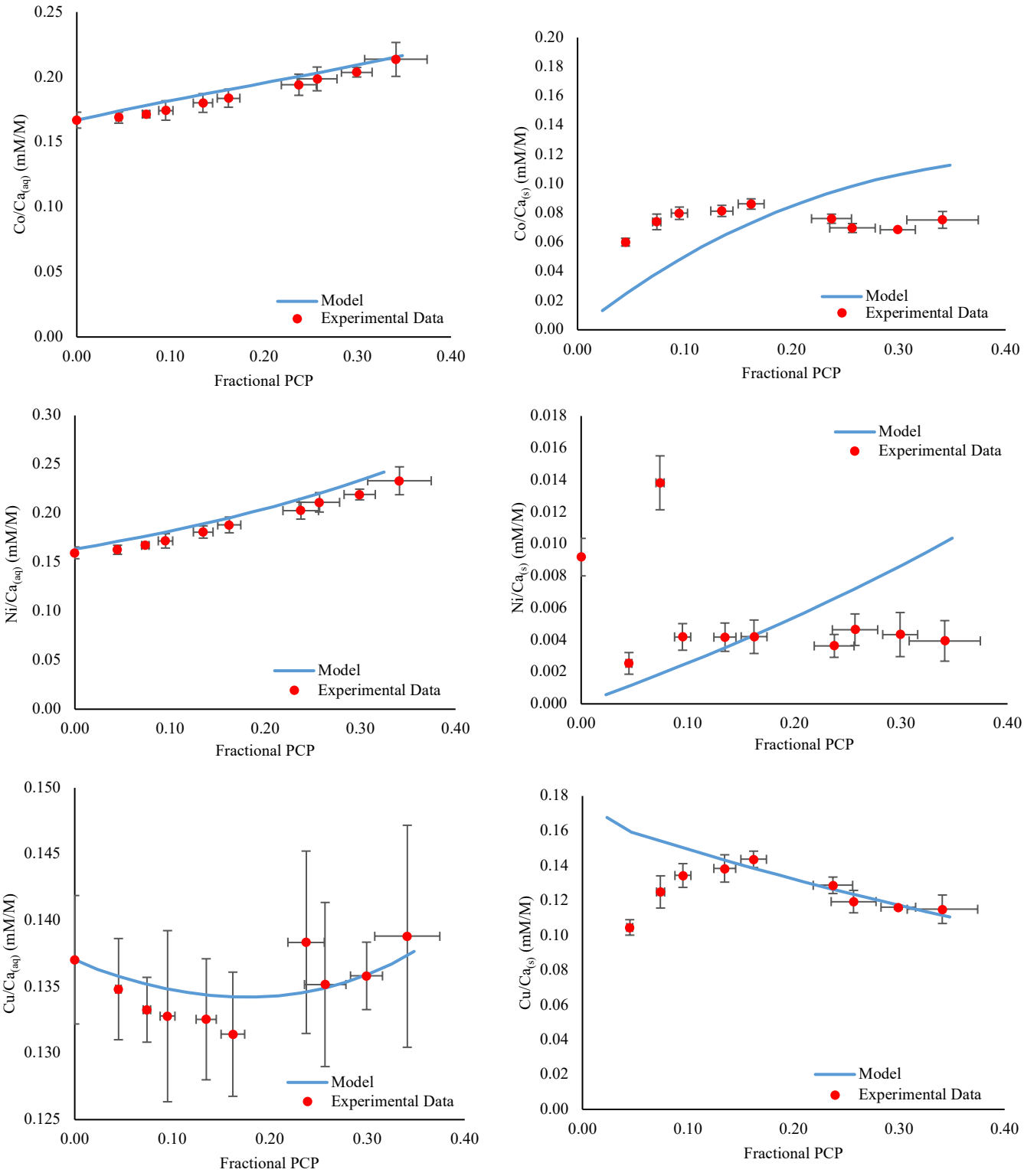

Figure 4.7. M/Ca ratios determined for solution and precipitate samples taken during experiment 3. Modelled M/Ca ratios are based on metal-NTA dissociation rates and average experimental inorganic K_d values determined for experiment 1.

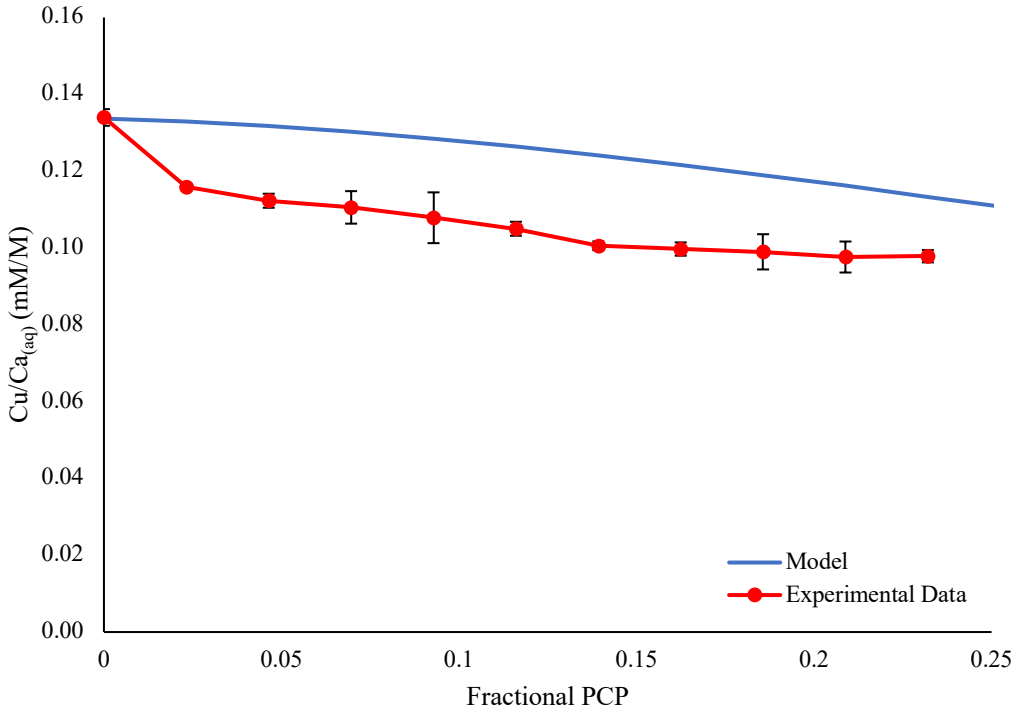

Figure 4.8. Cu/Ca ratios measured in solution samples during experiment 4. Modelled Cu/Ca ratios are based on Cu-SRNOM dissociation rates and the average experimental inorganic K_d value determined during experiment 1.

Deviations from predicted M/Ca ratios observed for experiment 3 may be explained by two major limitations of the modelling approach. Firstly, the dissociation constants used to predict the release of metal from organic complexes were constant across the entire plate. In reality however, it is unlikely the stability and dissociation rates of the complexes stayed the same as PCP progressed, because as the partitioning of trace metals into calcite occurred, it is likely there would also be a reduction in the M:NTA ratios in solution. This decrease in metal to ligand ratio would cause an increase in complex stability. Secondly, the effects of ternary complexation have not been accounted for in these models as the concentration of NTA in solution and precipitate samples was not assessed. However previous studies have shown that ternary complexation can play a role in trace element partitioning into speleothem calcite, particularly for highly stable complexes.[40] In order to assess whether the deviation from model predictions could realistically be a result of ternary complexation, the high values of $Ni/Ca_{(s)}$ observed at the start of the plate during experiment 3 were taken as an example. These deviation could be explained if ~0.18 % of the NiNTA complexes present in solution (equal to ~0.07 % of the total NTA species) were partitioning into the $CaCO_3$ via ternary

complexation. Previous studies have demonstrated that dissolved OM may indeed be incorporated into calcite to this degree, for instance Hartland et al (2014) reported a 3 % removal efficiency of organic carbon in the stalagmite PC-08-1 (Poole's Cavern, UK). It is therefore highly possible that ternary complexation may explain deviations in the $M/Ca_{(s)}$ for each trace metal.

Modelled results for the SRFA experiment predicted a slow decrease in $Cu/Ca_{(aq)}$ as PCP progressed, and this was observed in the experimental data. Again a stark contrast between the results observed for the inorganic experiment were seen, with complexation by SRFA causing a significant decrease in Cu partitioning. The $K_{d\ app}$ value determined for the SRFA experiment was 3.3 ± 0.3 compared to 0.92 ± 0.08 for the NTA experiment, indicative of faster dissociation rates for the CuSRFA complexes, as would be expected due to the high stability of complexes formed with the chelating ligand NTA. Discrepancies observed between the model and experimental results were likely due to the dissociation constant used, as faster dissociation rates gave similar results to those observed experimentally. The partitioning of SRFA into the calcite was assessed (see below) and it was found that ternary complexation could not account for the majority of the difference between modelled and observed results.

These experiments undertaken in the presence of organic ligands have reinforced the results observed in some speleothem-based studies; they have shown that complexation of the first-row transition metals Co, Ni and Cu by OM significantly alters their partitioning into calcite. Although the partitioning of Co, Ni and Cu can be predicted by K_d values alone in an inorganic system, this does not hold true for systems with organic ligand complexation, as dissociation of complexes to provide 'free' metal ions must first occur. Although the use of these metals as speleothem-based proxies has previously been overlooked in favour of metals with low inorganic K_d values, in reality the wide-spread presence of OM in karst systems will reduce the effects of PCP on these metals, and they should in fact be considered as useful additions to the current range paleo-proxies used. The results have highlighted that the signal of these metals in speleothems will be a controlled by the dissociation rates of the complexes, the residence time of the dripwaters and the

inorganic partition coefficients of the metal (i.e. the compatibility of the M^{2+} ions for lattice valence sites).

4.3.7 Partitioning of SRFA into Calcite

In order to assess the potential impact of ternary complexation on Cu partitioning into calcite, the concentration of SRFA in both solution and precipitate samples was assessed via 3D EEM fluorescence spectroscopy, and subsequent K_d values were calculated according to **Equation 4.3** (**Table 4.5).** Results indicated SRFA was being incorporated into precipitated calcite at a putative OM removal efficiency of 37 %. This was consistent with the observation that calcite precipitated during experiment 4 was significantly darker in colour compared to calcite precipitated during previous experiments, and indeed the brown colour observed in some speleothem calcite is known to be associated with high concentrations of OM.[13, 37, 91 113-114]

$$K_{d\ SRFA} = \frac{(SRFA/Ca)_s}{(SRFA/Ca)_{aq}} \quad \textbf{(4.3)}$$

The $K_{d\ SRFA}$ values determined here (average of 0.37) were consistent with the range of $K_{d\ NOM}$ values reported in the literature. Pearson *et al.* (2020) for instance observed values in the range of 2.8 to 4.3 during their crystal growth study where water from a peatland was used as the source of DOM. Hartland *et al.* (2014) observed average $K_{d\ NOM}$ values of 0.03 for samples taken from Pooles' Cavern, UK.[40] The incorporation of SRFA into calcite indicated that ternary complexation may be responsible to some degree for Cu partitioning into calcite, therefore the partitioning of SRFA-Cu complexes was assessed using **Equation 4.4**:[40]

$$K_{d\ SRFA-Cu} = \frac{(Cu/SRFA)_s}{(Cu/SRFA)_{aq}} \quad \textbf{(4.4)}$$

Table 4.5 SRFA concentrations in solution and precipitate samples taken from varying distances of flow during experiment 4, and associated partition coefficients.

Distance (cm)	PCP (%)	[SRFA] in Solution (ppm)	[SRFA] in Precipitate (mg/g)	$K_{d\ SRFA}$	$K_{d\ SRFA\text{-}Cu}$
0 ± 0.5	0.0	23.3	-	-	-
3 ± 0.5	2.7 ± 0.04	23.7	-	-	-
9 ± 0.5	5.0 ± 0.1	24.0	-	-	-
12 ± 0.5	3.9 ± 0.1	23.3	-	-	-
17 ± 0.5	1.9 ± 0.08	22.7	-	-	-
27 ± 0.5	8.9 ± 0.2	23.0	-	-	-
37 ± 0.5	10.5 ± 0.2	22.7	-	-	-
47 ± 0.5	12.3 ± 0.2	22.5	14	0.44	10.3
57 ± 0.5	11.4 ± 0.3	22.3	13	0.35	9.4
65 ± 0.5	11.9 ± 0.3	22.1	13	0.34	9.2
72 ± 0.5	-	-	12	-	-
78 ± 0.5	-	-	11	-	-
85 ± 0.5	16.5 ± 0.4	21.0	-	-	-
Average $K_{d\ SRFA}$ and $K_{d\ SRFA\text{-}Cu}$ for Entire Plate:				**0.37**	**9.7**

If ternary complexation was the dominant mechanism for Cu partitioning, $K_{d\ SRFA\text{-}Cu}$ values would be ≈1, as the metal to ligand ratio would remain constant in the solution and precipitate. This is a rare scenario for any complexed metal in karst systems, as ternary complexation is limited by the slower diffusion of NOM–M complexes relative to inorganic species, and by other complicated reaction mechanisms (e.g. steric and electrostatic effects and hydrophobic interactions between ligands).[115] However it has been observed for Co-NOM complexes in a hyperalkaline cave environment, due to the increased stability of Co complexes at high pH ensuring a significant decrease in dissociation rate. The average $K_{d\ SRFA\text{-}Cu}$ calculated during this study (**Table 4.5**) was 9.7, indicating the ratio of Cu to SRFA in the solid was higher than in the solution, and that the dissociation kinetics of Cu-SRFA complexes rather than ternary complexation was the main factor in determining Cu availability for incorporation into calcite.

4.3.8 Experimental Limitations and Future Work

This study suffered from several limitations that do not reflect natural cave environments. Notably, concentrations of trace elements significantly higher than those observed in a natural system were employed. Although this was necessary in order to ensure sufficient concentrations for isotope analysis, it is possible that effects that would otherwise not be observed in a natural system (e.g. competition between trace metals for lattice binding sites) affected the results of these experiments.

Although vaterite crystals have been identified as one of the many possible initial states of speleothem crystallization,[110] it is possible that the formation of vaterite during experiments 1-3 altered the partitioning behaviour of Co, Ni and Cu to some degree. Little data is available in the literature on the partitioning behaviour of trace elements into vaterite, and therefore further work in this area is required to assess whether partitioning behaviour into vaterite and calcite differs markedly.

Another significant limitation of this work is the lack of NTA concentration data for solution and precipitate samples from experiment 3. If this data were available, the extent of ternary complexation on the partitioning of Co, Ni and Cu into calcite could be properly assessed. Several analytical techniques including UV-visible spectroscopy, 3D EEM fluorescence spectroscopy and Liquid Chromatography Mass Spectrometry (LC-MS) were trialled in an attempt to provide this data, however the low concentrations of NTA coupled with matrix interferences observed for LC-MS due to high [Ca^{2+}] meant that NTA concentrations could not be reliably assessed. If further work on these samples were to be carried out, development of the Gas Chromatography Mass Spectrometry (GC-MS) method proposed by Reichert and Linckens (1980) to measure NTA to 1ppb concentrations in river water samples would be carried out.

In order for more accurate modelling of the partitioning of Co and Cu into calcite in the presence of NTA to be undertaken, dissociation rate constants for CoNTA and CuNTA complexes are required. Although the modelling undertaken here effectively used the data to solve for the dissociation rate constant, confirmation

that these values are in the expected range would be a valuable verification of the results.

Finally, assessment of the isotopic fractionation of Cu in each of the experiments would be a valuable addition to the literature. Schott *et al.* (2014) found that for metals where $K_d > 1$, precipitated calcite is enriched in heavier isotopes of the trace metal due to the affinity of these metals for the solid.[52] Thus, it would be expected for the inorganic experiments that the precipitate would be enriched in ^{65}Cu compared to the solution. However it is unlikely this would be observed for the organic experiments because, as mentioned in **Chapter 1**, it has been demonstrated that the organo-complexation of Cu can significantly alter the isotopic ratio of 'free' aqueous Cu species. For example Bigalke *et. al* (2010) reported that the fractionation at equilibrium between the 'free' Cu and the Cu bound to insoluble humic acid was 0.26 ± 0.11 ‰.[67] Ryan *et. al* (2014) also investigated the degree of isotopic fractionation of Cu during complexation with various soluble ligands and found an enrichment of ^{65}Cu in the complexes compared to the 'free' Cu species, with $\Delta^{65}Cu_{complex\text{-}free}$ values ranging from +0.14 to + 0.84 ‰.[68] It follows therefore that Cu precipitated in the organic experiments may demonstrate the opposite trend to that observed for the inorganic experiments. This effect is likely to be pronounced for Cu due to the high stability of Cu complexes (according to the Irvin-Williams series).[66] Indeed, Schott *et al.* (2014) calculated that complexation of Cu by very low concentrations of oxalate ligands would be sufficient to ensure calcite was enriched in light Cu instead of heavy Cu. It would be interesting therefore to investigate the degree of fractionation observed in the presence of stronger binding organic ligands more representative of karst-derived NOM (such as SRFA), so as to help with the interpretation of Cu isotope signals present in speleothem samples.

4.4 Conclusions

The partitioning behaviour of Co, Ni and Cu into calcite grown under speleothem-like conditions was assessed, and speleothem-specific K_d values of ~ 4, 1 and 44, respectively, were determined. Their partitioning as precipitation progressed was found to be predictable for the most part using the experimentally determined K_d

values, when no organic ligands were present in solution. These relatively high inorganic K_d values illustrate the reason why these divalent metals have frequently been overlooked as paleoclimate proxies in speleothems: metals with high partition coefficients are thought to exhibit complex partitioning behaviour and are significantly affected by PCP. However, further experiments illustrated that the complexation of Co, Ni and Cu significantly altered their partitioning behaviour, with apparent partition coefficients ($K_{d\ app}$) reduced below 1 for all three metals. It was shown that partitioning of Co, Ni and Cu into calcite was controlled by dissociation of the metal-ligand complexes, and thus that the amount of 'free' metal available for incorporation into calcite was dependent on residence time and the dissociation constants of the complexes.

This study highlights the fact that the incorporation of the divalent first-row metals into speleothem calcite cannot not be considered in terms of simple inorganic partitioning, as the widespread presence of NOM in karst systems will alter their partitioning behaviour significantly. Thus, although the use of these metals as speleothem-based proxies has previously been overlooked in favour of elements such as the alkali earth metals which exhibit simple partitioning (i.e. $K_d << 1$), in reality the NOM present in karst systems will reduce the effects of PCP on these divalent first-row metals, and they should in fact be considered as useful additions to the current range of paleo-proxies used.

It has been shown that the signal of the divalent first-row transition metals Co, Ni and Cu in speleothems will be a controlled by i) the dissociation rates of the complexes ii) the residence time of the dripwaters and iii) the inorganic partition coefficients of the metal, and therefore that their partitioning into speleothem calcite may be predictable.

5 Conclusions

To date, trace element proxies in speleothem archives have primarily been limited to elements that exhibit simple partitioning into calcite, namely the alkali earth metals. The high inorganic partition coefficients reported for transition metals have ensured little attention has been given to these elements, as it has been assumed that prior calcite precipitation (PCP) would significantly affect the signals of these elements in speleothems. However recent studies have suggested that first-row transition metals may indeed be useful additions to the current suite of trace element proxies already utilised, due to the complexation of these metals by natural organic matter (NOM) in karst systems. It has been suggested that complexation of first-row transition metals by NOM may alter their partitioning behaviour into speleothem calcite and reduce the effects of PCP on these metals. This study therefore aimed to assess the degree to which complexation of Co, Ni and Cu by organic ligands affected their partition behaviour into calcite grown under karst analogue conditions, and thus to help establish whether these metals may be viable speleothem-based proxies for paleoclimate reconstructions.

A method for growing speleothem-like calcite that allowed investigation of the partitioning behaviour of trace elements was first developed. A purpose-built chamber allowing precise control of temperature, humidity and pCO_2 ensured consistent environmental conditions throughout the crystal growth experiments. Calcite was grown in a manner analogous to that observed for natural speleothems, with calcite precipitation occurring as a result of CO_2 degassing from a thin solution film. Calculated growth rates for the method were consistent with growth rates reported in the literature for similar cave-analogue studies and structural characterisation of the $CaCO_3$ crystals confirmed the precipitate was predominantly calcite (and thus representative of speleothem $CaCO_3$ deposits). The method developed was therefore considered to be suitable for the desired purpose, and the partitioning data obtained subsequently was considered to be applicable to 'real-world' speleothem samples.

The partitioning of Co, Ni and Cu into calcite in the absence of organic ligands was assessed and speleothem-specific K_d values of ~ 4, 1 and 44, respectively, were determined. The high inorganic K_d values determined for Co and Cu illustrate the reason why these divalent metals have frequently been overlooked as paleoclimate proxies in speleothems: metals with high partition coefficients are thought to exhibit complex partitioning behaviour and are significantly affected by PCP. However, further experiments were undertaken to assess the partitioning behaviour of these metals when organic ligands were present in solution, and it was found that complexation of Co, Ni and Cu by nitrilotriacetic acid (NTA) and complexation of Cu by Suwanee River fulvic acid (SRFA) significantly altered the partitioning behaviour of the metals, with apparent partition coefficients reduced below 1 in all cases.

The results of this study therefore reinforce the notion that partitioning of first-row transition metals into speleothems is controlled to a significant degree by complexation with NOM in karst systems, and cannot be considered in terms of simple inorganic partitioning. The results also demonstrated that partitioning of Co, Ni and Cu into speleothems may be predictable, as the extent of their incorporation into calcite is dependent primarily on three factors: the residence time of the dripwaters, the dissociations rates of metal-NOM complexes and the speleothem-specific inorganic partition coefficients.

Overall, this study indicated that Co, Ni and Cu may indeed be viable paleoclimate proxies in speleothems. Their use in a multi-proxy approach for paleoclimate reconstructions may help speleothem scientists worldwide to interpret their records with a higher degree of certainty and provide information on past climatic events that could help us to better understand our current and changing climate.

References

1. Fairchild, I. J.; Baker, A., *Speleothem Science : From Process to Past Environments*. Wiley: Hoboken, UK, 2012.

2. Hendy, C. H., The isotopic geochemistry of speleothems - I. The calculation of the effects of different modes of formation on the isotopic composition of speleothems and their applicability as palaeoclimatic indicators. *Geochimica et Cosmochimica Acta* **1971,** *35* (8), 801-824.

3. Casteel, R. C.; Banner, J. L., Temperature-driven seasonal calcite growth and drip water trace element variations in a well-ventilated Texas cave: Implications for speleothem paleoclimate studies. *Chemical Geology* **2015,** *392*, 43-58.

4. Fairchild, I. J.; Borsato, A.; Tooth, A. F.; Frisia, S.; Hawkesworth, C. J.; Huang, Y.; McDermott, F.; Spiro, B., Controls on trace element (Sr-Mg) compositions of carbonate cave waters: implications for speleothem climatic records. *Chemical Geology* **2000,** *166* (3), 255-269.

5. Fairchild, I. J.; Treble, P. C., Trace elements in speleothems as recorders of environmental change. *Quaternary Science Reviews* **2009,** *28* (5), 449-468.

6. Gascoyne, M., Trace-element partition coefficients in the calcite-water system and their paleoclimatic significance in cave studies. *Journal of Hydrology* **1983,** *61* (1), 213-222.

7. Owen, R. A.; Day, C. C.; Hu, C. Y.; Liu, Y. H.; Pointing, M. D.; Blättler, C. L.; Henderson, G. M., Calcium isotopes in caves as a proxy for aridity: Modern calibration and application to the 8.2 kyr event. *Earth and Planetary Science Letters* **2016,** *443*, 129-138.

8. Phillips, B. L.; Zhang, Z.; Kubista, L.; Frisia, S.; Borsato, A., NMR spectroscopic study of organic phosphate esters coprecipitated with calcite. *Geochimica et Cosmochimica Acta* **2016,** *183*, 46-62.

9. Nagra, G.; Treble, P. C.; Andersen, M. S.; Fairchild, I. J.; Coleborn, K.; Baker, A., A post-wildfire response in cave dripwater chemistry. *Hydrology and Earth System Sciences* **2016,** *20* (7), 2745-2758.

10. Moreno, A.; Stoll, H.; Jiménez-Sánchez, M.; Cacho, I.; Valero-Garcés, B.; Ito, E.; Edwards, R. L., A speleothem record of glacial (25–11.6kyr BP) rapid

climatic changes from northern Iberian Peninsula. *Global and Planetary Change* **2010,** *71* (3), 218-231.

11. Shen, C.; Lin, K.; Duan, W.; Jiang, X.; Partin, J. W.; Edwards, R. L.; Cheng, H.; Tan, M., Testing the annual nature of speleothem banding. *Scientific Reports* **2013,** *3*, 2633.

12. Hartland, A.; Fairchild, I. J.; Lead, J. R.; Borsato, A.; Baker, A.; Frisia, S.; Baalousha, M., From soil to cave: Transport of trace metals by natural organic matter in karst dripwaters. *Chemical Geology* **2012,** *304-305*, 68-82.

13. Blyth, A. J.; Hartland, A.; Baker, A., Organic proxies in speleothems – New developments, advantages and limitations. *Quaternary Science Reviews* **2016,** *149*, 1-17.

14. Hartland, A.; Hu, C.; Enge, G.; Zitoun, R.; Lehto, N.; Salmanzadeh, M.; Fox, B.; Dosseto, A.; Breitenbach, S. F. M., Towards a quantitative proxy of cave dripwater hydrology. In *European Geosciences Union*, Vienna, Austria, 2018.

15. Markowska, M.; Baker, A.; Treble, P. C.; Andersen, M. S.; Hankin, S.; Jex, C. N.; Tadros, C. V.; Roach, R., Unsaturated zone hydrology and cave drip discharge water response: Implications for speleothem paleoclimate record variability. *Journal of Hydrology* **2015,** *529*, 662-675.

16. Williams, P. W., The role of the epikarst in karst and cave hydrogeology: a review. *International Journal of Speleology* **2008,** *37*, 1-10.

17. Poulain, A.; Watlet, A.; Kaufmann, O.; Van Camp, M.; Jourde, H.; Mazzilli, N.; Rochez, G.; Deleu, R.; Quinif, Y.; Hallet, V., Assessment of groundwater recharge processes through karst vadose zone by cave percolation monitoring. *Hydrological Processes* **2018,** *32* (13), 2069-2083.

18. Hansen, M.; Dreybrodt, W.; Scholz, D., Chemical evolution of dissolved inorganic carbon species flowing in thin water films and its implications for (rapid) degassing of CO_2 during speleothem growth. *Geochimica et Cosmochimica Acta* **2013,** *107*, 242-251.

19. Hansen, M.; Scholz, D.; Froeschmann, M. L.; Schöne, B. R.; Spötl, C., Carbon isotope exchange between gaseous CO_2 and thin solution films: Artificial cave experiments and a complete diffusion-reaction model. *Geochimica et Cosmochimica Acta* **2017,** *211*, 28-47.

20. Hansen, M. Determination of the stable isotope fractionation $\delta^{18}O$ and $\delta^{13}C$ during precipitation of speleothem calcite: Novel cave analogue laboratory experiments. PhD, Johannes-Gutenberg University, Mainz, Germany, 2017.

21. Dreybrodt, W.; Hansen, M.; Scholz, D., Processes affecting the stable isotope composition of calcite during precipitation on the surface of stalagmites: Laboratory experiments investigating the isotope exchange between DIC in the solution layer on top of a speleothem and the CO_2 of the cave atmosphere. *Geochimica et Cosmochimica Acta* **2016,** *174*, 247-262.

22. Dreybrodt, W.; Eisenlohr, L.; Madry, B.; Ringer, S., Precipitation kinetics of calcite in the system $CaCO_3$ - H_2O - CO_2: The conversion to CO_2 by the slow process $H^+ + HCO_3^- \rightarrow CO_2 + H_2O$ as a rate limiting step. *Geochimica et Cosmochimica Acta* **1997,** *61* (18), 3897-3904.

23. Romanov, D.; Kaufmann, G.; Dreybrodt, W., Modeling stalagmite growth by first principles of chemistry and physics of calcite precipitation. *Geochimica et Cosmochimica Acta* **2008,** *72* (2), 423-437.

24. Mühlinghaus, C.; Scholz, D.; Mangini, A., Modelling stalagmite growth and $\delta^{13}C$ as a function of drip interval and temperature. *Geochimica et Cosmochimica Acta* **2007,** *71* (11), 2780-2790.

25. Plummer, L. N.; Wigley, T. M. L.; Parkhurst, D. L., The kinetics of calcite dissolution in CO_2 -water systems at 5 degrees to 60 degrees C and 0.0 to 1.0 atm CO_2. *American Journal of Science* **1978,** *278* (2), 179-216.

26. Buhmann, D.; Dreybrodt, W., The kinetics of calcite dissolution and precipitation in geologically relevant situations of karst areas: 1. Open system. *Chemical Geology* **1985,** *48* (1), 189-211.

27. Baker, A.; Genty, D.; Dreybrodt, W.; Barnes, W. L.; Mockler, N. J.; Grapes, J., Testing theoretically predicted stalagmite growth rate with recent annually laminated samples: Implications for past stalagmite deposition. *Geochimica et Cosmochimica Acta* **1998,** *62* (3), 393-404.

28. Hori, M.; Ishikawa, T.; Nagaishi, K.; Lin, K.; Wang, B. S.; You, C. F.; Shen, C. C.; Kano, A., Prior calcite precipitation and source mixing process influence Sr/Ca, Ba/Ca and $^{87}Sr/^{86}Sr$ of a stalagmite developed in southwestern Japan during 18.0 - 4.5ka. *Chemical Geology* **2013,** *347*, 190-198.

29. Hoefs, J., *Stable Isotope Geochemistry*. Springer Berlin Heidelberg: Berlin/Heidelberg, Germany, 2009.

30. Hansen, M. Determination of the stable isotope fractionation $\delta^{18}O$ and $\delta^{13}C$ during precipitation of speleothem calcite: Novel cave analogue laboratory experiments. Johannes-Gutenberg University, Mainz, Germany, 2017.

31. Cross, M.; McGee, D.; Broecker, W. S.; Quade, J.; Shakun, J. D.; Cheng, H.; Lu, Y.; Edwards, R. L., Great Basin hydrology, paleoclimate, and connections

with the North Atlantic: A speleothem stable isotope and trace element record from Lehman Caves, NV. *Quaternary Science Reviews* **2015,** *127*, 186-198.

32. Liu, Y. H.; Henderson, G. M.; Hu, C. Y.; Mason, A. J.; Charnley, N.; Johnson, K. R.; Xie, S. C., Links between the East Asian monsoon and North Atlantic climate during the 8,200 year event. *Nature Geoscience* **2013,** *6*, 117.

33. Baker, A.; Ito, E.; Smart, P. L.; McEwan, R. F., Elevated and variable values of ^{13}C in speleothems in a British cave system. *Chemical Geology* **1997,** *136* (3), 263-270.

34. Cumberland, S. A.; Baker, A., The freshwater dissolved organic matter fluorescence–total organic carbon relationship. *Hydrological Processes* **2007,** *21* (16), 2093-2099.

35. Blyth, A. J.; Smith, C. I.; Drysdale, R. N., A new perspective on the $\delta^{13}C$ signal preserved in speleothems using LC–IRMS analysis of bulk organic matter and compound specific stable isotope analysis. *Quaternary Science Reviews* **2013,** *75*, 143-149.

36. Hartland, A.; Fairchild, I. J.; Lead, J. R.; Zhang, H.; Baalousha, M., Size, speciation and lability of NOM–metal complexes in hyperalkaline cave dripwater. *Geochimica et Cosmochimica Acta* **2011,** *75* (23), 7533-7551.

37. Blyth, A. J.; Asrat, A.; Baker, A.; Gulliver, P.; Leng, M. J.; Genty, D., A new approach to detecting vegetation and land-use change using high-resolution lipid biomarker records in stalagmites. *Quaternary Research* **2007,** *68* (3), 314-324.

38. McPhie, P., Principles of Fluorescence Spectroscopy, Second ed. Joseph R. Lakowicz. *Analytical Biochemistry* **2000,** *287* (2), 353-354.

39. Allan, M.; Fagel, N.; Van Rampelbergh, M.; Baldini, J.; Riotte, J.; Cheng, H.; Edwards, R. L.; Gillikin, D.; Quinif, Y.; Verheyden, S., Lead concentrations and isotope ratios in speleothems as proxies for atmospheric metal pollution since the industrial revolution. *Chemical Geology* **2015,** *401*, 140-150.

40. Hartland, A.; Fairchild, I. J.; Müller, W.; Dominguez-Villar, D., Preservation of NOM-metal complexes in a modern hyperalkaline stalagmite: Implications for speleothem trace element geochemistry. *Geochimica et Cosmochimica Acta* **2014,** *128*, 29-43.

41. McIntire, W. L., Trace element partition coefficients - A review of theory and applications to geology. *Geochimica et Cosmochimica Acta* **1963,** *27* (12), 1209-1264.

42. Paquette, J.; Reeder, R. J., Relationship between surface structure, growth mechanism, and trace element incorporation in calcite. *Geochimica et Cosmochimica Acta* **1995,** *59* (4), 735-749.

43. Morse, J. W.; Bender, M. L., Partition coefficients in calcite: Examination of factors influencing the validity of experimental results and their application to natural systems. *Chemical Geology* **1990,** *82*, 265-277.

44. Henderson, L. M.; Kracek, F. C., The fractional precipitation of barium and radium chromates. *Journal of the American Chemical Society* **1927,** *49* (3), 738-749.

45. Tremaine, D. M.; Froelich, P. N., Speleothem trace element signatures: A hydrologic geochemical study of modern cave dripwaters and farmed calcite. *Geochimica et Cosmochimica Acta* **2013,** *121*, 522-545.

46. Rimstidt, J. D.; Balog, A.; Webb, J., Distribution of trace elements between carbonate minerals and aqueous solutions. *Geochimica et Cosmochimica Acta* **1998,** *62* (11), 1851-1863.

47. Lorens, R. B., Sr, Cd, Mn and Co distribution coefficients in calcite as a function of calcite precipitation rate. *Geochimica et Cosmochimica Acta* **1981,** *45* (4), 553-561.

48. Wang, Y.; Xu, H., Prediction of trace metal partitioning between minerals and aqueous solutions: A linear free energy correlation approach. *Geochimica et Cosmochimica Acta* **2001,** *65* (10), 1529-1543.

49. Staudt, W. J.; Reeder, R. J.; Schoonen, M. A. A., Surface structural controls on compositional zoning of SO_2^{4-} and SeO_2^{4-} in synthetic calcite single crystals. *Geochimica et Cosmochimica Acta* **1994,** *58* (9), 2087-2098.

50. Reeder, R. J.; Nugent, M.; Lamble, G. M.; Tait, C. D.; Morris, D. E., Uranyl incorporation into calcite and aragonite: XAFS and luminescence studies. *Environmental Science & Technology* **2000,** *34* (4), 638-644.

51. Day, C. C.; Henderson, G. M., Controls on trace-element partitioning in cave-analogue calcite. *Geochimica et Cosmochimica Acta* **2013,** *120*, 612-627.

52. Schott, J.; Mavromatis, V.; González-González, A.; Oelkers, E. H., Kinetic and thermodynamic controls of divalent metals isotope composition in carbonate: Experimental investigations and applications. *Procedia Earth and Planetary Science* **2014,** *10*, 168-172.

53. Zhou, H.; Wang, Y.; Huang, L.; Mai, S., Speleothem Mg, Sr and Ba records during the MIS 5c-d, and implications for paleoclimate change in NE Sichuan, Central China. *Chinese Science Bulletin* **2011,** *56* (32), 3445-3450.

54. Fairchild, I. J.; McMillan, E. A., Speleothems as indicators of wet and dry periods. *International Journal of Speleology* **2007,** *36* (2), 69-74.

55. Sinclair, D. J., Two mathematical models of Mg and Sr partitioning into solution during incongruent calcite dissolution: Implications for dripwater and speleothem studies. *Chemical Geology* **2011,** *283* (3), 119-133.

56. Borsato, A.; Frisia, S.; Fairchild, I. J.; Somogyi, A.; Susini, J., Trace element distribution in annual stalagmite laminae mapped by micrometer-resolution X-ray fluorescence: Implications for incorporation of environmentally significant species. *Geochimica et Cosmochimica Acta* **2007,** *71* (6), 1494-1512.

57. Tipping, E.; Campbell, P. G. C.; Harrison, R. M., *Cation Binding by Humic Substances*. Cambridge University Press: Cambridge, UK, 2002.

58. Gaffney, J. S.; Marley, N. A.; Clark, S. B., Humic and fulvic acids and organic colloidal materials in the environment. In *Humic and Fulvic Acids*, American Chemical Society: 1996; Vol. 651, pp 2-16.

59. Motuzova, G. V.; Makarichev, I. P.; Dergham, H. M.; Stepanov, A. A.; Barsova, N. U., *Soil Organic Matter and Its Interactions with Metals: Processes, Factors, Ecological Significance*. Nova Science Publishers, Incorporated: Hauppauge, US, 2012.

60. Tipping, E.; Hurley, M. A., A unifying model of cation binding by humic substances. *Geochimica et Cosmochimica Acta* **1992,** *56* (10), 3627-3641.

61. Hartland, A.; Zitoun, R., Transition metal availability to speleothems controlled by organic binding ligands. *Geochemical Perspectives Letters* **2018,** *8*, 22-25.

62. Amery, F.; Degryse, F.; Van Moorleghem, C.; Duyck, M.; Smolders, E., The dissociation kinetics of Cu-dissolved organic matter complexes from soil and soil amendments. *Analytica Chimica Acta* **2010,** *670* (1), 24-32.

63. Eigen, M.; Wilkins, R. G., The kinetics and mechanism of formation of metal complexes. In *Mechanisms of Inorganic Reactions, Advances in Chemistry*, Gould, R. F., Ed. American Chemical Society: Washington, DC, 1965.

64. Mandal, R.; L.R. Sekaly, A.; Murimboh, J.; Hassan, N. M.; Chakrabarti, C. L.; Back, M. H.; Grégoire, D. C.; Schroeder, W. H., Effect of the competition of copper and cobalt on the lability of Ni(II)–organic ligand complexes, Part II: In freshwaters (Rideau River surface waters). *Analytica Chimica Acta* **1999,** *395* (3), 323-334.

65. Shi, Z.; Wang, P.; Peng, L.; Lin, Z.; Dang, Z., Kinetics of heavy metal dissociation from natural organic matter: Roles of the carboxylic and phenolic sites. *Environmental Science & Technology* **2016,** *50* (19), 10476-10484.

66. Irving, H.; Williams, R. J. P., Order of stability of metal complexes. *Nature* **1948,** *162* (4123), 746-747.

67. Bigalke, M.; Weyer, S.; Wilcke, W., Copper isotope fractionation during complexation with insolubilized humic acid. *Environmental Science & Technology* **2010,** *44* (14), 5496-5502.

68. Ryan, B. M.; Kirby, J. K.; Degryse, F.; Scheiderich, K.; McLaughlin, M. J., Copper isotope fractionation during equilibration with natural and synthetic ligands. *Environmental Science & Technology* **2014,** *48* (15), 8620-8626.

69. Jahn, H. A.; Teller, E., Stability of polyatomic molecules in degenerate electronic states - I: Orbital degeneracy. *Proceedings of the Royal Society of London. Series A - Mathematical and Physical Sciences* **1937,** *161* (905), 220-235.

70. Furia, T. E., Chapter 6: Sequestrants in food. In *Handbook of Food Additives*, 2 ed.; Furia, T. E., Ed. CRC Press: Washington, USA, 1972; Vol. 1, pp 274-278.

71. Goli, M. B.; Pande, M.; Bellaloui, N., Effects of chelating agents on protein, oil, fatty acids, and minerals in soybean seed. *Agricultural Sciences* **2012,** *3* (4), 7.

72. Glaus, M. A.; Hummel, W.; Van Loon, L. R., Trace metal–humate interactions. I. Experimental determination of conditional stability constants. *Applied Geochemistry* **2000,** *15* (7), 953-973.

73. Stumm, W.; Morgan, J. J., *Aquatic Chemistry : Chemical Equilibria and Rates in Natural Waters*. John Wiley & Sons, Incorporated: Somerset, USA, 1995.

74. Town, R. M.; Filella, M., Crucial role of the detection window in metal ion speciation analysis in aquatic systems: The interplay of thermodynamic and kinetic factors as exemplified by nickel and cobalt. *Analytica Chimica Acta* **2002,** *466* (2), 285-293.

75. Warnken, K. W.; Davison, W.; Zhang, H.; Galceran, J.; Puy, J., In situ measurements of metal complex exchange kinetics in freshwater. *Environmental Science & Technology* **2007,** *41* (9), 3179-3185.

76. Wang, P.; Ding, Y.; Liu, M.; Liang, Y.; Shi, Z., Modeling kinetics of Ni dissociation from humic substances based on WHAM 7. *Chemosphere* **2019,** *221*, 254-262.

77. Rate, A. W.; McLaren, R. G.; Swift, R. S., Response of copper(II)-humic acid dissociation kinetics to factors influencing complex stability and

macromolecular conformation. *Environmental Science & Technology* **1993,** *27* (7), 1408-1414.

78. Cabaniss, S. E., pH and ionic strength effects on nickel-fulvic acid dissociation kinetics. *Environmental Science & Technology* **1990,** *24* (4), 583-588.

79. Lavigne, J. A.; Langford, C. H.; Mak, M. K. S., Kinetic study of speciation of nickel(II) bound to a fulvic acid. *Analytical Chemistry* **1987,** *59* (21), 2616-2620.

80. Zhang, H.; Shafaei Arvajeh, M. R.; Lehto, N.; Garmo, Ø. A., Kinetic studies of Ni organic complexes using Diffusive Gradients in Thin Films (DGT) with double binding layers and a dynamic numerical model. *Environmental Science & Technology* **2013,** *47* (1), 463-470.

81. Town, R. M., Metal binding by heterogeneous ligands: Kinetic master curves from SSCP waves. *Environmental Science & Technology* **2008,** *42* (11), 4014-4021.

82. Amery, F.; Degryse, F.; Cheyns, K.; De Troyer, I.; Mertens, J.; Merckx, R.; Smolders, E., The UV-absorbance of dissolved organic matter predicts the fivefold variation in its affinity for mobilizing Cu in an agricultural soil horizon. *European Journal of Soil Science* **2008,** *59* (6), 1087-1095.

83. Pokrovsky, O. S.; Viers, J.; Emnova, E. E.; Kompantseva, E. I.; Freydier, R., Copper isotope fractionation during its interaction with soil and aquatic microorganisms and metal oxy(hydr)oxides: Possible structural control. *Geochimica et Cosmochimica Acta* **2008,** *72* (7), 1742-1757.

84. Mavromatis, V.; Immenhauser, A.; Buhl, D.; Purgstaller, B.; Baldermann, A.; Dietzel, M., Effect of organic ligands on Mg partitioning and Mg isotope fractionation during low-temperature precipitation of calcite in the absence of growth rate effects. *Geochimica et Cosmochimica Acta* **2017,** *207*, 139-153.

85. Fujii, T.; Moynier, F.; Abe, M.; Keisuke, N.; Albarède, F., Copper isotope fractionation between aqueous compounds relevant to low temperature geochemistry and biology. *Geochimica et Cosmochimica Acta* **2013,** *110*, 29-44.

86. Huang, Y.; Fairchild, I. J., Partitioning of Sr^{2+} and Mg^{2+} into calcite under karst-analogue experimental conditions. *Geochimica et Cosmochimica Acta* **2001,** *65* (1), 47-62.

87. Parkhurst, D. L.; Apello, C., User's guide to PHREEQC version 2. *US Geological Survey* **1999,** *312*.

88. Dreybrodt, W.; Scholz, D., Climatic dependence of stable carbon and oxygen isotope signals recorded in speleothems: From soil water to speleothem calcite. *Geochimica et Cosmochimica Acta* **2011,** *75* (3), 734-752.

89. Allison, J. D.; Brown, D. S.; Novo-Gradac, K. J., *MINTEQA2/ PRODEFA2, A Geochemical Model for Environmental Systems: Version 3.0*. Office of Research and Development, U.S. Environmental Protection Agency: Washington, DC, 1991.

90. Ni, M.; Ratner, B. D., Differentiating calcium carbonate polymorphs by surface analysis techniques - an XPS and TOF-SIMS study. *Surface and Interface Analysis* **2008,** *40* (10), 1356-1361.

91. Pearson, A. R.; Hartland, A.; Frisia, S.; Fox, B. R. S., Formation of calcite in the presence of dissolved organic matter: Partitioning, fabrics and fluorescence. *Chemical Geology* **2020**, 119492.

92. Gilmore, A. M.; Cohen, S. M., Analysis of the chromophoric dissolved organic matter in water by EEMs with Horiba-Jobin Yvon fluorescence instrument called Aqualog. *Readout* **2013,** *41*, 19-24.

93. Andersson, C. A.; Bro, R., The N-way toolbox for MATLAB. *Chemometrics and intelligent laboratory systems* **2000,** *52* (1), 1-4.

94. Murphy, K. R.; Stedmon, C. A.; Graeber, D.; Bro, R., Fluorescence spectroscopy and multi-way techniques. PARAFAC. *Analytical Methods* **2013,** *5* (23), 6557-6566.

95. Fellman, J. B.; Hood, E.; Spencer, R. G. M., Fluorescence spectroscopy opens new windows into dissolved organic matter dynamics in freshwater ecosystems: A review. *Limnology and Oceanography* **2010,** *55* (6), 2452-2462.

96. Ishii, S. K. L.; Boyer, T. H., Behavior of reoccurring PARAFAC components in fluorescent dissolved organic matter in natural and engineered systems: A critical review. *Environmental Science & Technology* **2012,** *46* (4), 2006-2017.

97. Coble, P. G., Characterization of marine and terrestrial DOM in seawater using excitation-emission matrix spectroscopy. *Marine Chemistry* **1996,** *51* (4), 325-346.

98. Rutlidge, H.; Baker, A.; Marjo, C. E.; Andersen, M. S.; Graham, P. W.; Cuthbert, M. O.; Rau, G. C.; Roshan, H.; Markowska, M.; Mariethoz, G.; Jex, C. N., Dripwater organic matter and trace element geochemistry in a semi-arid karst environment: Implications for speleothem paleoclimatology. *Geochimica et Cosmochimica Acta* **2014,** *135*, 217-230.

99. Hartland, A.; Fairchild, I. J.; Lead, J. R.; Baker, A., Fluorescent properties of organic carbon in cave dripwaters: Effects of filtration, temperature and pH. *Science of The Total Environment* **2010,** *408* (23), 5940-5950.

100. Bischoff, W. D.; Sharma, S. K.; MacKenzie, F. T., Carbonate ion disorder in synthetic and biogenic magnesian calcites: A Raman spectral study. *American Minerologist* **1985,** *70* (5-6), 581-589.

101. Jacob, D. E.; Wehrmeister, U.; Soldati, A. L.; Häger, T.; Hofmeister, W., Vaterite in freshwater cultured pearls from China and Japan. *The Gemmological Association of Great Britain* **2007,** *31* (5), 269-276.

102. Behrens, G.; Kuhn, L. T.; Ubic, R.; Heuer, A. H., Raman spectra of vateritic calcium carbonate. *Spectroscopy Letters* **1995,** *28* (6), 983-995.

103. Hu, Q.; Zhang, J.; Teng, H.; Becker, U., Growth process and crystallographic properties of ammonia-induced vaterite. **2012,** *97* (8-9), 1437.

104. R Core Team, *R: A language and environment for statistical computing*. R Foundation for Statistical Computing: Vienna, Austria, 2013.

105. Wickham, H., *ggplot2: Elegant Graphics for Data Analysis*. Springer-Verlag: New York, 2016.

106. Fairchild, I. J.; Hartland, A., Trace element variations in stalagmites: Controls by climate and by karst system processes. In *Ion Partitioning in Ambient Temperature Aqueous Systems: From Fundamentals to Applications in Climate Proxies and Environmental Geochemistry* Stoll, H.; Prieto, M., Eds. European Mineralogical Union: Oviedo, 2010.

107. Kinniburgh, D. G.; van Riemsdijk, W. H.; Koopal, L. K.; Borkovec, M.; Benedetti, M. F.; Avena, M. J., Ion binding to natural organic matter: Competition, heterogeneity, stoichiometry and thermodynamic consistency. *Colloids and Surfaces A: Physicochemical and Engineering Aspects* **1999,** *151* (1), 147-166.

108. Meldrum, F. C.; Hyde, S. T., Morphological influence of magnesium and organic additives on the precipitation of calcite. *Journal of Crystal Growth* **2001,** *231* (4), 544-558.

109. Zhang, Y.; Dawe, R. A., Influence of Mg^{2+} on the kinetics of calcite precipitation and calcite crystal morphology. *Chemical Geology* **2000,** *163* (1), 129-138.

110. Frisia, S.; Borsato, A.; Hellstrom, J., High spatial resolution investigation of nucleation, growth and early diagenesis in speleothems as exemplar for sedimentary carbonates. *Earth-Science Reviews* **2018,** *178*, 68-91.

111. Lakshtanov, L. Z.; Stipp, S. L. S., Experimental study of nickel(II) interaction with calcite: Adsorption and coprecipitation. *Geochimica et Cosmochimica Acta* **2007,** *71* (15), 3686-3697.

112. Chakraborty, P.; Manek, A.; Niyogi, S.; Hudson, J., Determination of dynamic metal complexes and their diffusion coefficients in the presence of different humic substances by combining two analytical techniques. *Analytical Letters* **2014,** *47* (7), 1224-1241.

113. van Beynen, P.; Bourbonniere, R.; Ford, D.; Schwarcz, H., Causes of colour and fluorescence in speleothems. *Chemical Geology* **2001,** *175* (3), 319-341.

114. Gázquez, F.; Calaforra, J. M.; Rull, F.; Forti, P.; García-Casco, A., Organic matter of fossil origin in the amberine speleothems from El Soplao Cave (Cantabria, Northern Spain). *International Journal of Speleology* **2102,** *41*, 113-123.

115. Murphy, E. M.; Zachara, J. M.; Smith, S. C.; Phillips, J. L. *The sorption of humic acids to mineral surfaces and their role in contaminant binding*, 5th International Meeting of the International Humic Substances Soc: Advances in Humic Substances Research, Nagoya, Japan, Nagoya, Japan, 1990; pp 413-423.

Appendix I

Script 1: PHREEQC script for determining species distribution, pH and calcite saturation indices (SI) in reservoir solutions.

```
SELECTED_OUTPUT
-file c:\
-user_punch true
-high_precision false
-totals Ca Cu Co Ni C C(4)
-molalities Cu+2 Cu+ Co+2 Co+3 Ni+2 Ca+2 CH4 CO3-2 HCO3- CO2 (CO2)2 CaOH+ CaCO3 CaHCO3+ CuCO3 Cu(CO3)2-2 CuHCO3+ CuOH+ Cu(OH)2 Cu(OH)3- Cu(OH)4-2 Cu2(OH)2+2 NiOH+ Ni(OH)2 Ni(OH)3- CoOH+ Co(OH)2 Co(OH)3- Co(OH)4-2 Co2OH+3 Co4(OH)4+4 CoOOH- CoOH+2 NiCO3 NiHCO3+ CoCO3 CoHCO3+ H2CO3
-pH
-saturation_indices CO2(g) Calcite Aragonite

SOLUTION 1 Pure Water
ph 7.0
temp 20
units mol/l
Cu 7.868E-07
Ni 8.5189E-07
Co 8.484E-07

EQUILIBRIUM_Phases
CO2(g) -3.402
save solution 1
End

USE solution 1
REACTION 1
Calcite 0.0049853
save solution 1
END

USE solution 1
Equilibrium_Phases 1
CO2(g)  0                    #Sequentially adjust this value until the desired SI of calcite is reached
SAVE solution 2
END
```

Script 2: PHRREQC script for determination of the relationship between [Ca] and conductance.

```
SOLUTION 1 Pure water
pH 8.0
temp 20

EQUILIBRIUM_PHASES 1
CO2(g) -3.4202
SAVE solution 1
END

USE solution 1
REACTION 1
CaCO3 0.001

EQUILIBRIUM_PHASES 1
CO2(g) -3
SAVE solution 1
END

USE solution 1
REACTION 1
CaCO3 0.001

EQUILIBRIUM_PHASES 1
CO2(g) -3
SAVE solution 1
END

USE solution 1
REACTION 1
CaCO3 0.001

EQUILIBRIUM_PHASES 1
CO2(g) -3
SAVE solution 1
END

USE solution 1
REACTION 1
CaCO3 0.001

EQUILIBRIUM_PHASES 1
CO2(g) -3
SAVE solution 1
END

USE solution 1
REACTION 1
CaCO3 0.001
```

```
EQUILIBRIUM_PHASES 1
CO2(g) -3
SAVE solution 1
END

USE solution 1
REACTION 1
CaCO3 0.001

EQUILIBRIUM_PHASES 1
CO2(g) -3
SAVE solution 1
END

USE solution 1
REACTION 1
CaCO3 0.001

EQUILIBRIUM_PHASES 1
CO2(g) -3
SAVE solution 1
END

USE solution 1
REACTION 1
CaCO3 0.001

EQUILIBRIUM_PHASES 1
CO2(g) -3
SAVE solution 1
END

USE solution 1
REACTION 1
CaCO3 0.001

EQUILIBRIUM_PHASES 1
CO2(g) -3
SAVE solution 1
END
```

Script 3: R script used to fit conductivity data to Equation 1.7 and calculate $\tau_{pr.}$

```
library(ggplot2)

data <- read.table(file = "filename.txt", header = TRUE, sep = "\t") #file with residence time and conductivity data
t <- data$t          #Header of column containing residence times (t is used in this example)
c <- data$c          #Header of column containing conductivity data (c is used in this example)

gplot <- ggplot(data=data) + geom_point(aes(t,c))      #Plots conductivity data against time

fit.c <- nls(formula = c ~ (C0 - Ceq) * exp(-t / tau) + Ceq, start = list(C0 = data$c[10], Ceq = 250, tau = 250)) #Exponential fit of conductivity values
fit.c

coef(fit.c)

gplot + geom_smooth(aes(t,fitted(fit.c)),colour="black") + labs(x = "Time (s)", y = "Conductance (uS)")

ggsave("exp5_fig.png", device="png")         #Exports graph as a .png file

confint(fit.c)

summary(fit.c)

# List of the values determined by the exponential fit

Ceq <- coef(summary(fit.c))[2,"Estimate"]              #Equilibrium conductivity value
Ceq.err <- coef(summary(fit.c))[2, "Std. Error"]       #Error in equilibrium conductivity value
C0 <- coef(summary(fit.c))[1,"Estimate"]               #Initial conductivity value
C0.err <- coef(summary(fit.c))[1, "Std. Error"]        #Error in Initial conductivity value
tau.err <- coef(summary(fit.c))[3,"Std. Error"]        #Time constant of precipitation
tau <- coef(summary(fit.c))[3,"Estimate"]              #Error in time constant of precipitation

# Export the fitted data in a results sheet

export.data <- data.frame(name=c("Ceq", "Ceq error", "C0", "C0 error", "tau", "tau.err"), value = c(Ceq, Ceq.err, C0, C0.err, tau, tau.err))
write.table(x = export.data, file = "exp5_export.txt", sep = ";", row.names = FALSE)
```

Appendix II

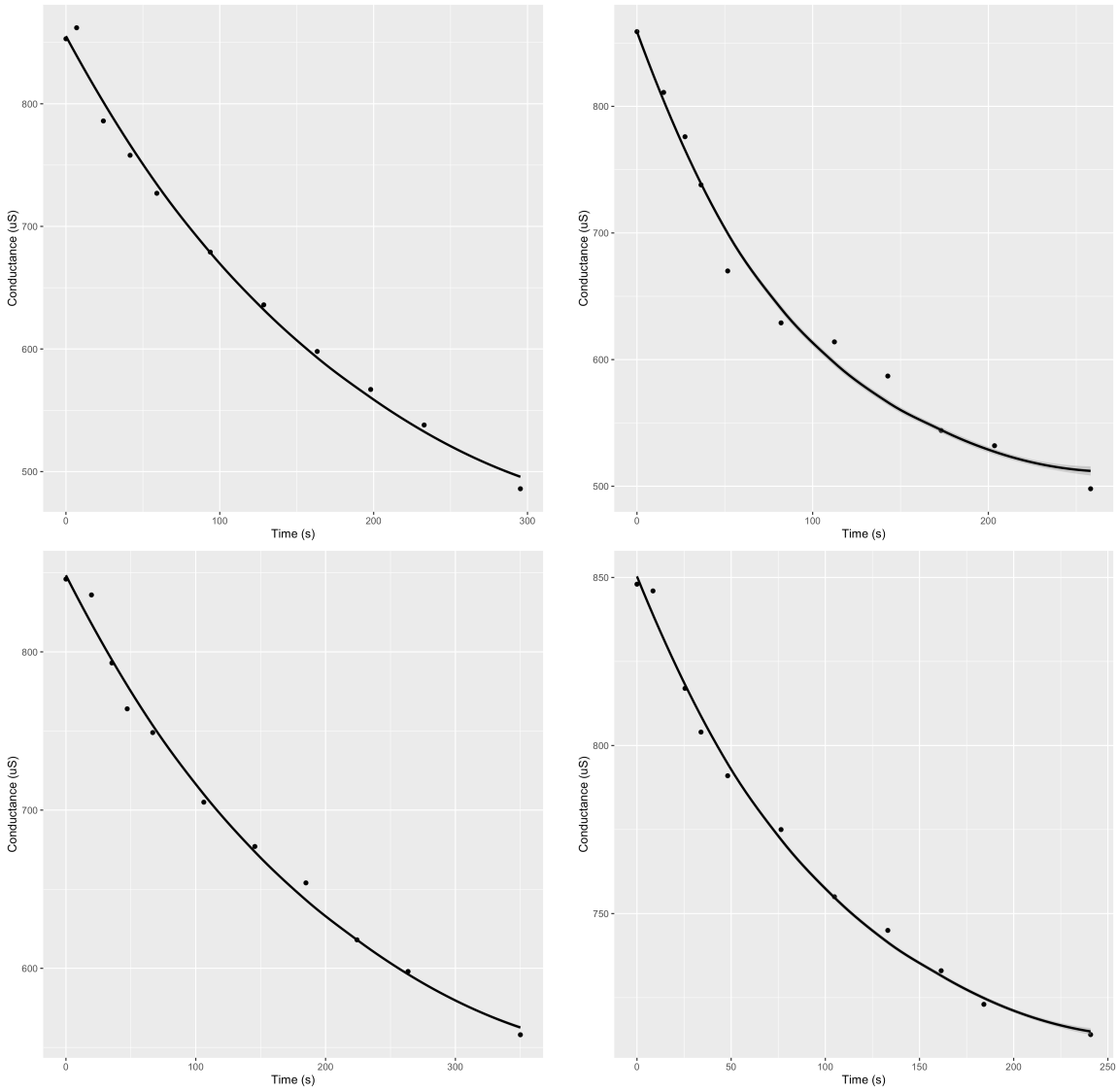

Figure A.1. Conductivity data for experiments 1-4 fitted to Equation 1.7, allowing calculation of precipitation time constants and subsequently, growth rate.

Table A.1. Metal concentrations in solution samples taken during experiment 1. Errors represent one standard deviation of triplicate ICP-MS measurements.

Distance of Flow (cm)	[Ca] (M)	±	[Co] (mM)	±	[Ni] (mM)	±	[Cu] (mM)	±
0	0.0047	1.3×10^{-4}	0.00089	1.7×10^{-5}	0.00091	6.5×10^{-6}	0.00067	8.1×10^{-6}
2	0.0047	6.6×10^{-5}	0.00099	1.8×10^{-5}	0.00098	1.6×10^{-5}	0.00044	1.3×10^{-5}
7	0.0044	3.1×10^{-5}	0.00076	7.6×10^{-7}	0.00089	1.4×10^{-5}	0.00020	4.3×10^{-7}
12	0.0042	8.8×10^{-5}	0.00063	6.3×10^{-6}	0.00085	1.0×10^{-5}	0.00005	7.6×10^{-7}
17	0.0040	1.2×10^{-4}	0.00049	5.9×10^{-6}	0.00081	1.2×10^{-5}	<QL	-
27	0.0037	1.9×10^{-5}	0.00031	2.2×10^{-6}	0.00072	4.4×10^{-6}	<QL	-
37	0.0035	9.7×10^{-5}	0.00022	2.2×10^{-6}	0.00066	2.7×10^{-6}	<QL	-
47	0.0032	7.1×10^{-5}	0.00016	2.2×10^{-6}	0.00061	2.5×10^{-6}	<QL	-
57	0.0031	3.4×10^{-5}	0.00012	2.7×10^{-6}	0.00058	9.9×10^{-6}	<QL	-
67	0.0029	8.1×10^{-5}	0.00010	2.6×10^{-6}	0.00056	1.2×10^{-5}	<QL	-
85	0.0025	6.5×10^{-5}	0.00010	2.1×10^{-6}	0.00057	9.2×10^{-6}	<QL	-

Table A.2. Metal concentrations in $CaCO_3$ samples precipitated during experiment 1. Errors represent one standard deviation of triplicate ICP-MS measurements.

Distance of Flow (cm)	[Ca] (ug/g)	±	[Co] (ug/g)	±	[Ni] (ug/g)	±	[Cu] (ug/g)	±
2	374515	7887	297	9.2	85	1.8	1888	32.1
7	398977	5224	254	3.0	55	0.6	1704	25.6
12	417173	5862	274	5.8	68	0.4	960	6.7
17	359672	1461	385	2.7	112	1.7	411	4.9
27	367984	4070	399	2.4	154	0.5	77	0.2
37	381582	11851	344	14.1	164	5.1	32	1.2
47	340612	2747	212	3.6	131	1.3	12	0.2
57	346501	6605	151	3.5	132	0.9	6	0.1
67	331315	17914	149	3.1	149	3.6	8	0.3
85	377826	3422	79	0.4	120	0.6	15	0.1

Table A.3. Metal concentrations in solution samples taken during experiment 2. Errors represent one standard deviation of triplicate ICP-MS measurements.

Distance of Flow (cm)	[Ca] (M)	±	[Co] (mM)	±	[Ni] (mM)	±	[Cu] (mM)	±
0	0.0047	4.2×10^{-4}	0.00080	6.9×10^{-5}	0.00075	6.6×10^{-5}	0.00044	3.9×10^{-5}
5	0.0050	1.2×10^{-4}	0.00087	1.8×10^{-5}	0.00088	1.7×10^{-5}	<QL	-
9	0.0045	1.1×10^{-4}	0.00058	9.3×10^{-6}	0.00074	1.2×10^{-5}	<QL	-
12	0.0043	7.0×10^{-5}	0.00047	2.4×10^{-6}	0.00071	8.3×10^{-6}	<QL	-
17	0.0041	6.7×10^{-5}	0.00039	5.1×10^{-6}	0.00067	1.1×10^{-5}	<QL	-
27	0.0043	7.9×10^{-4}	0.00032	4.0×10^{-5}	0.00068	8.9×10^{-5}	<QL	-
37	0.0037	1.2×10^{-4}	0.00024	5.1×10^{-6}	0.00061	1.0×10^{-5}	<QL	-
47	0.0036	1.3×10^{-4}	0.00020	3.8×10^{-6}	0.00057	1.3×10^{-5}	<QL	-
57	0.0033	3.9×10^{-5}	0.00016	2.4×10^{-6}	0.00055	4.2×10^{-6}	<QL	-
67	0.0033	7.2×10^{-5}	0.00015	1.7×10^{-6}	0.00053	5.2×10^{-6}	<QL	-
85	0.0032	8.0×10^{-5}	0.00011	3.4×10^{-6}	0.00050	1.5×10^{-6}	<QL	-

Table A.4. Metal concentrations in $CaCO_3$ samples precipitated during experiment 2. Errors represent one standard deviation of triplicate ICP-MS measurements.

Distance of Flow (cm)	[Ca] (ug/g)	±	[Co] (ug/g)	±	[Ni] (ug/g)	±	[Cu] (ug/g)	±
2	374515	7887	297	9.2	85	1.8	1888	32.1
7	398977	5224	254	3.0	55	0.6	1704	25.6
12	417173	5862	274	5.8	68	0.4	960	6.7
17	359672	1461	385	2.7	112	1.7	411	4.9
27	367984	4070	399	2.4	154	0.5	77	0.2
37	381582	11851	344	14.1	164	5.1	32	1.2
47	340612	2747	212	3.6	131	1.3	12	0.2
57	346501	6605	151	3.5	132	0.9	6	0.1
67	331315	17914	149	3.1	149	3.6	8	0.3
85	377826	3422	79	0.4	120	0.6	15	0.1

Table A.5. Metal concentrations in solution samples taken during experiment 3. Errors represent one standard deviation of triplicate ICP-MS measurements.

Distance of Flow (cm)	[Ca] (M)	±	[Co] (mM)	±	[Ni] (mM)	±	[Cu] (mM)	±
0	0.0047	1.0×10^{-4}	0.00079	1.5×10^{-5}	0.00076	1.4×10^{-5}	0.00063	1.3×10^{-5}
5	0.0048	9.3×10^{-5}	0.00080	1.4×10^{-5}	0.00076	1.4×10^{-5}	0.00065	1.0×10^{-5}
9	0.0046	7.6×10^{-5}	0.00077	7.1×10^{-6}	0.00074	8.9×10^{-6}	0.00062	7.2×10^{-6}
12	0.0044	2.9×10^{-5}	0.00076	6.2×10^{-6}	0.00074	7.4×10^{-6}	0.00059	6.9×10^{-6}
17	0.0043	1.3×10^{-4}	0.00075	9.2×10^{-6}	0.00074	8.9×10^{-6}	0.00057	1.0×10^{-5}
27	0.0041	9.8×10^{-5}	0.00074	1.2×10^{-5}	0.00075	8.2×10^{-6}	0.00055	5.9×10^{-6}
37	0.0040	8.3×10^{-5}	0.00074	1.3×10^{-5}	0.00075	1.7×10^{-5}	0.00053	7.9×10^{-6}
47	0.0036	1.3×10^{-4}	0.00071	4.4×10^{-6}	0.00074	5.1×10^{-6}	0.00050	7.0×10^{-6}
57	0.0036	1.1×10^{-4}	0.00071	1.0×10^{-5}	0.00075	1.1×10^{-5}	0.00048	6.7×10^{-6}
67	0.0033	2.6×10^{-5}	0.00068	7.0×10^{-6}	0.00073	1.3×10^{-5}	0.00045	5.0×10^{-6}
89	0.0031	1.2×10^{-4}	0.00067	1.6×10^{-5}	0.00073	1.8×10^{-5}	0.00044	1.0×10^{-5}

Table A.6. Metal concentrations in $CaCO_3$ samples precipitated during experiment 3. Errors represent one standard deviation of triplicate ICP-MS measurements.

Distance of Flow (cm)	[Ca] (ug/g)	±	[Co] (ug/g)	±	[Ni] (ug/g)	±	[Cu] (ug/g)	±
5	285614	7646	27	0.6	3.8	0.4	49	0.9
9	276751	4924	24	0.6	1.0	0.3	46	1.1
12	290387	14169	32	0.7	5.9	0.4	57	1.5
17	317554	8160	37	1.0	1.9	0.3	68	1.7
27	329306	11090	39	0.5	2.0	0.4	72	1.7
37	297586	5276	38	0.9	1.8	0.4	68	1.0
47	326472	3804	36	1.1	1.7	0.3	67	1.7
57	320104	8222	33	0.6	2.2	0.4	61	1.7
67	310322	1450	31	0.1	2.0	0.6	57	0.3
89	308046	12547	34	1.2	1.8	0.5	56	1.7

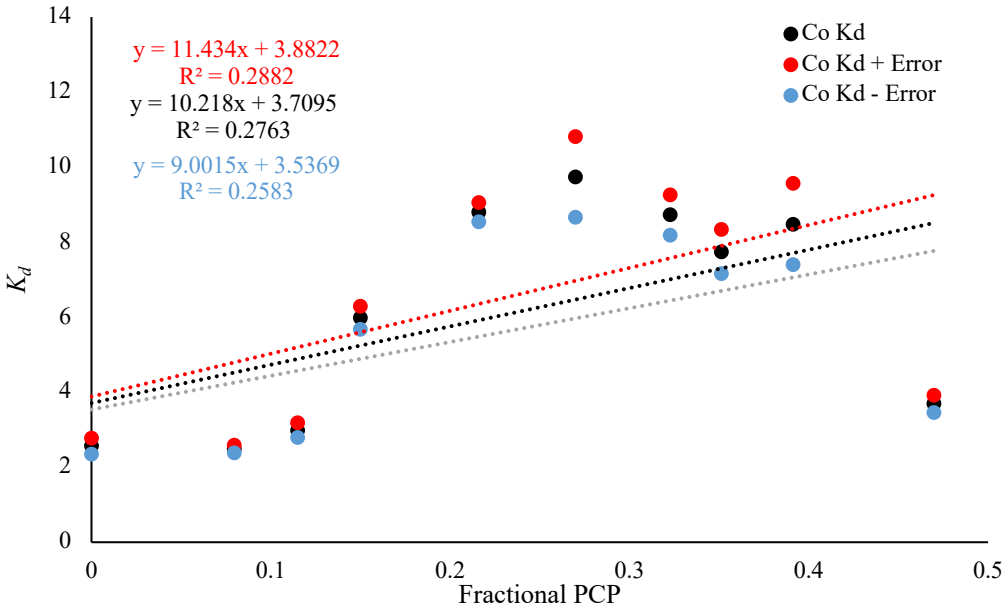

Figure A.2. Linear regression of PCP and partition coefficients calculated for Co during experiment 1. Equations were used to calculate changing K_d values as PCP increased during modelling of Co partitioning under inorganic conditions.

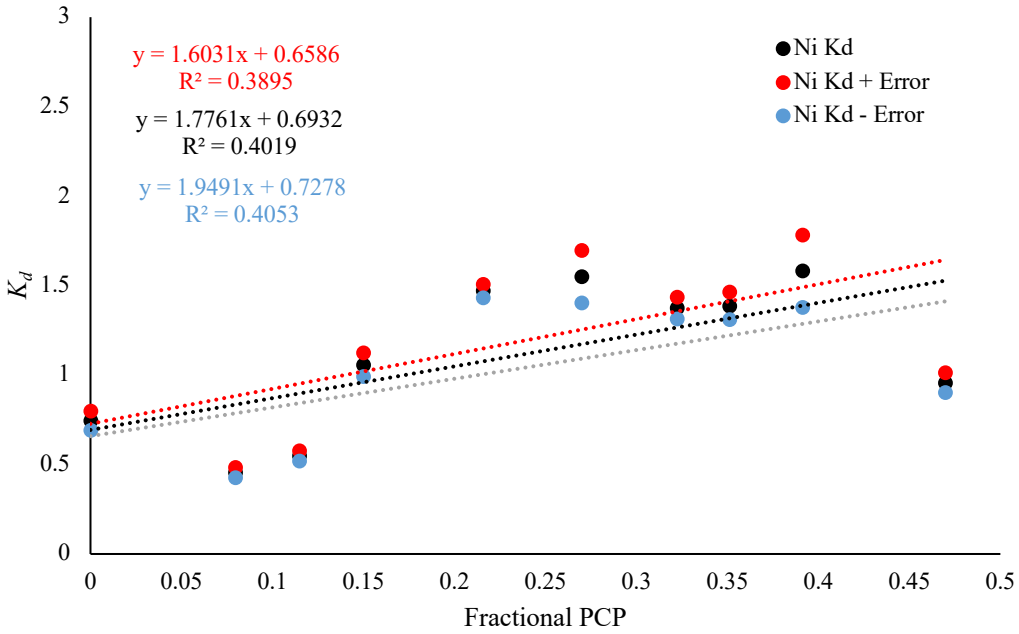

Figure A.3. Linear regression of PCP and partition coefficients calculated for Ni during experiment 1. Equations were used to calculate changing K_d values as PCP increased during modelling of Ni partitioning under inorganic conditions.

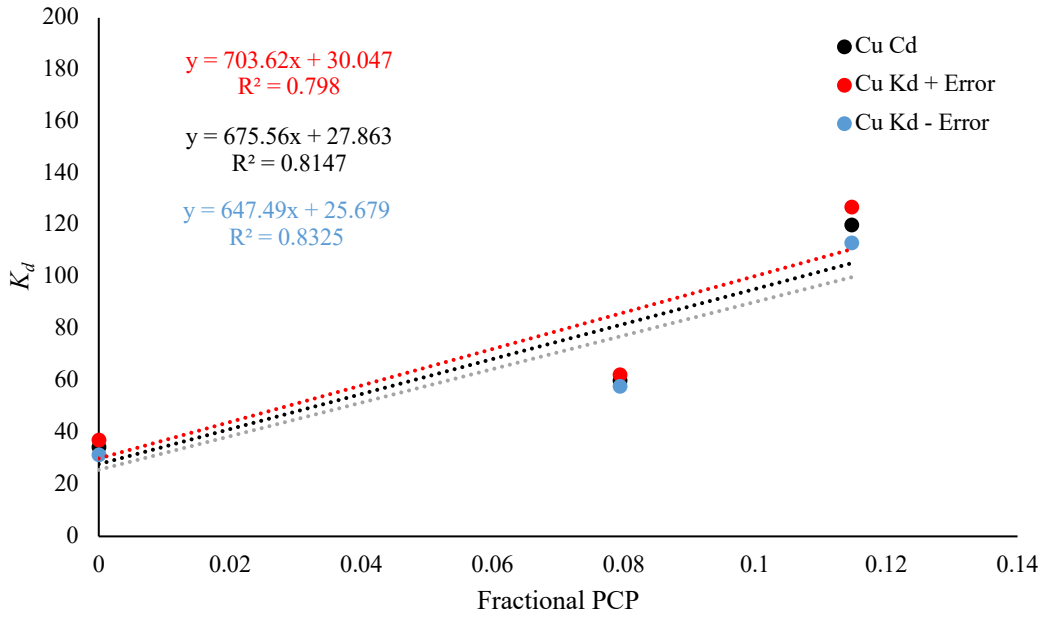

Figure A.4. Linear regression of PCP and partition coefficients calculated for Cu during experiment 1. Equations were used to calculate changing K_d values as PCP increased during modelling of Cu partitioning under inorganic conditions.

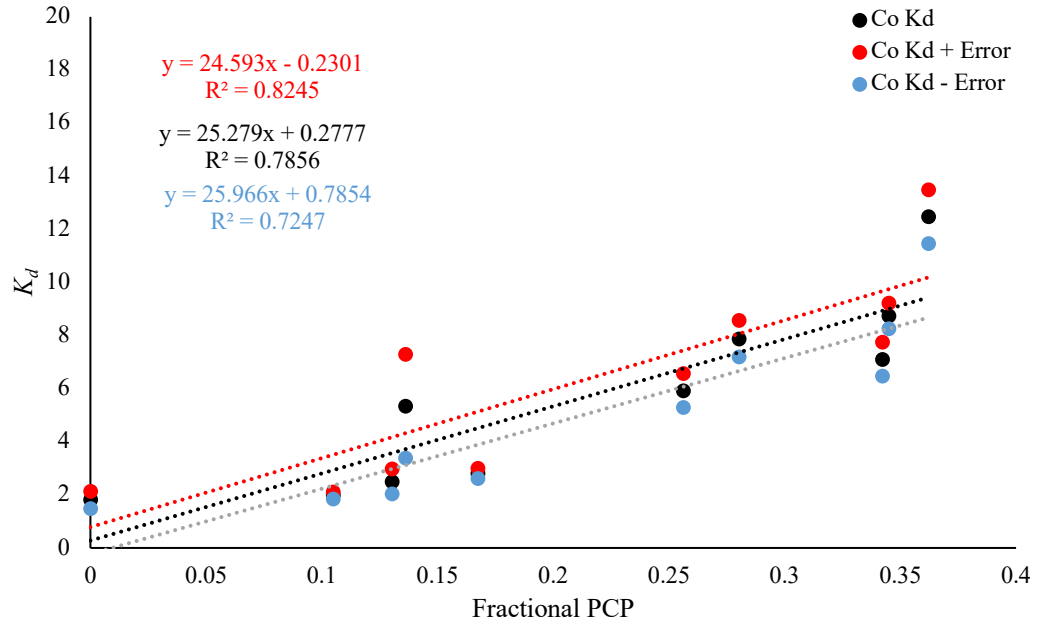

Figure A.5. Linear regression of PCP and partition coefficients calculated for Co during experiment 2. Equations were used to calculate changing K_d values as PCP increased during modelling of Co partitioning under inorganic conditions.

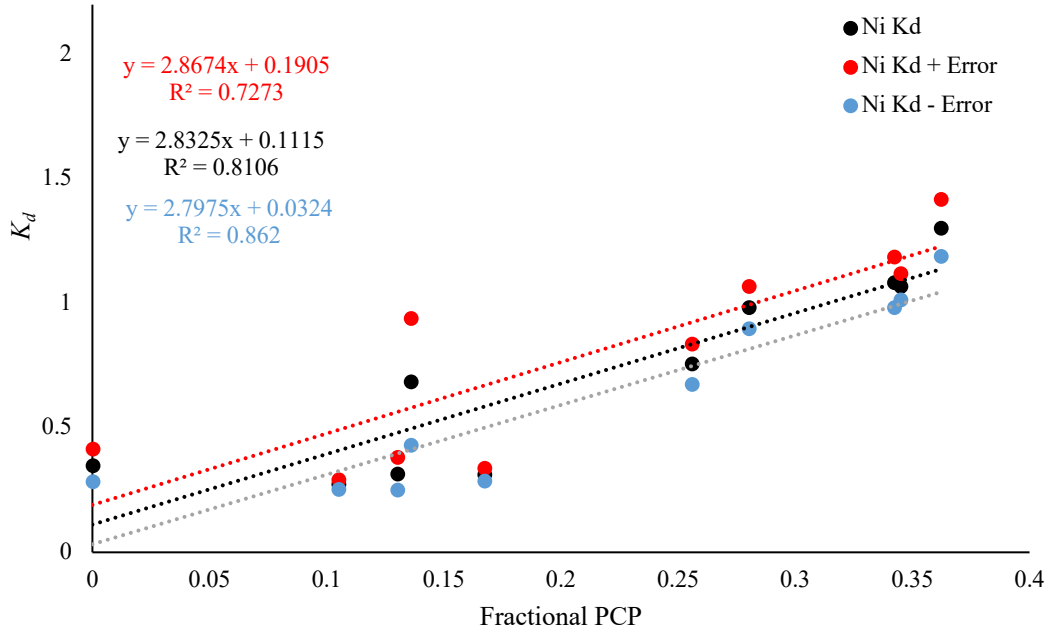

Figure A.6. Linear regression of PCP and partition coefficients calculated for Ni during experiment 2. Equations were used to calculate changing K_d values as PCP increased during modelling of Ni partitioning under inorganic conditions.

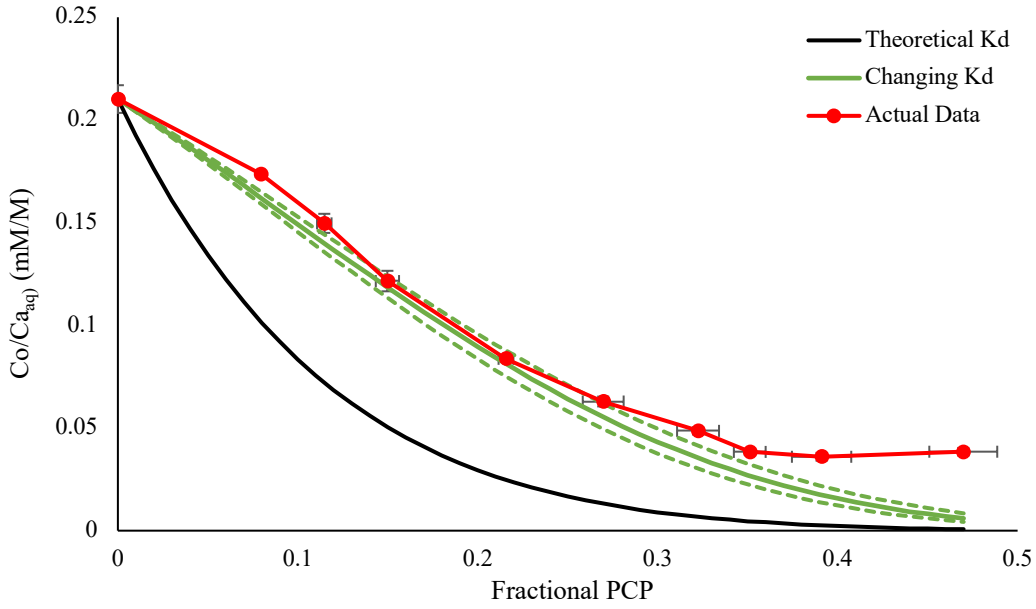

Figure A.7. Co/Ca ratios determined for solution samples taken during experiment 1, with modelled Co/Ca ratios based on both theoretical literature K_d values and experimental K_d values predicted by regressing K_d at changing distances of flow against PCP. The black line represents modelling undertaken with the theoretical K_d value predicted by Wang and Xu (2001) using a linear free energy correlation approach, while the green solid line represents modelling based on the changing experimental K_d values. Green dashed lines indicate error associated with the experimental K_d values.

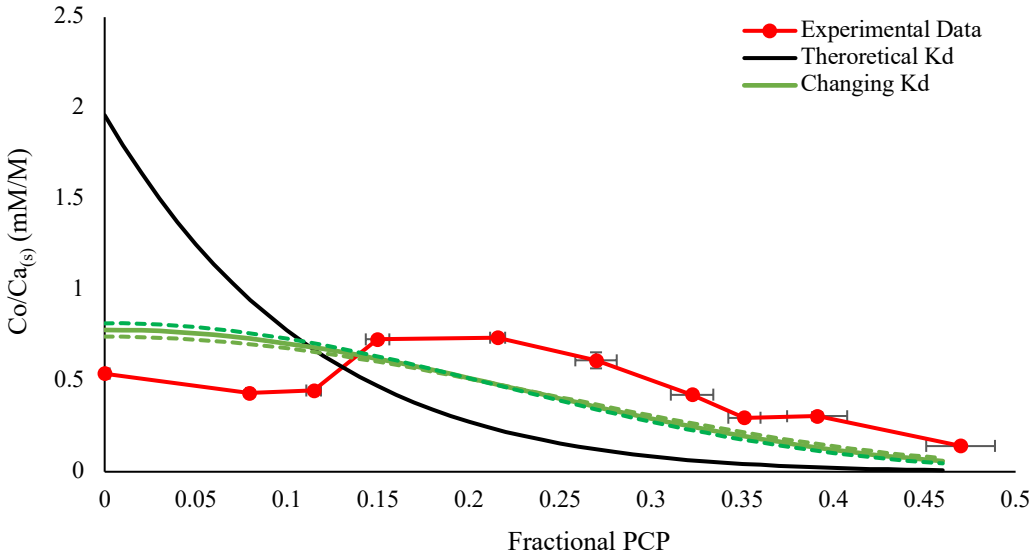

Figure A.8. Co/Ca ratios determined for precipitate samples taken during experiment 1, with modelled Co/Ca ratios based on both theoretical literature K_d values and experimental K_d values predicted by regressing K_d at changing distances of flow against PCP. The black line represents modelling undertaken with the theoretical K_d value predicted by Wang and Xu (2001) using a linear free energy correlation approach, while the green solid line represents modelling based on the changing experimental K_d values. Green dashed lines indicate error associated with the experimental K_d values.

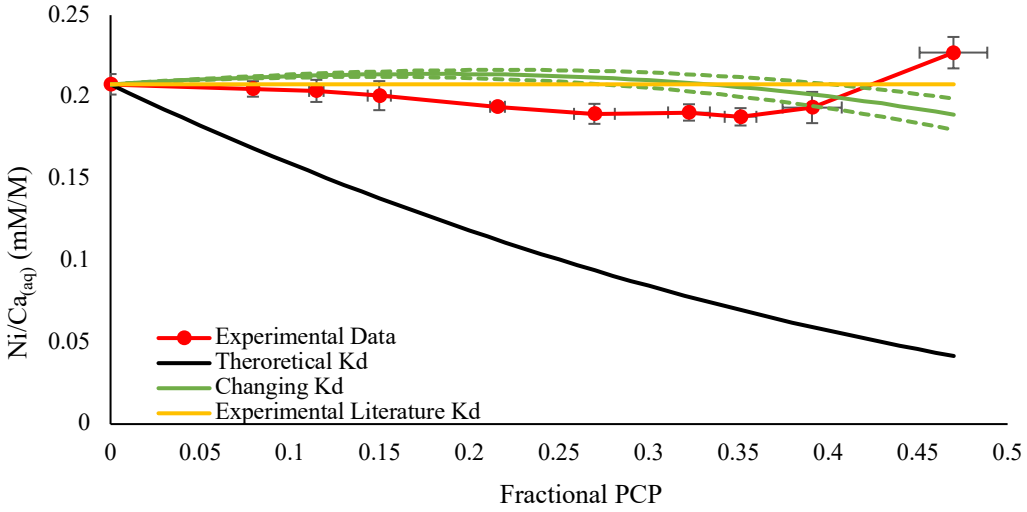

Figure A.9. Ni/Ca ratios determined for solution samples taken during experiment 1, with modelled Ni/Ca ratios based on both theoretical literature K_d values and experimental K_d values predicted by regressing K_d at changing distances of flow against PCP. The black line represents modelling undertaken with the theoretical K_d value predicted by Wang and Xu (2001) using a linear free energy correlation approach, while the green solid line represents modelling based on the changing experimental K_d values. Green dashed lines indicate error associated with the experimental K_d values. The yellow line indicates modelling results based on the Ni partition coefficient determined for dilute solid solutions by Stipp and Lakshtanov (2007).

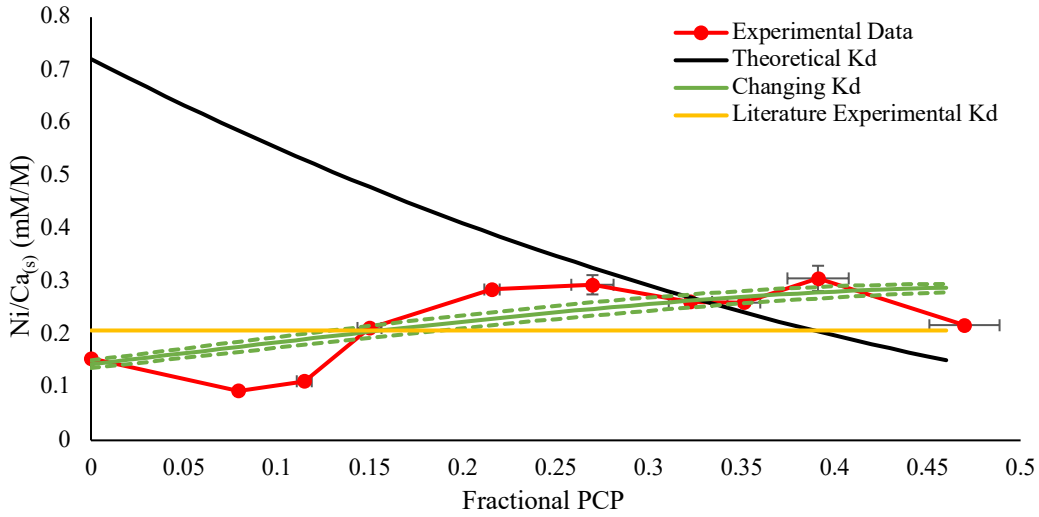

Figure A.10. Ni/Ca ratios determined for precipitate samples taken during experiment 1, with modelled Ni/Ca ratios based on both theoretical literature K_d values and experimental K_d values predicted by regressing K_d at changing distances of flow against PCP. The black line represents modelling undertaken with the theoretical K_d value predicted by Wang and Xu (2001) using a linear free energy correlation approach, while the green solid line represents modelling based on the changing experimental K_d values. Green dashed lines indicate error associated with the experimental K_d values. The yellow line indicates modelling results based on the Ni partition coefficient determined for dilute solid solutions by Stipp and Lakshtanov (2007).

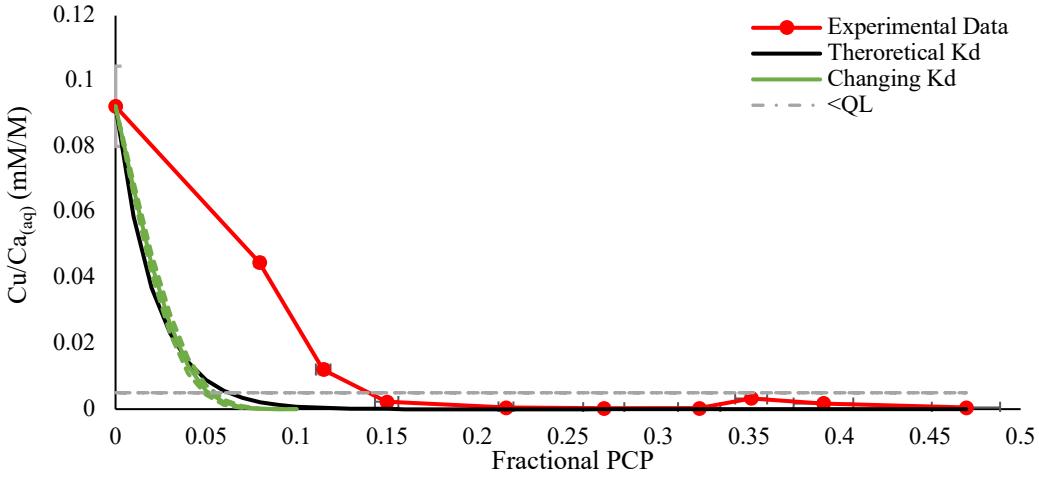

Figure A.11. Cu/Ca ratios determined for solution samples taken during experiment 1, with modelled Cu/Ca ratios based on both theoretical literature K_d values and experimental K_d values predicted by regressing K_d at changing distances of flow against PCP. The black line represents modelling undertaken with the theoretical K_d value predicted by Wang and Xu (2001) using a free energy correlation approach, while the green solid line represents modelling based on the changing experimental K_d values. Green dashed lines indicate error associated with the experimental K_d values. Experimental data below the grey dashed line were below the ICP-MS limit of quantification (QL).

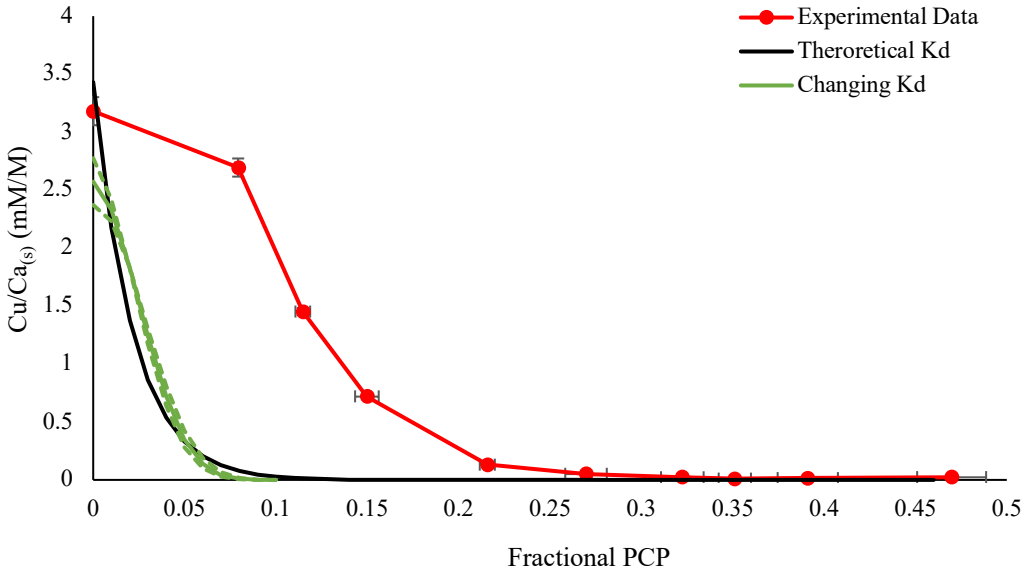

Figure A.12. Cu/Ca ratios determined for precipitate samples taken during experiment 1, with modelled Cu/Ca ratios based on both theoretical literature K_d values and experimental K_d values predicted by regressing K_d at changing distances of flow against PCP. The black line represents modelling undertaken with the theoretical K_d value predicted by Wang and Xu (2001) using a linear free energy correlation approach, while the green solid line represents modelling based on the changing experimental K_d values. Green dashed lines indicate error associated with the experimental K_d values.

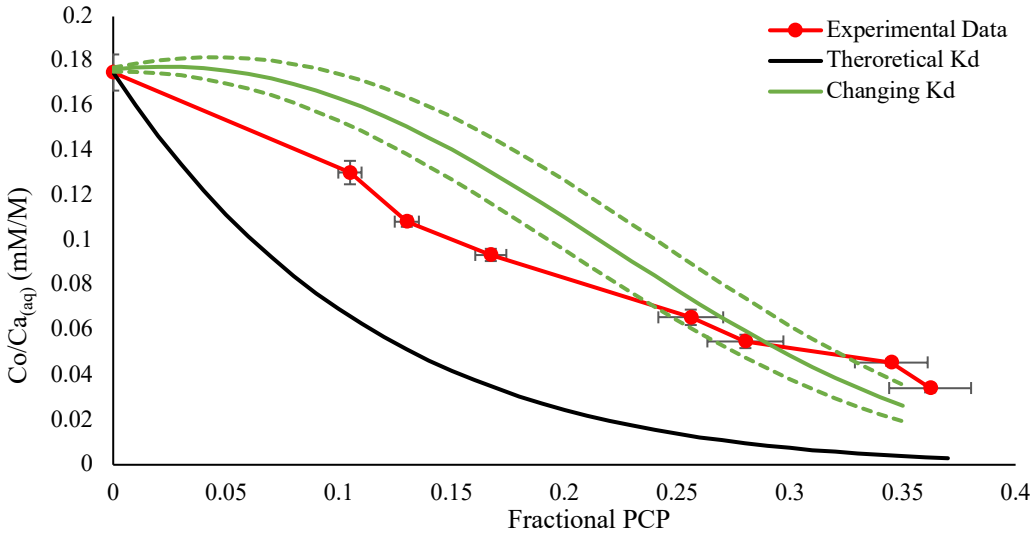

Figure A.13. Co/Ca ratios determined for solution samples taken during experiment 2, with modelled Co/Ca ratios based on both theoretical literature K_d values and experimental K_d values predicted by regressing K_d at changing distances of flow against PCP. The black line represents modelling undertaken with the theoretical K_d value predicted by Wang and Xu (2001) using a linear free energy correlation approach, while the green solid line represents modelling based on the changing experimental K_d values. Green dashed lines indicate error associated with the experimental K_d values.

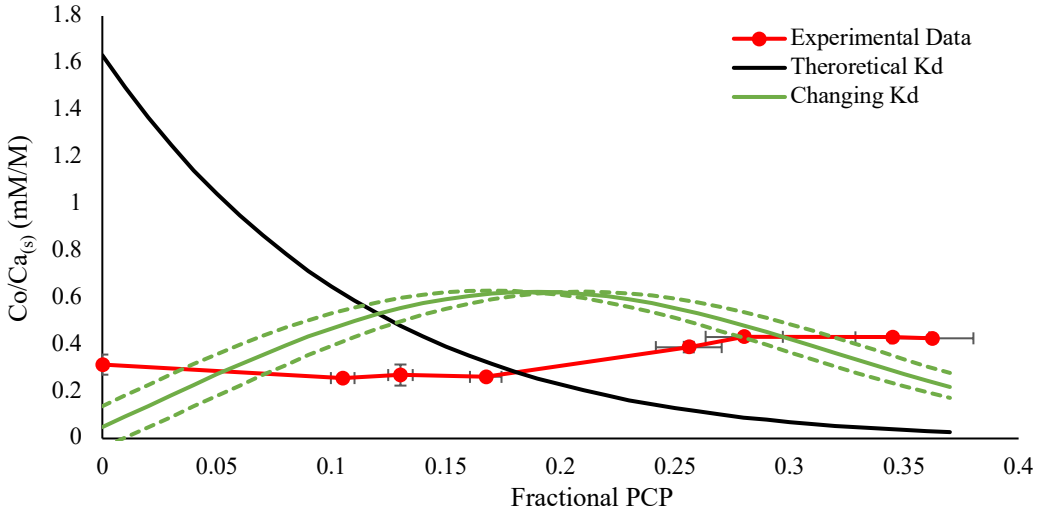

Figure A.14. Co/Ca ratios determined for precipitate samples taken during experiment 2, with modelled Co/Ca ratios based on both theoretical literature K_d values and experimental K_d values predicted by regressing K_d at changing distances of flow against PCP. The black line represents modelling undertaken with the theoretical K_d value predicted by Wang and Xu (2001) using a linear free energy correlation approach, while the green solid line represents modelling based on the changing experimental K_d values. Green dashed lines indicate error associated with the experimental K_d values.

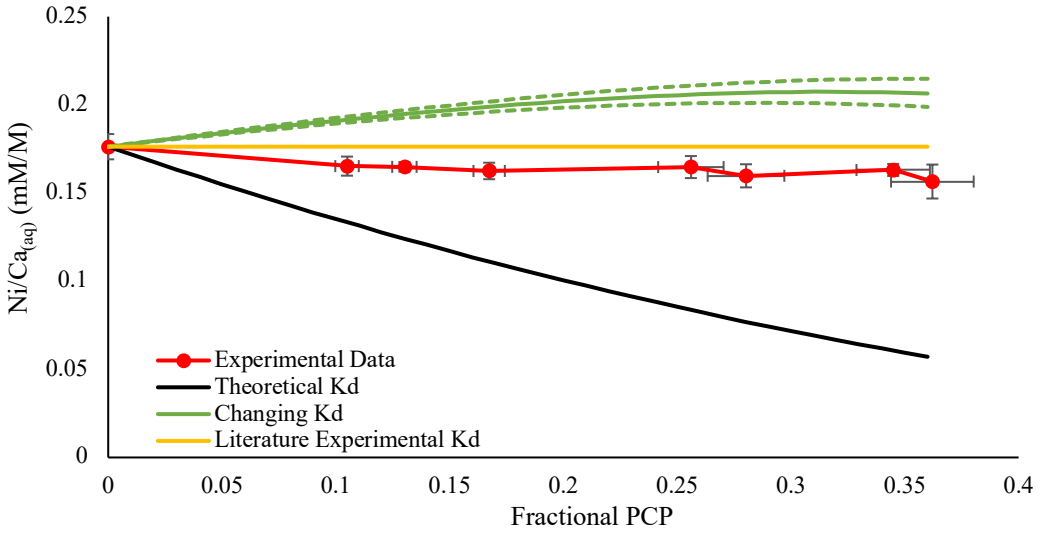

Figure A.15. Ni/Ca ratios determined for psolution samples taken during experiment 2, with modelled Ni/Ca ratios based on both theoretical literature K_d values and experimental K_d values predicted by regressing K_d at changing distances of flow against PCP. The black line represents modelling undertaken with the theoretical K_d value predicted by Wang and Xu (2001) using a linear free energy correlation approach, while the green solid line represents modelling based on the changing experimental K_d values. Green dashed lines indicate error associated with the experimental K_d values. The yellow line indicates modelling results based on the Ni partition coefficient determined for dilute solid solutions by Stipp and Lakshtanov (2007).

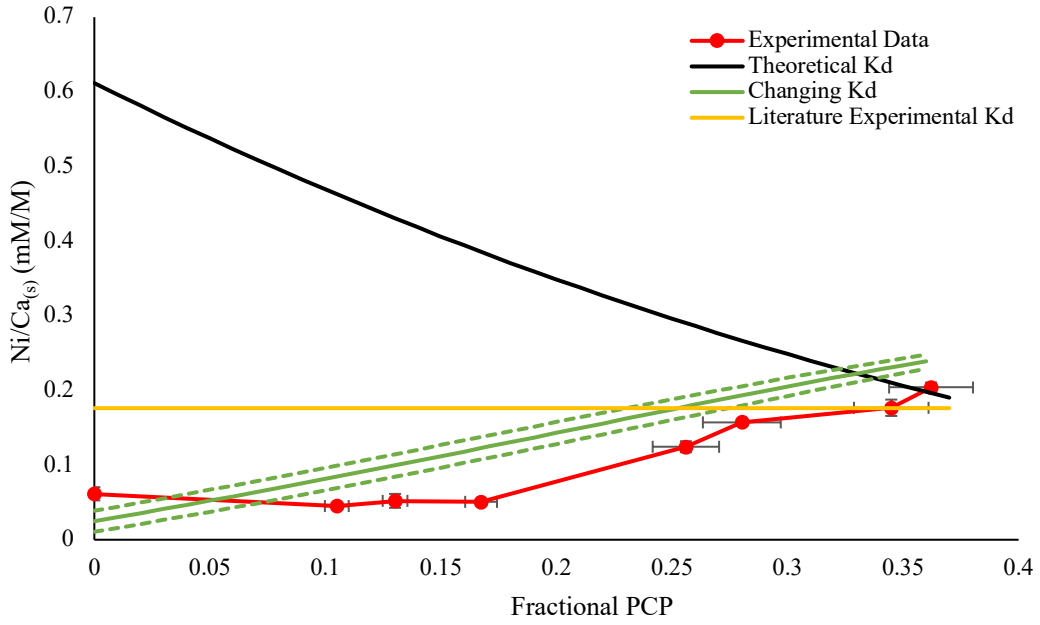

Figure A.16. Ni/Ca ratios determined for precipitate samples taken during experiment 2, with modelled Ni/Ca ratios based on both theoretical literature K_d values and experimental K_d values predicted by regressing K_d at changing distances of flow against PCP. The black line represents modelling undertaken with the theoretical K_d value predicted by Wang and Xu (2001) using a linear free energy correlation approach, while the green solid line represents modelling based on the changing experimental K_d values. Green dashed lines indicate error associated with the experimental K_d values. The yellow line indicates modelling results based on the Ni partition coefficient determined for dilute solid solutions by Stipp and Lakshtanov (2007).